SYNTHESIS AND CHARACTERIZATION OF HEAVILY CYANATED BORON CLUSTERS

Austin A. Kamin

A thesis submitted in partial fulfillment of the requirements
for graduation with Honors in Chemistry

Whitman College
2020

Certificate of Approval

This is to certify that the accompanying thesis by Austin A. Kamin has been accepted in partial fulfillment of the requirements for graduation with Honors in Chemistry.

Marcus A. Juhasz

Whitman College

May 20, 2020

ABSTRACT

Compounds based on polyhedral boron clusters, such as $[B_{12}H_{12}]^{2-}$, have a wide array of potential applications ranging from new drugs to advanced electronics. Computational and experimental studies suggest that heavily cyanated boron cluster derivatives are amongst the most electronically stable anions known and could function as excellent weakly coordinating anions (WCAs) or as superior electrolytes in metal-ion batteries. Current methods for the derivatization of these boron clusters are limited, and the synthesis and isolation of any percyanated boron clusters has not previously been reported. The percyanated *closo*-dodecaborate anion, $[B_{12}(CN)_{12}]^{2-}$, has been prepared by a microwave-promoted palladium-catalyzed cyanation reaction and isolated for the first time. Characterization of $[B_{12}(CN)_{12}]^{2-}$ by NMR (^{11}B, ^{1}H, and ^{13}C), liquid chromatography-mass spectrometry (LC-MS), high-resolution mass spectrometry (HRMS), and infrared spectroscopy (IR), is reported along with the single-crystal X-ray structures of $(CH_3CN)_3Cu[\mu\text{-}B_{12}(CN)_{12}]Cu(NCCH_3)_3$ and $[Et_4N]_2[B_{12}(CN)_{12}]$. The exhaustive acid-catalyzed hydrolysis of $[B_{12}(CN)_{12}]^{2-}$ was attempted, but only the hydrolysis of up to two of the cluster's CN ligands was observed by MS. Preliminary studies suggest that heavily cyanated derivatives of $[CB_{11}H_{12}]^{-}$ and $[B_{10}H_{10}]^{2-}$ can also be prepared by microwave-promoted palladium-catalyzed cyanation reactions. In addition, the electronic stability of functionalized derivatives of $[B_{10}H_{10}]^{2-}$ has been explored computationally using density functional theory (DFT).

TABLE OF CONTENTS

1. INTRODUCTION 1

1.1 BORON CLUSTERS: $[B_{12}H_{12}]^{2-}$ AND ITS RELATIVES 1

1.2 APPLICATIONS OF BORON CLUSTERS 5

1.3 BATTERY ELECTROLYTES 11

1.4 DERIVATIZATION OF BORON CLUSTERS 19

1.5 THIS WORK 24

2. RESULTS AND DISCUSSION 25

2.1 SYNTHESIS OF $[B_{12}(CN)_{12}]^{2-}$ 25

2.2 $[B_{12}(CN)_{12}]^{2-}$ CRYSTAL STRUCTURE 28

2.3 $[B_{12}(CN)_{12}]^{2-}$ STABILITY AND HYDROLYSIS 31

2.4 SYNTHESIS OF $[CB_{11}H_6(CN)_6]^-$ 32

2.5 ATTEMPTED SYNTHESIS OF $[CHB_{11}(CN)_{11}]^-$ 34

2.6 SYNTHESIS OF $[B_{10}(CN)_{10}]^{2-}$ 35

2.7 $[B_{10}(CN)_{10}]^{2-}$ STABILITY 36

3. CONCLUSION 40

3.1 SUMMARY OF RESULTS 40

3.2 FUTURE WORK 41

4. EXPERIMENTAL 42

4.1 EXPERIMENTAL PROCEDURES 42

4.2 SYNTHETIC PROCEDURES 43

4.3 X-RAY DIFFRACTION DETAILS 47

4.4 COMPUTATIONAL DETAILS 48

5. ACKNOWLEDGMENTS 50

6. REFERENCES 51

7. APPENDIX A: SUPPORTING INFORMATION 61

7.1 RELEVANT SPECTRA 61

7.2 X-RAY DIFFRACTION DATA 85

7.3 OPTIMIZED GEOMETRIES 99

8. APPENDIX B: TABLE OF REACTIONS 103

TABLE OF FIGURES

FIGURE 1. Examples of borane structures: borane, BH_3; diborane(6), B_2H_6; tetraborane(10), B_4H_{10}; pentaborane(9), B_5H_9; *closo*-decaborate, $[B_{10}H_{10}]^{2-}$; and *closo*-carbadodecaborate $[CB_{11}H_{12}]^-$. 1

FIGURE 2. Structure of diborane(6) highlighting the antisymmetric 3c-2e BHB bonding MO. 2

FIGURE 3. Icosahedral structure of *closo*-$[B_{12}H_{12}]^{2-}$. 3

FIGURE 4. MOs exhibiting a high degree of electron delocalization in $[B_{12}H_{12}]^{2-}$ HOMO–15, $[B_{12}H_{12}]^{2-}$ HOMO–24, $[B_{10}H_{10}]^{2-}$ HOMO–15, and $[B_{10}H_{10}]^{2-}$ HOMO–26.. 4

FIGURE 5. Parallel fission processes induced in ^{10}B upon the capture of a thermal neutron. 6

FIGURE 6. Schematic of a rechargeable LIB. 11

FIGURE 7. Structures of $[B_{10}X_{10}]^{2-}$ and $[B_{12}X_{12}]^{2-}$ where X = F, X = SCN, X= CN, and X = BO. 16

FIGURE 8. Temperature-dependent conductivity of Na^+ ions in $Na_2[B_{12}H_{12}]$ and $Na_2[B_{10}H_{10}]$ compared to $Na_2[B_{12}H_{12}]_{0.5}[B_{10}H_{10}]_{0.5}$ (labeled as 1:1). Structure of $Na_2[B_{12}H_{12}]_{0.5}[B_{10}H_{10}]_{0.5}$ (simplified, fcc framework) in the high-T phase showing the tetrahedral and octahedral geometries of the partially-occupied cation sites. 18

FIGURE 9. Homoperfunctionalized derivatives of $[B_{12}H_{12}]^{2-}$. 20

FIGURE 10. Palladium-catalyzed Rosenmund-von Braun reaction by Sakamoto and Ohsawa on aryl halide substrates. Palladium-catalyzed cross-coupling reaction by Rosenbaum et al. on carborane substrates. 22

FIGURE 11. Evaluation of conditions for the cyanation of B_{12} with varying solvents and palladium catalysts.. 26

FIGURE 12. Conditions for the preparation of the percyanated dianion, $[B_{12}(CN)_{12}]^{2-}$, from $[B_{12}I_{12}]^{2-}$ using an intermediate iodine removal step. 28

FIGURE 13. Single-crystal structure of $(CH_3CN)_3Cu[\mu\text{-}B_{12}(CN)_{12}]Cu(NCCH_3)_3$. 29

FIGURE 14. Single-crystal structure of $[Et_4N]_2[B_{12}(CN)_{12}]$. 30

FIGURE 15. Structures of the B_{10} cluster with thiocyanate ligands coordinating from the nitrogen atoms and the sulfur atoms. 38

1. INTRODUCTION

1.1 Boron Clusters: $[B_{12}H_{12}]^{2-}$ and its Relatives

Boron is one of only a few elements, aside from carbon, that can form unlimited molecular networks through homonuclear covalent bonding. However, the valency of boron leads to the formation of unique structural motifs that appear exotic to many organic chemists and excite group theorists. One useful yet seemingly-exotic set of compounds, comprised of boron and hydrogen, are known as boranes; stable boranes typically have partial or complete deltahedral geometries and generalized formulas of B_nH_{n+4} (*nido*-boranes), B_nH_{n+6} (*arachno*-boranes), and $[B_nH_n]^{2-}$ (*closo*-borates). Carbon vertices may also be incorporated into many of these polyhedral boron structures, leading to the class of compounds known as carboranes with generalized formulas of $[CB_nH_{n+1}]^-$ and $C_2B_nH_{n+2}$.[1]

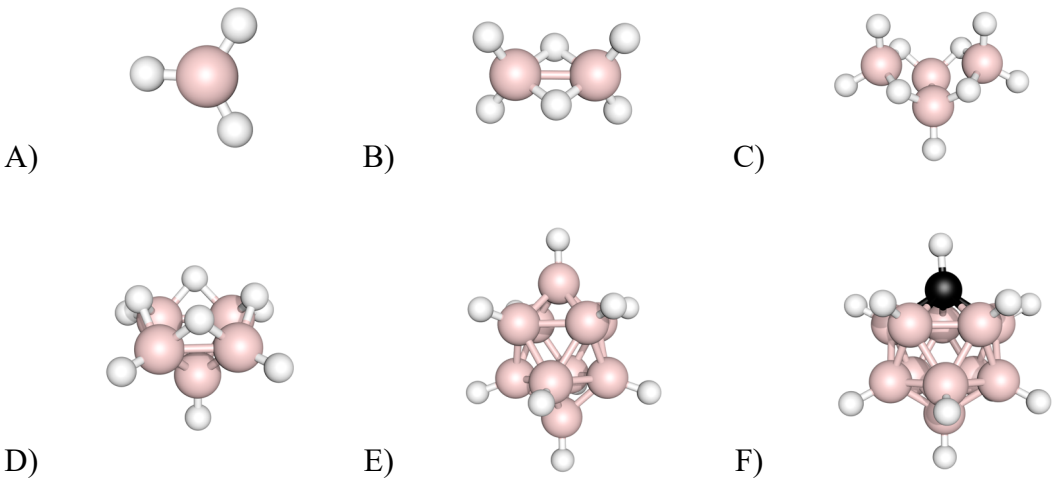

Figure 1. Examples of borane structures: **(A)** borane, BH_3; **(B)** diborane(6), B_2H_6; **(C)** tetraborane(10), B_4H_{10}; **(D)** pentaborane(9), B_5H_9; **(E)** *closo*-decaborate, $[B_{10}H_{10}]^{2-}$; and **(F)** *closo*-carbadodecaborate $[CB_{11}H_{12}]^-$.

While hydrocarbons exhibit two-center two-electron (2c-2e) bonding (i.e. traditional covalent bonds), boranes form electron-deficient three-center two-electron (3c-2e) bonds. The model of 3c-2e bonding in boron compounds was proposed by Lipscomb in 1954 and has been used to explain the unusual geometry of compounds like diborane, $B_2H_4(\mu\text{-}H_2)$, in which the two boron atoms are bridged by hydrogen atoms.[2] Formally, these BHB 3c-2e bonds involve the construction of three molecular orbitals (MOs) from the linear combinations of two boron-based sp^x hybrid orbitals (ψ_{B1} and ψ_{B2}) and the hydrogen atom's 1s atomic orbital (ψ_H):[3]

$$\psi_1 = \frac{1}{2}\psi_{B1} + \frac{1}{2}\psi_{B2} + \frac{1}{\sqrt{2}}\psi_H \quad (1)$$

$$\psi_2 = \frac{1}{\sqrt{2}}(\psi_{B1} - \psi_{B2}) \quad (2)$$

$$\psi_3 = \frac{1}{2}\psi_{B1} + \frac{1}{2}\psi_{B2} - \frac{1}{\sqrt{2}}\psi_H \quad (3)$$

In BHB 3c-2e bonds, ψ_1 is bonding and is the highest occupied molecular orbital (HOMO), ψ_2 is nonbonding and is the lowest unoccupied molecular orbital (LUMO), and ψ_3 is antibonding.

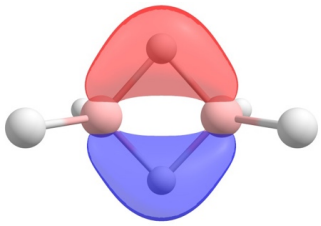

Figure 2. Structure of diborane(6) highlighting the antisymmetric 3c-2e BHB bonding MO.

In diborane and other small boron compounds, these 3c-2e bonds are relatively unstable making the resulting species quite pyrophoric. However, boron's capacity for 3c-

2e bonding allows for the assembly of complete or fragmented borane polyhedra that are stabilized by electron delocalization. One of the most famous examples of such a structure is the dodecahydro-*closo*-dodecaborate dianion, *closo*-$[B_{12}H_{12}]^{2-}$, which exhibits perfect icosahedral symmetry (I_h point group) and incredible electronic and thermal stability. The existence of $[B_{12}H_{12}]^{2-}$ as a stable species was first postulated by Longuet-Higgens and Roberts in 1955,[4] and the first method for its synthesis was established by Hawthorne and Pitocchelli shortly thereafter.[5]

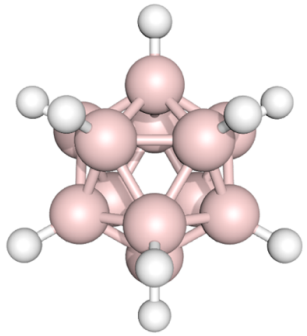

Figure 3. Icosahedral structure of *closo*-$[B_{12}H_{12}]^{2-}$. Note: the lines in the boron skeleton represent connectivity between atoms, not 2c-2e bonds.

The atoms in the B_{12} cluster contain a total of 50 valence electrons, which contribute to the formation of both external MOs (B–H bonds) and skeletal MOs (B–B bonds); 24 electrons contribute to the formation of the external bonds to hydrogen while the 26 remaining electrons remain to form the boron cage's delocalized skeletal bonds. The number of electrons in a stable boron cluster can also be determined by Wade's rules for deltahedral molecules (also known as polyhedral skeletal electron pair theory or PSEPT)

which states that a stable *closo*-borane will contain $4n + 2$ electrons, of which, $n + 1$ pairs will be involved in skeletal bonding (where n is the total number of boron vertices).[6]

While the simplicity of PSEPT makes it an incredibly useful tool for electron counting and determining stability in boron clusters, MO theory can facilitate a more quantitative analysis of electron behavior. Straightforward density functional theory (DFT) calculations at the PBE0/def2-TZVP level of theory (see **Section 4.4**) allow for the visualization of MOs such as HOMO–15 and HOMO–24 which demonstrate significant electron delocalization within the B_{12} cluster's boron cage. This electron delocalization can

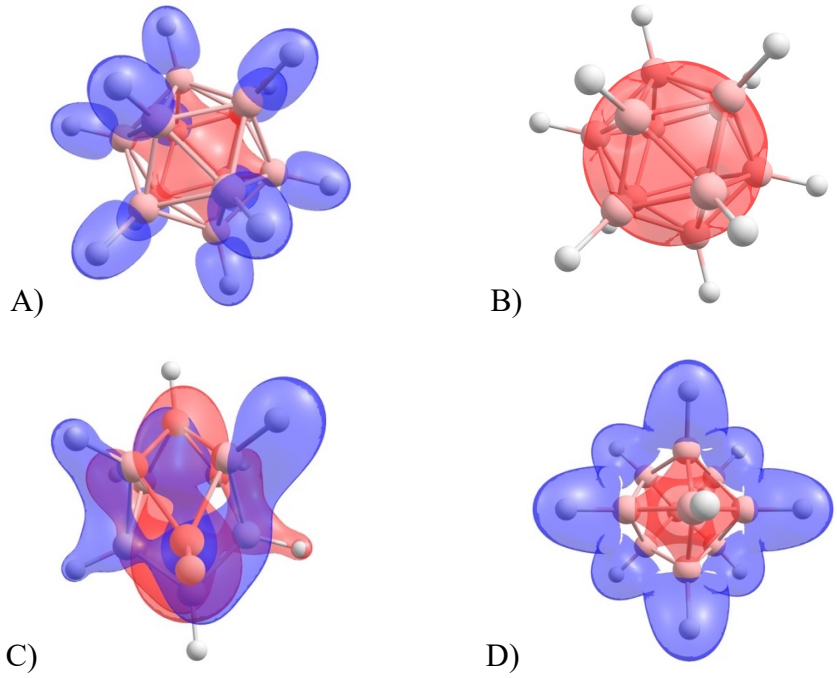

Figure 4. MOs exhibiting a high degree of electron delocalization in **(A)** $[B_{12}H_{12}]^{2-}$ HOMO–15, **(B)** $[B_{12}H_{12}]^{2-}$ HOMO–24, **(C)** $[B_{10}H_{10}]^{2-}$ HOMO–15, and **(D)** $[B_{10}H_{10}]^{2-}$ HOMO–26 (here the cluster is rotated to look down the C_4 axis of rotation).

also be observed in the 10-vertex analog of B_{12}, *closo*-$[B_{10}H_{10}]^{2-}$, in MOs such as HOMO–15 and HOMO–26. The large stability induced by electron delocalization is also evidenced

by these clusters' large HOMO-LUMO gaps (which are calculated to be 7.14 and 5.84 eV for the $[B_{12}H_{12}]^{2-}$ and $[B_{10}H_{10}]^{2-}$ clusters, respectively, at the PBE0/def2-TZVP level).

The electron delocalization in deltahedral borane skeletons has been described as three-dimensional (3D) sigma-aromaticity, or 'superaromaticity,' and has been explored theoretically and computationally via the same methods used to probe aromaticity in planar systems.[7] Examples of this include nucleus independent chemical shift (NICS) calculations (which yield a value of –28.4 at the CSGT-B3LYP/6-311+G** level).[8] Spherical aromaticity can also be theoretically determined through Hirsch et al.'s extension of Hückel's rule for aromaticity in planar systems: molecules with spherical (I_h) symmetry such as fullerenes, borane polyhedra, and other inorganic cage systems will exhibit aromaticity when they contain $2(n + 1)^2$ conjugated σ or π electrons.[9]

1.2 Applications of Boron Clusters

Due to the high energy density of boranes and the difficulty of managing high-energy fuels (HEFs) like liquid hydrogen, both the United States and Soviet Union governments began investing heavily in borane production after World War II. Through initiatives like Project Hermes (Army), Project ZIP (Navy Bureau of Aeronautics), and Project HEF (Air Force), the U.S. military aimed to produce commercial-scale HEFs, based on compounds like pentaborane (B_4H_9) and decaborane ($B_{10}H_{14}$), that could extend the flight range of jet aircraft.[10] Despite many millions of dollars in funding, most of these borane fuels did not perform as well as theoretical calculations suggested they should, the resulting exhausts were quite toxic, and there was little success towards the development

of an engine that could withstand their combustion byproducts (e.g. boron oxide and boron carbide).[11] Interest in borane fuels quickly dwindled. However, the U.S. military's funding for borane research opened the door for continued research into boron clusters with non-military applications ranging from pharmacology to materials science.

Over the past century, boron clusters have found many potential applications in medicine, the most well-studied of which is boron neutron capture therapy (BNCT).[12] Continued interest in BNCT has led to an increased focus on developing non-toxic, boron-containing drugs that can accumulate in tumoral tissue. Low-energy, neutron beam radiation (which is non-destructive to tissues) causes the non-radioactive boron-10 isotope to undergo alpha decay:[13]

$$^{10}\mathrm{B} + \mathrm{n}_{\mathrm{thermal}} \rightarrow [^{11}\mathrm{B}]^{*} \rightarrow \begin{cases} {}^{4}\alpha + {}^{7}\mathrm{Li}^{3+} + 2.79\ \mathrm{MeV}\ (6\%) \\ {}^{4}\alpha + [{}^{7}\mathrm{Li}^{3+}]^{*} + 2.31\ \mathrm{MeV}\ (94\%) \quad \rightarrow {}^{7}\mathrm{Li}^{3+} + \gamma\ (478\ \mathrm{keV}) \end{cases}$$

Figure 5. Parallel fission processes induced in ^{10}B upon the capture of a thermal neutron.[14]

The resultant radiation has a high linear energy transfer (α = 150 keV μm^{-1}, ^{7}Li = 174 keV μm^{-1}), leading to selective irradiation with a diameter of only a single cell (< 10 μm).[15] Thus far, only two drugs for BNCT have been approved for clinical testing: $Na_2[B_{12}H_{11}SH]$ (abbreviated as BSH) and (*L*)-4-boronophenylalanine (L-BPA). In the treatment of glioblastomas, BSH exhibits no toxic effects but is limited in its tumor selectivity; L-BPA, due to its similarity to amino acids, exhibits better selectivity than BSH but has a significantly lower boron density (only 5.2% by mass).[14] Current research has focused developing the next generation of BNCT drugs by combining the high neutron capture

cross-section of boron cluster derivatives with tumor-targeting biological moieties via hydrolytically stable linkages.[10] However, one large obstacle to finding these BNCT drug candidates is the limited library of feasible borane and carborane derivatives necessary for high-throughput screening.

Outside of BNCT, boron clusters have significant utility in cell imaging. Carboranes and metallacarboranes can be labeled with halogen radioisotopes for imaging via single-photon emission computed tomography (SPECT) and positron emission tomography (PET), or as tumor-seeking agents in targeted radionuclide cancer therapies. Heavily iodinated boron clusters have potential applications as non-toxic X-ray contrast agents as they can have significantly higher iodine contents than contrast agent currently on the market (e.g. water-soluble aryl triiodides).[10] Cholesterol-coupled boranes have been used for cell imaging via Raman spectroscopy as they generate unique bands in the cellular-Raman silent region.[16]

Boranes and carboranes have been explored for a wide range of pharmacological applications, including as hydrophobic pharmacophores in nuclear receptor ligands. These ligands have been shown to act as estrogen agonists, estrogen antagonists, selective estrogen-reuptake inhibitors (SERMs), retinoic acid receptor (RAR) agonists and antagonists, retinoic acid x receptor (RXR) agonists and antagonists, androgen antagonists, testosterone mimics, cholesterol mimics, transthyretin amyloidosis inhibitors, α-human thrombin inhibitors, and adenosine-based blood platelet function inhibitors.[17,18] Platinum(II) complexes with carborane ligands have also been explored as potential anticancer agents with the goal of producing new drugs with higher efficacy, broader activity, and lower toxicity compared to current platinum-based anticancer agents like

cisplatin.[10] A complete summary of the medical applications of boron clusters is beyond the scope of this thesis, but the quantity and breadth of work being done in this field is expanding rapidly.

Outside of medicine, boron clusters have found applications throughout materials science. One example of this is in the development of nonlinear optical (NLO) chromophores. Nonlinear optics, as a field, explores the interactions between intense electromagnetic fields and matter in systems that give rise to a modified field that differs from the incident field with regard to frequency, amplitude, phase, path, and/or polarization. This is formally described by:

$$\mu(E) = \mu_0 + \alpha E + \beta E^2 + \gamma E^3 \ldots \quad (4)$$

wherein E is the electric field component of the incident light, μ_0 is the permanent dipole moment, α is the polarizability, β is the first-order hyperpolarizability, γ is the second-order hyperpolarizability, and so on. One of the most important NLO effects, based on first-order hyperpolarizability β, is frequency doubling (also known as second harmonic generation or SHG). Frequency doubling involves the absorption of two same-frequency photons and the subsequent emission of a single photon at twice the energy and twice the frequency of the incident photons. This phenomenon is particularly useful in the development of photonic devices such as disks for optical information storage.[19]

Frequency doubling is typically observed in non-centrosymmetric molecules containing an electron-accepting group and an electron-donating group that are bridged by a π-conjugated linker, as this gives rise to higher first-order hyperpolarizability. Boron clusters have been explored for use in all parts of these NLO materials. B_{12} derivatives can be used as electron-donating groups due to their high degree of electron delocalization and

polarizability, while dicarborane derivatives can be used as electron-accepting groups. For organic linkers, increasing the π-conjugated system's length can increase hyperpolarizability but can also lead to a loss of the material's transparency in the laser operating wavelength region, thereby interfering with the material's NLO properties; carboranes-based linkers have been shown to exhibit extremely high first-order hyperpolarizability ($\leq 1226 \times 10^{-30}$ cm^5 esu^{-1}) while remaining transparent to the frequencies of incident light.[20]

Weakly coordinating anions (WCAs) are bulky anions with extremely low affinities for resident cations. WCAs are characterized by (1) a low degree of charge, (2) a high degree of charge delocalization, and (3) a high degree of kinetic and thermodynamic stability. Monoanionic clusters such as CB_{11} excel in these categories and have been shown to act as exceptional WCAs and extremely weak nucleophiles.[21] As such, CB_{11} derivatives have been used to stabilize highly-reactive electrophiles such as fullerene cations (e.g. HC_{60}^+ and C_{60}^+),[22] and even in the isolation of *tert*-butyl cations,[23] silylium cations (R_3Si^+),[24] and protonated arenes (e.g. $C_6H_7^+$).[25] Derivatives of the B_{12} cluster have also been shown to act as robust WCAs despite their dinegative charge.[26] Because of their low proton affinity, the conjugate acids of many of these boron clusters anions are categorized as superacids (a class of acids characterized by strengths greater than 100% sulfuric acid). Carborane acids, with the formula $H[CHB_{11}X_5Y_6]$ (X = H and Cl; Y= Cl, Br, and I), are the strongest isolable Brønsted acids (Hammett values ≥ -18). These acids can protonate fullerenes, even at low temperatures, without inducing the decomposition caused by other superacids such as "Magic Acid" (a Lewis-Brønsted mixture of $HFSO_3$ and SbF_5).[27]

Ionic liquids (ILs) are entirely ionic compounds that are liquid below ca. 100 ˚C, although ILs with melting points at or near room temperature are particularly sought-after. Ionic liquids are useful as designer solvents and liquid electrolytes, although the number of applications is growing quickly. Due to their capacity for derivatization, boron clusters are excellent, tunable WCAs for use as the anionic component of ionic liquids.[28] Boron cluster-containing ionic liquids have been produced with melting points which range from below –30 to over 95 ˚C.[29] Boron clusters can also act as versatile structural elements in liquid crystals for use in NLO materials as well as in ionic liquid crystals that function as positive $\Delta\varepsilon$ additives in nematic-phase mixtures for liquid crystal displays (LCDs).[30]

Carboranes with short DNA adapters have been assembled into functional nanoparticles.[31] Polyhedral boron species have been widely used in catalytic organic transformations,[32] and have more recently been used for a broader range of applications in catalysis including surface functionalization of catalytic nanoparticles[33] and the self-assembly of highly monodisperse magnetic nanocomposites.[34] Various boron clusters have been explored for use in the synthesis of molecular architecture, nanostructures, and even nanomachines.[35] The incorporation of boron clusters into polymer backbones has led to the production of polymers with specialized applications due to their high thermal stabilities while functionalized carboranes have been incorporated into various coordination polymers and metal-organic frameworks (MOFs).[36–38] Commercially, carboranes have been used as cation detectors in ion-selective electrodes and stationary phase materials for high-temperature gas chromatography (GC) while borates are commonly used in vehicular airbag propellant systems.[39] As before, a complete summary of the non-medical

applications of boron clusters is beyond the scope of this thesis, but the quantity and breadth of work being done in these areas are expanding rapidly.

1.3 Battery Electrolytes

In the years leading up to Goodenough, Whittingham, and Yoshino's receipt of the 2019 Nobel Prize in Chemistry for the development of lithium-ion batteries (LIBs), research on these now-ubiquitous rechargeable batteries has grown immensely. This research has been motivated by LIBs' high energy-density, high operating voltage, low self-discharge, lack of memory effect, portability, and increasing use in everyday

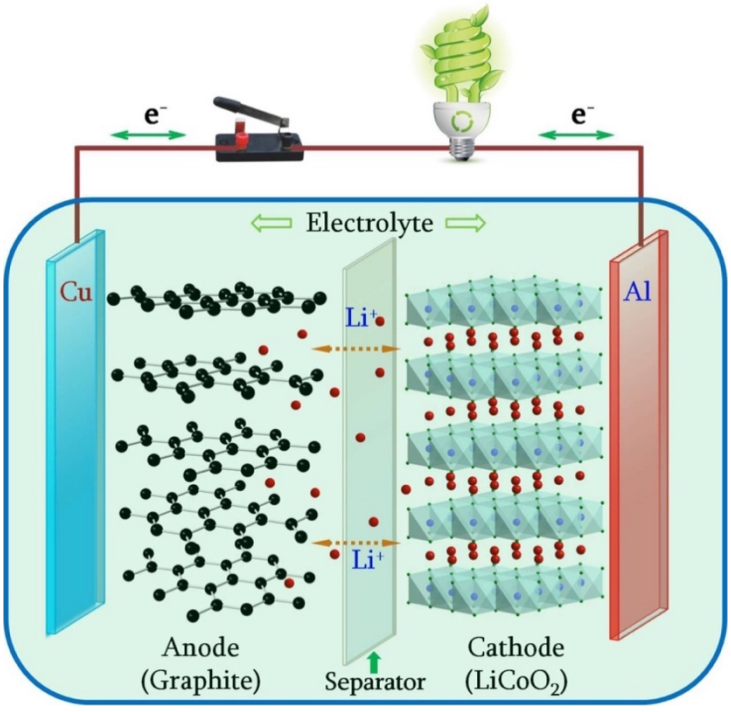

Figure 6. Schematic of a rechargeable LIB. In this battery, Li^+ ions move from the cathode to the anode when charging; Li^+ ions move in the reverse direction when discharging. Reproduced from Liu et al.[41] Copyright 2015, the authors, published by Elsevier Ltd.

electronics and electric transportation.[40] As global energy production from coal and petroleum-based fuels continue to result in the emission of unsustainable quantities of greenhouse gasses, improving electrochemical energy storage is especially important for maximizing the utility of the energy produced by intermittent and 'greener' energy sources such as wind and solar.

LIB cells commonly use solid-state cathodes with intercalated lithium (such as $LiCoO_2$), graphite anodes, and polymeric or solution-phase electrolytes. Conventional liquid electrolytes consist of halogenated lithium salts, such as $LiPF_6$, in an organic solvent like ethylene carbonate. Many of these electrolyte solutions have led to significant concerns regarding consumer safety, public health, environmental impact, and battery operation.[42] Principally, this is because organic solvents are flammable and thermal runaway in LIB systems often leads to the formation of toxic organohalides[43] and the release of hydrohalic gasses.[44] Because of this, researchers have begun searching for halogen-free superhalogens (salts with a vertical detachment energy (VDE) for the anionic moiety that is greater than the VDE of any halogen atom), as potential alternatives. Giri et al. identified lithium carborane salts as a particularly intriguing class of halogen-free superhalogens, as they meet the set of requirements established by the authors for improving LIB electrolytes: (1) halogens should be removed from electrolytes to mitigate safety concerns, (2) the binding energy between the electrolyte's anionic moiety and Li^+ should be reduced to minimize interference with ion conduction, and (3) the electrolyte's affinity for water should be reduced to extend battery lifetime.[45]

In 2016, Zhao et al. presented the compound $[B_{12}(CN)_{12}]^{2-}$ as a potential candidate for use as an electrolyte in metal-ion batteries due to its electron binding energy,

dissociation energy with lithium ions, and thermal stability.[46] Specifically, $[B_{12}(CN)_{12}]^{2-}$ exhibited extremely high electron binding energies (i.e. 5.28 eV for the outermost electron at the B3LYP/6-31+G(d,p) level). This places the second electron binding energy of $[B_{12}(CN)_{12}]^{2-}$ only ca. 1.7 eV below that of the first electron in current, singly-charged LIB electrolytes (e.g. 7.03 eV for PF_6^- at the PBE0/6-311+G(d,p) level).[47] This also makes $[B_{12}(CN)_{12}]^{2-}$ the second-most electronically stable multiply charged anion (MCA) known, with calculated electron binding energies exceeded only by those of the yet-unsynthesized boronylated cluster, $[B_{12}(BO)_{12}]^{2-}$.[48]

	$[B_{12}(BO)_{12}]^{2-}$	$[B_{12}(CN)_{12}]^{2-}$	$[B_{12}(SCN)_{12}]^{2-}$	$[B_{12}F_{12}]^{2-}$	$[B_{12}H_{12}]^{2-}$
ΔE_1	9.33 [(a)]	8.76 [(a)]	5.65 [(b)]	5.67 [(a)]	4.45 [(a)]
ΔE_2	5.89 [(a)]	5.40 [(a)]	3.28 [(b)]	1.39 [(a)]	0.96 [(a)]

Table 1. Electron binding energies in eV of the first and second electrons (ΔE_1 and ΔE_2 respectively) for the perfunctionalized B_{12} cluster at the (a) PBE0/def2-TZVP level[48] and (b) B3LYP/6-31+G(d,p) level.[49]

In liquid electrolytes, a low dissociation energy with metal ions is important for maximizing the concentration, and therefore conduction, of metal ions in solution.[50] The percyanated B_{12} cluster exhibits relatively low dissociation energies with lithium ions (i.e. 4.66 and 6.83 eV for the first and second Li^+ ions in a dilithium salt at the B3LYP/6-31+G(d,p) level). These dissociation energies are defined by Zhao et al. as:

$$\Delta E_{Li1} = E(Li^+) + E(LiX^-) - E(Li_2X) \quad (5)$$

$$\Delta E_{Li2} = E(Li^+) + E(X^{2-}) - E(LiX) \quad (6)$$

where X is the anionic moiety being studied.[46]

	$Li_2[B_{12}(CN)_{12}]$	$Li_2[B_{12}H_{12}]$	$Li[CB_{11}H_{12}]$	$LiPF_6$
ΔE_{Li1}	4.66 [(a)]	5.91[(a)]	5.08 [(b)]	5.73 [(b)]
ΔE_{Li2}	6.83 [(a)]	9.03 [(a)]	—	—

Table 2. Dissociation energies in eV of anionic species with one and two lithium ions (ΔE_{Li1} and ΔE_{Li2} respectively) at the (a) B3LYP/6-31+G(d,p) level[49] and (b) wB97XD/6-311+G(d) level.[45]

Zhao et al. also examined the percyanated B_{12} cluster's dissociation energies with magnesium ions.[46] Not only is the elemental abundance of magnesium in the Earth's crust over 1000 times greater than that of lithium, but magnesium can be recovered from seawater whereas lithium is necessarily a product of mineral extraction.[51] Therefore, the development of effective secondary magnesium batteries would have a significant impact on the cost, safety, and environmental toll of chemical energy storage. In addition to its abundance, magnesium (which can be used as a solid metal anode) is non-dendritic upon battery cycling and has a high volumetric capacity (3832 mA h cm^{-3} compared to 2036 mA h cm^{-3} for lithium).[52] Conversely, magnesium has strong interactions with many potential electrolytes and poor capacity for intercalation into many cathode substrates due to its bivalency.[53,54] The use of electrolytes like PF_6^- also leads to the formation of surface films comprised of insoluble salts (i.e. electrode passivation). In electrochemical cells, electrode passivation was avoided through the use of Grignard reagents (RMgX in ether; R = alkyl or aryl; and X = halogen) as electrolytes due to their facilitation of the reversible deposition of magnesium.[55] While this leads to high anodic stability, the reductive capacity of Grignard reagents can cause severe damage to the metals used in battery casings and current collectors, thereby limiting the practical electrochemical window of the cell and raising safety concerns. Magnesium-carborane salts such as $Mg[CB_{11}H_{12}]_2$ are some of the

first halogen-free (non-Grignard), simple-type salts found to be compatible with Mg metal, oxidatively stable, and non-corrosive.[56]

Wade's rules predict that monoanionic monocarboranes will be more electronically stable than their dianionic counterparts; however, the stability induced in the CB_{11} cluster via percyanation is so great that the $[CB_{11}(CN)_{12}]^{2-}$ dianion is calculated to be more stable than the $[CB_{11}H_{12}]^{-}$ monoanion by more than 1.0 eV. This stability, combined with a low dissociation energy with magnesium ions, also makes $[CB_{11}(CN)_{12}]^{2-}$ a good theoretical candidate for use in magnesium battery electrolytes.[46]

	$Mg[B_{12}(CN)_{12}]$	**$Mg[B_{12}(SCN)_{12}]$**	**$Mg[B_{12}H_{12}]$**	**$Mg[CB_{11}(CN)_{12}]$**	**$Mg[CB_{11}H_{12}]_2$**
ΔE_{Mg}	18.29	18.37	21.19	19.70	20.38

Table 3. Metal dissociation energies in eV of anionic species with Mg^{2+} ions (ΔE_{Mg}) at the B3LYP/6-31+G(d,p) level.[49]

Some researchers have suggested alternative ligands to the one studied in clusters like $[B_{12}(CN)_{12}]^{2-}$ and $[CB_{11}(CN)_{12}]^{2-}$.[49] As an example, Fang and Jena proposed the use of the isothiocyanate ligand, SCN, as it could potentially reduce the B_{12} cluster's dissociation energy with metal ions. To explore this, the authors used a more comprehensive model for metal-electrolyte interactions in order to account for ligand distortion due to metal ion binding, i.e.:

$$\Delta E_{Mg} = E_{distort} + E(Mg^{2+}) - E(MgX) \qquad (7)$$

While these calculations yield very similar metal binding energies for $[B_{12}(CN)_{12}]^{2-}$ and $[B_{12}(SCN)_{12}]^{2-}$ with both Mg^{2+} and Li^{+} ions, the calculated electron binding energy of the

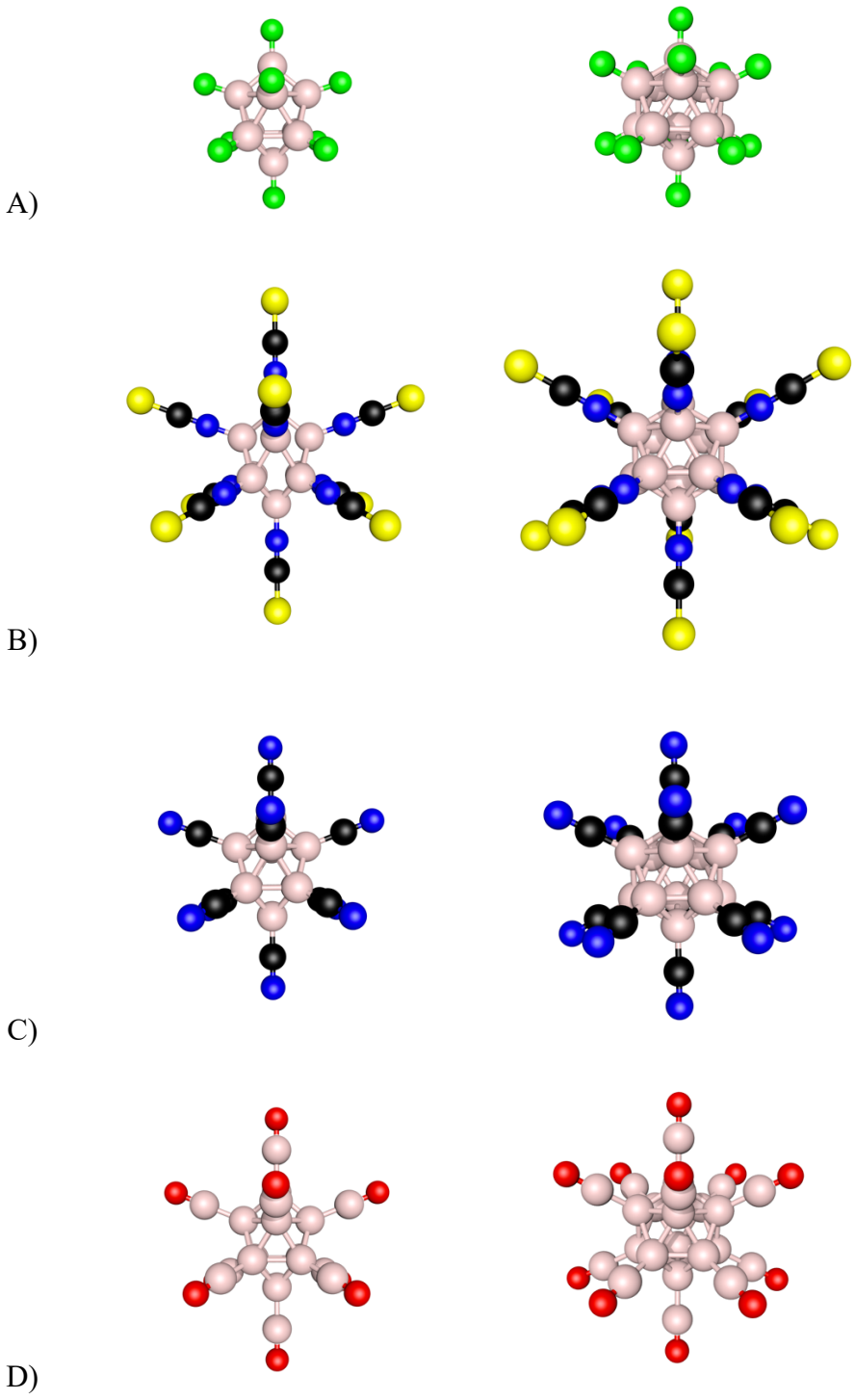

Figure 7. Structures of $[B_{10}X_{10}]^{2-}$ and $[B_{12}X_{12}]^{2-}$ where **(A)** X = F, **(B)** X = SCN, **(C)** X= CN, and **(D)** X = BO.

perisothiocyanated B_{12} cluster is 2.0 eV lower than that of the percyanated B_{12} cluster (an almost 40% reduction).

Calculations of the electron binding energies for the perfunctionalized B_{12} and CB_{11} clusters were expanded upon by Zhong et al. in their comprehensive computational investigation of the properties of $[B_nX_n]^{2-}$ and $[CB_{n-1}X_n]^-$ clusters (n = 5–10, X = H, F, and CN) for potential use in LIB electrolytes (B3LYP/6-31+G(d,p) level).[57] Of the dianions studied, $[B_{10}(CN)_{10}]^{2-}$ exhibited the highest degree of stability with a binding energy of 4.13 eV for the outermost electron; of the studied monoanions, $[CB_9H_{10}]^-$ exhibited the highest degree of stability with an electron binding energy of 4.45 eV. Computational studies on the stability of the boronylated and isothiocyanated B_{10} clusters, $[B_{10}(BO)_{10}]^{2-}$ and $[B_{10}(SCN)_{10}]^{2-}$, have not previously been performed.

When it comes to the improvement of metal-ion batteries with regard to consumer safety, beyond the synthesis of halogen-free electrolytes with high stability and low metal dissociation energies, the development of solid-state electrolytes (SSEs) is of extremely high priority for use in secondary lithium, magnesium, and sodium battery systems. SSEs have demonstrated comparable ionic conductivities and improved charge-transport efficiency when compared to solution-phase electrolytes.[58] In recent years, boron clusters have been explored as a new class of SSEs due to their unparalleled superionic conductivity — a result of large interstitial pathways for ion transport created by the size and quasi-spherical geometry of boron cluster anions. However, this ionic conductivity, which can be as high as 0.1 S cm^{-1}, is only present above the SSE's order-disorder phase-transition temperature (ca. 530 K for $Na_2[B_{12}H_{12}]$, 380 K for $Na[CB_{11}H_{12}]$, and 370 K for $Na_2[B_{10}H_{10}]$); therefore, introducing disorder to stabilize the cation-vacancy-rich high-T

phase at or below room temperature is extremely important for the implementation of such SSEs in practical battery systems.[59]

Stabilization of the disordered phase in boron cluster-based SSEs can be achieved through: (1) finding a *closo*-borate anion host that exhibits high ionic conductivity in the disordered high-T phase, (2) finding a *closo*-borate anion whose structure and size are similar to that of the host anion, and (3) partially incorporating it into the host material to form a disordered structure, thereby stabilizing the cation-vacancy-rich high-T phase at lower temperatures.[60] The mixed-borate salt $Na_2[B_{12}H_{12}]_{0.5}[B_{10}H_{10}]_{0.5}$ has been shown to be effective as an SSE in stable 3 V all-solid-state sodium-ion batteries. This borate-based electrolyte was shown to exhibit a large electrochemical window, maintain high ionic conductivity for Na^+ ions even near room temperature, and be stable against sodium metal anodes.[61] Recently, Kim et al. demonstrated that the mixed carborane salt,

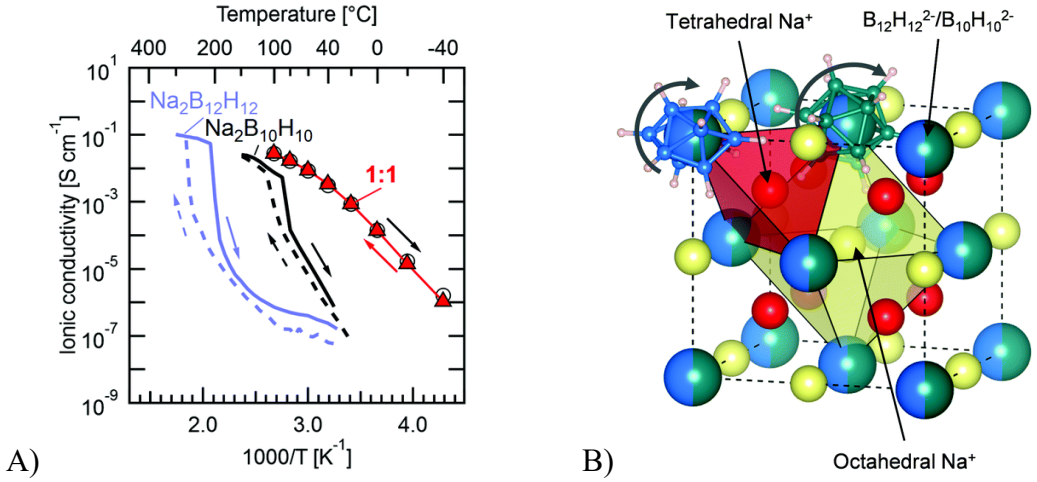

Figure 8. (A) Temperature-dependent conductivity of Na^+ ions in $Na_2[B_{12}H_{12}]$[62] and $Na_2[B_{10}H_{10}]$[63] compared to $Na_2[B_{12}H_{12}]_{0.5}[B_{10}H_{10}]_{0.5}$ (labeled as 1:1). **(B)** Structure of $Na_2[B_{12}H_{12}]_{0.5}[B_{10}H_{10}]_{0.5}$ (simplified, fcc framework) in the high-T phase showing the tetrahedral and octahedral geometries of the partially-occupied cation sites. Reproduced from Duchêne et al.[61] Copyright 2017, the authors. Published by the Royal Society of Chemistry.

$Li[CB_9H_{10}]_{0.7}[CB_{11}H_{12}]_{0.3}$, can be an effective electrolyte in high-energy-density, all-solid-state lithium-sulfur batteries. This carborane-based electrolyte was shown to exhibit exceptionally high ionic conductivity for Li^+ ions and to be stable against lithium metal anodes.[60] The use of boron clusters in SSEs has also been the subject of a recent review.[64]

1.4 Derivatization of Boron Clusters

The functionalization of boron clusters allows their specific properties to be tuned to meet the requirements of a broad range of both established and proposed applications. The derivatization of aromatic boron clusters like $[B_{12}H_{12}]^{2-}$ frequently resembles known derivatization methods for aromatic organic molecules, such as the electrophilic aromatic substitution (EAS) of benzene. However, reactions conditions infrequently translate directly from arene to boron cluster systems.

Because of the large numbers of potential regioisomers of any partially functionalized or multiply functionalized icosahedral boron clusters, monofunctionalized and perfunctionalized derivatives of the B_{12} cluster are particularly sought-after synthetic targets. This is the case for functionalization of the B_{10} cluster as well, although the lower degree of symmetry in the cluster (D_{4d} point group) also necessitates differentiating between functionalization at one of the antipodal vertices (positions 1 or 10) versus the vertices in between (positions 2–9). The directing effect of carbon in carboranes like $[CB_{11}H_{12}]^-$ also allows for isomerically-pure hexafunctionalization (positions 6–12) and undecafunctionalization (at non-carbon vertices: positions 2–12). However, examples of uniformly perfunctionalized boron clusters are currently quite limited.

For the B_{12} cluster, permethylated, perfluorinated, perchlorinated, perbrominated, periodinated, and perhydroxylated derivatives can be synthesized directly from $[B_{12}H_{12}]^{2-}$, whilst ester, carbamate, carbonate, and ether derivatives can, in turn, be prepared from $[B_{12}(OH)_{12}]^{2-}$.[65] Derivatives of the B_{10} cluster are even more limited. Perchlorinated,

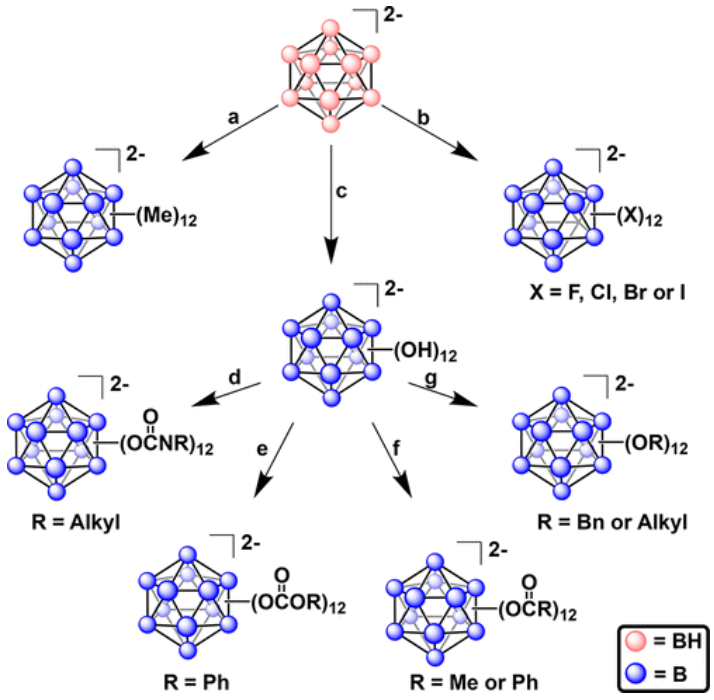

Figure 9. Homoperfunctionalized derivatives of $[B_{12}H_{12}]^{2-}$. Reproduced with permission from Axtell et al.[66] Copyright 2018, American Chemical Society.

perbrominated, and periodinated derivatives can be synthesized directly from $[B_{10}H_{10}]^{2-}$.[67] $[B_{10}(OH)_{10}]^{2-}$ has not yet been synthesized which significantly limits synthetic routes for further perfunctionalization. The perfluorinated B_{10} cluster has not yet been synthesized either, although its properties have been explored via DFT.[57,68] Many of these perfunctionalized B_{10} species have also been included in a patent focused on the

development of improved LIB systems with intrinsic pulse overcharge protection, including the yet-unsynthesized $[B_{10}X_{10}]^{2-}$ clusters (X = F, OH, and OCH_3).[69]

As described in **Section 1.3**, heavily cyanated and heavily boronylated boron clusters are highly desirable synthetic targets. No synthetic methods for the boronylation of any boron clusters have yet been reported. The isolation of any percyanated boron clusters has also not previously been reported, in part due to difficulties arising from the steric hindrance and deactivating effects associated with the addition of each cyano group, as well as from the difficulty of separating a mixture of poly- and percyanated clusters.

Partially cyanated derivatives of the B_{12} cluster were first prepared by Trofimenko and Cripps in the 1960s by UV-irradiation (low-pressure mercury lamp) of aqueous solutions of a perhalogenated B_{12} cluster in the presence of KCN.[70,71] The authors suggested that the formation of these cyanated derivatives likely involves the photo-induced heterolysis of the B-X bond, leaving the electrophilic boron cluster to react with any solubilized bases such as cyanide. More recently, Mayer et al. employed a similar approach in their synthesis of $[B_{12}(CN)_{12}]^{2-}$, utilizing UV-irradiation (medium-pressure mercury lamp) to produce cyanated derivatives of $[B_{12}I_{12}]^{2-}$ in an aqueous solution.[72] This resulted in a mixture, $[B_{12}(CN)_{12-n}(OH)_n]^{2-}$ ($n \leq 5$), in which the mole fraction of $[B_{12}(CN)_{12}]^{2-}$ was very low (ca. 10-15% by MS). Very recently, Meyer at al. published an updated synthetic procedure that used UV-irradiation (medium-pressure mercury lamp) to produce a precipitate composed of a 1:1 mixture of $[B_{12}(CN)_{12}]^{2-}$ and $[B_{12}(CN)_{11}I]^{2-}$ that was co-crystallized as a $[PPh_4]^+$ salt.[73] The use of UV-irradiation for the percyanation of B_{12} from various perhalogenated precursors has also been the subject of a recent dissertation.[74]

UV-irradiation is not the only method for the cyanation of boron clusters though. While never before tested with the B_{12} cluster, microwave irradiation (MWI) has been shown to be effective in the mono- and di-cyanation of boron vertexes in certain halogenated carboranes. For example, $[12\text{-}CB_{11}H_{11}(CN)]^-$ and $[7,12\text{-}CB_{11}H_{10}(CN)_2]^-$ can be synthesized from $[12\text{-}CB_{11}H_{11}]^-$ and $[7,12\text{-}CB_{11}H_{10}I_2]^-$ respectively via copper-promoted, palladium-catalyzed cross-coupling reactions under MWI.[75,76] This process is analogous to the cyanation of aryl halides using CuCN and a palladium(II) catalyst (e.g. the palladium-catalyzed Rosenmund-von Braun reaction), which is a well-established synthetic transformation in organic chemistry.[77–79]

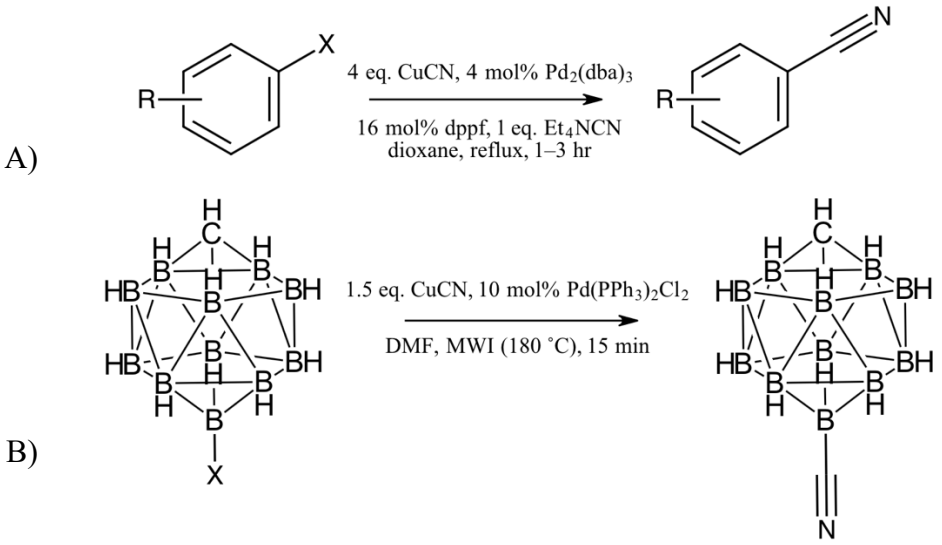

Figure 10. (A) Palladium-catalyzed Rosenmund-von Braun reaction by Sakamoto and Ohsawa on aryl halide substrates.[79] $Pd_2(dba)_3$ = tris(dibenzylideneacetone)dipalladium(0), dppf = diphenylphosphinoferrocene. **(B)** Palladium-catalyzed cross-coupling reaction by Rosenbaum et al. on carborane substrates.[75] DMF = *N,N*-dimethylformamide.

A number of other methods for the monocyanation of boron clusters have also been developed. The cyanation of the CB_{11} cluster's carbon vertex via PhOCN gives $[1\text{-}NC\text{-}CB_{11}X_{11}]^-$ (using $CsLi[CB_{11}X_{11}]$ as a precursor and where X = H, F, Cl, Br, and

I).[80] More unexpectedly, carbon-extrusion/cage-contraction of $[1\text{-}H_2N\text{-}CB_{11}F_{11}]^-$ has been shown to lead to the formation of $[3\text{-}B_{11}F_{10}(CN)]^{2-}$.[81] The synthesis of $[12\text{-}CB_{11}H_{11}(CN)]^-$ can also be achieved by producing a zwitterionic aryliodonium derivative of the CB_{11} cluster and reacting it with CN^-. This synthetic procedure can also be used for the preparation of $[6\text{-}CB_9H_9(CN)]^-$ and $[10\text{-}CB_9H_9(CN)]^-$ from $[CB_9H_{10}]^-$,[82] as well as for the preparation of $[1\text{-}B_{10}H_9(CN)]^{2-}$ from $[B_{10}H_{10}]^{2-}$.[83] No other methods for the cyanation of the B_{10} cluster are currently known.

There exist various methods for the monocyanation of the C_2B_{10} cluster, although very few of the many potential product regioisomers have yet been synthesized. Metal-catalyzed cross-coupling under MWI gives the *ortho*, *meta*, and *para* regioisomers of $9\text{-}C_2B_{10}H_{11}(CN)$ from the corresponding iodinated precursors.[84] These synthetic transformations can also be achieved via nucleophilic attack of an aryliodonium-derivatized precursor (position 9 for *o*/*m*- and position 2 for *p*-carborane), yielding $9\text{-}o\text{-}C_2B_{10}H_{11}(CN)$, $9\text{-}m\text{-}C_2B_{10}H_{11}(CN)$, and $2\text{-}p\text{-}C_2B_{10}H_{11}(CN)$.[85] The use of a diazonium-functionalized precursor (position 3) instead of aryliodonium has also been shown to lead to the formation of $9\text{-}o\text{-}C_2B_{10}H_{11}(CN)$.[86]

Using ion-trap triple mass spectrometry, Mayer et al. showed that $[B_{12}(CN)_{12}]^{2-}$ can act as a precursor for generating the monoanionic fragment, $[B_{12}(CN)_{11}]^-$, which exhibits sufficient superelectrophilicity to covalently bind to argon at room temperature.[72] Only a single, non-cationic species containing argon, HArF, had previously been isolated and doing so required the use of a low-temperature matrix. Thermodynamic binding between $[B_{12}(CN)_{11}]^-$ and neon (arguably the most inert of all the elements[87]) was also observed by MS.[73] In addition, the VDE of $[B_{12}(CN)_{12}]^{2-}$ was determined to be 5.75 eV by negative-ion

photoelectronic spectroscopy (NIPES).[72] This is the largest experimental value observed for any MCA and confirms the superhalogen character of the percyanated B_{12} dianion.

1.5 This Work

Here we report the synthesis, isolation, and characterization of $[B_{12}(CN)_{12}]^{2-}$ by a novel protocol for metal-catalyzed cross-coupling under MWI. Characterization by NMR, Fourier-transform infrared spectroscopy (FTIR), and high-resolution mass spectrometry (HRMS) is reported along with two distinct single-crystal structures obtained via X-ray diffraction (XRD). The chemical stability of the cluster was evaluated, and attempts were made at acid hydrolysis of the cluster's cyano groups. Metal-catalyzed cross-coupling under MWI was also used for the cyanation of the CB_{11} and B_{10} clusters in order to produce additional heavily cyanated boron clusters and results were characterized by liquid chromatography-mass spectrometry (LC-MS) and ^{11}B NMR. Lastly, the electronic stability of the perfunctionalized B_{10} cluster with CN, SCN, and BO substituents was explored computationally and compared to their B_{12} functional analogs.

2. RESULTS AND DISCUSSION

2.1 Synthesis of $[B_{12}(CN)_{12}]^{2-}$

While cyanation via transition-metal cross-coupling reactions had previously been demonstrated with the CB_{11} and C_2B_{10} carboranes, it had yet to be explored with the isoelectronic B_{12} cluster. The periodinated cross-coupling precursor, $[B_{12}I_{12}]^{2-}$, was prepared according to published methods.[89] The percyanation of $[B_{12}I_{12}]^{2-}$ was first attempted using $Pd(OAc)_2$ and CuCN in *N,N*-dimethylformamide (DMF) under MWI. For initial reactions, heating for 30 min at 240 ˚C followed by 30 min at 260 ˚C showed no reaction by ^{11}B NMR. Analysis by electrospray-ionization mass-spectrometry (ESI-MS) revealed a mixture of partially and percyanated products after only a short period of heating at 280 ˚C (ca. 20 min).

A small-scale, systematic reaction study was carried out in an attempt to increase the ratio of per- to polycyanated products. As with the mono- and dicyanation of CB_{11}, which have been previously shown to proceed with CuCN but not KCN or NaCN,[75] copper-free cyanide sources proved unreactive with the B_{12} cluster. $[B_{12}I_{12}]^{2-}$ proved entirely unreactive with $Zn(CN)_2$ and reacted slowly with Et_4NCN (forming only mono- through tricyanated products) after 90 minutes under MWI at 280 ˚C. Solvent and atmospheric conditions showed less of an effect on the reaction than the cyanide source, with all tested solvents resulting in $[B_{12}(CN)_{12}]^{2-}$ as the major product. The use of DMF resulted in higher

yields than when using higher-boiling solvents such as dimethylacetamide (DMA) or *N*-methyl-2-pyrrolidone (NMP). Running the reaction under an inert atmosphere (Ar) decreased the percentage of desired product by more than half. All tested palladium catalysts gave $[B_{12}(CN)_{12}]^{2-}$ as the major product in a mixture of clusters with the formula $[B_{12}(CN)_nI_{12-n}]^{2-}$ ($n \geq 4$) after 90 min under MWI at 280 ˚C, except for $PdCl_2(PhCN)_2$

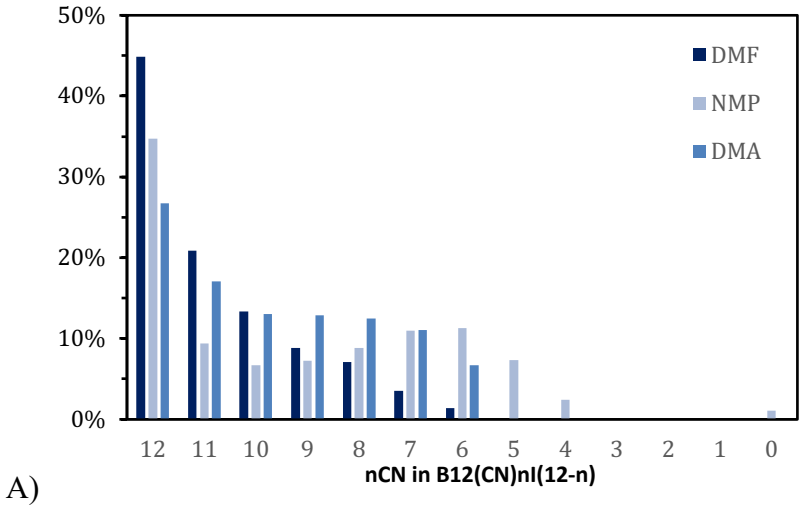

A)

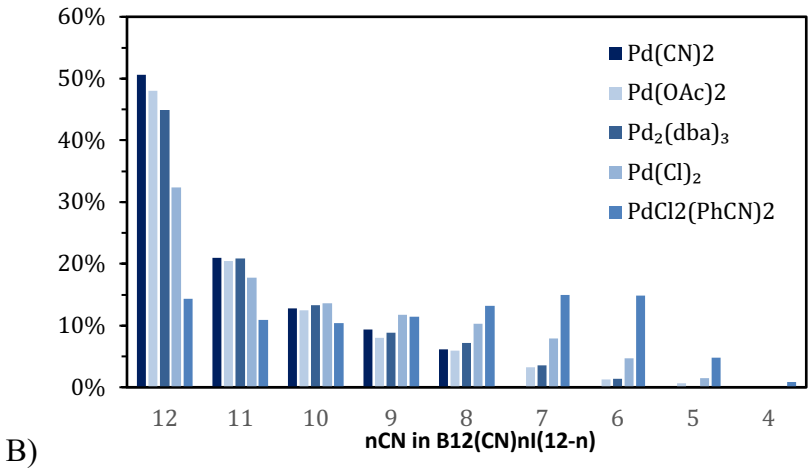

B)

Figure 11. Evaluation of conditions for the cyanation of B_{12} with varying **(A)** solvents and **(B)** palladium catalysts. All reactions were performed with 20 mg of $[Et_4N]_2[B_{12}I_{12}]$, 15 eq. CuCN, and 25 mol% palladium catalyst in DMF, and checked by ESI-MS after 90 min of MWI heating at 280 °C.

which favored the hexa- and hepta-cyanated species. While $Pd(CN)_2$ showed the best conversion on a small scale (20 mg $[Et_4N]_2[B_{12}I_{12}]$), on a larger scale (0.2 g $[Et_4N]_2[B_{12}I_{12}]$), $PdCl_2$ and $Pd_2(dba)_3$ (dba = dibenzylideneacetone) showed a more rapid and complete conversion to the percyanated product.

Testing reaction progress as a function of time showed that the ratio of per- to polycyanated products reached a maximum fairly quickly (ca. 30 minutes), and then proceeded to decrease significantly with further heating. Increased quantities of catalyst and CuCN did not substantially affect conversion to the desired product. Chromatographic separation of the percyanated product from other polycyanated species was nontrivial as these boron clusters could not be visualized using UV or common chromatographic stains (e.g. I_2 or $KMnO_4$). Therefore, the most promising route for the isolation of $[B_{12}(CN)_{12}]^{2-}$ was through overcoming the unexpected reaction reversion and forcing the reaction to completion. The exact cause of this reversion is uncertain, but the significant quantity of iodine liberated during the cyanation reaction was hypothesized to interfere with the completion of the reaction. A modified protocol which included an initial 30 min heating cycle, followed by a wash with aqueous sodium sulfite to remove accumulated iodine, and reheating for 30 minutes with fresh palladium catalyst and CuCN, was found to reliably convert the starting material to $[B_{12}(CN)_{12}]^{2-}$. The quantity of catalytic $PdCl_2$ used was ca. 50 mol% per heating cycle (resulting in a turnover number of 12). Decreasing the quantity of catalyst to ca. 25 mol% per heating cycle showed little effect on reaction progress and could likely be decreased further.

The reaction was worked up via a straightforward chromatography-free procedure to give $[Et_4N]_2[B_{12}(CN)_{12}]$ in reliable yields of 31–39%. The isolated product eluted as a

single band in the LC-MS chromatogram with *m/z* 220.9 (*z* = 2) in the negative-ion MS spectrum, consistent with $[B_{12}(CN)_{12}]^{2-}$. Characterization by ^{11}B NMR showed a resonance at −17.6 ppm for the product and the disappearance of the resonance at −15.7 ppm for the $[B_{12}I_{12}]^{2-}$ starting material. The ^{13}C NMR spectrum contained a resonance at 117 ppm for the carbon in the CN groups; significant broadening of this peak is consistent with one-bond coupling of the C_{CN} nucleus to the attached quadrupolar ^{11}B nucleus. The FTIR spectrum of $[Et_4N]_2[B_{12}(CN)_{12}]$ showed a band at 2235 cm^{-1}, consistent with a C≡N stretch and in agreement with scaled frequencies of 2255–2257 cm^{-1} for the C≡N stretching modes calculated at the B3LYP/6-311+G(d,p) level. Negative-ion HRMS showed an isotopic envelope with a maximum at *m/z* 221.0784, which is in excellent agreement with the theoretical mass for the most isotopically abundant $[B_{12}(CN)_{12}]^{2-}$ species (calculated: *m/z* 221.0777). No other boron clusters were detected by MS.

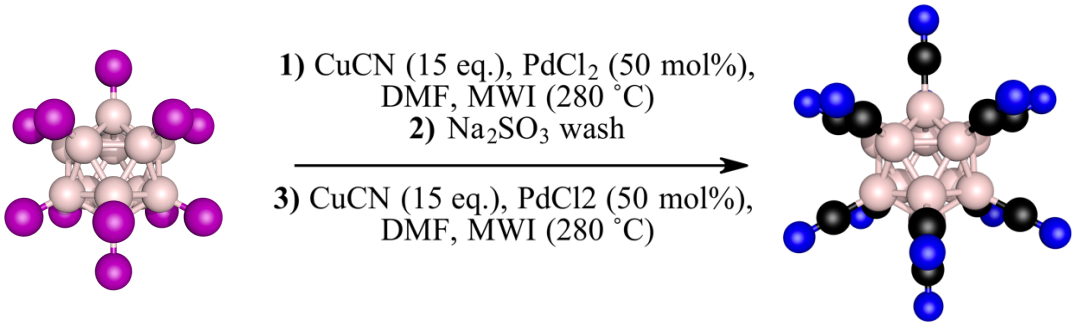

Figure 12. Conditions for the preparation of the percyanated dianion, $[B_{12}(CN)_{12}]^{2-}$, from $[B_{12}I_{12}]^{2-}$ using an intermediate iodine removal step.

2.2 $[B_{12}(CN)_{12}]^{2-}$ Crystal Structure

The single-crystal structure of the percyanated B_{12} cluster as a bridging ligand in the copper complex, $(CH_3CN)_3Cu[\mu\text{-}B_{12}(CN)_{12}]Cu(NCCH_3)_3$, was obtained by XRD. A

suitable sample for XRD was produced through an alternative workup for $[B_{12}(CN)_{12}]^{2-}$ that did not involve an extraction to remove copper, giving a white solid that was recrystallized from a mixture of acetonitrile and water. The asymmetric unit of the crystal structure contains one copper atom coordinated to the nitrogen atom in each of three acetonitrile ligands and a nitrogen from one of the cyano groups in $[B_{12}(CN)_{12}]^{2-}$ in a distorted tetrahedral geometry: N−Cu−N angles average 109.43˚ and range from a minimum of 102.51˚ for $N9_{CH3CN}$−Cu−$N1_{B12(CN)}$ to a maximum of 114.21˚ for N9−Cu−N2. The Cu−N lengths are nearly identical with a longest distance of 1.999(2) Å for Cu−N1 and a shortest distance of 1.977(3) Å for Cu−N2, thereby falling within the range of Cu−N distances (1.964−2.030 Å) observed in crystal structures of tetrakis-(acetonitrile)copper(I).[90–94] All C≡N groups in $[B_{12}(CN)_{12}]^{2-}$ are essentially linear (∠B–C≡N = 177.21−178.66˚), except for the nitrile group coordinated to the copper center,

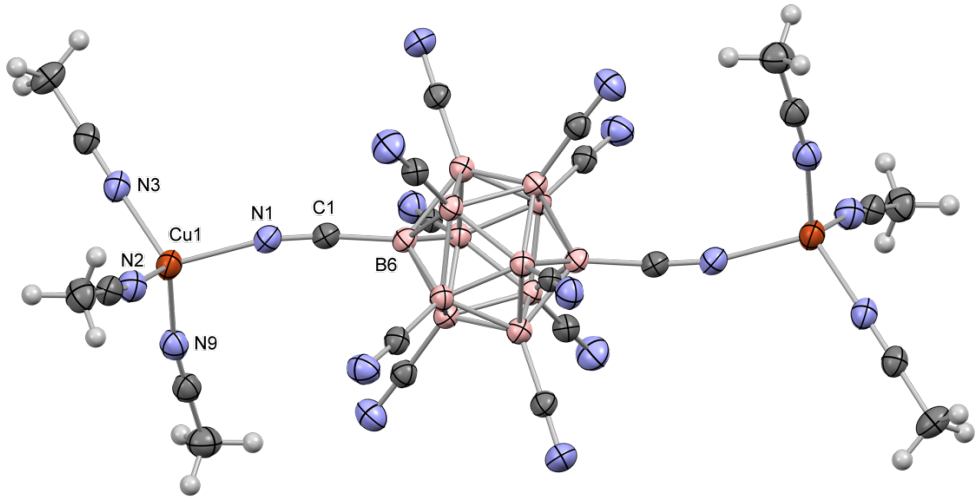

Figure 13. Single-crystal structure of $(CH_3CN)_3Cu[\mu\text{-}B_{12}(CN)_{12}]Cu(NCCH_3)_3$. Thermal ellipsoids are drawn at the 50% probability level. The asymmetric unit contains a single distorted tetrahedral copper(I) center coordinated to three acetonitrile molecules and one nitrile group from $[B_{12}(CN)_{12}]^{2-}$. Two asymmetric units, related by a center of inversion at the center of the B_{12} cluster, comprise the full complex.

which is slightly bent (∠B–C≡N = 173.84˚). The B_{12} core of the cluster is essentially icosahedral in the crystal structure with B−B bond lengths of 1.789 ± 0.012 Å, similar to B−B bond distances for other dodecaborate clusters.[95,96]

The single-crystal structure of the percyanated B_{12} cluster as bis(tetraethylammonium) salt, $[Et_4N]_2[B_{12}(CN)_{12}]$, was obtained by XRD. A suitable sample was produced via the reported workup, giving a white solid that was recrystallized from a mixture of acetonitrile and water. The asymmetric unit contains one full Et_4N cation and two cluster fragments, one comprised of two and one comprised of four boron vertexes with their corresponding nitrile groups. The crystal exhibits a rhombohedral lattice

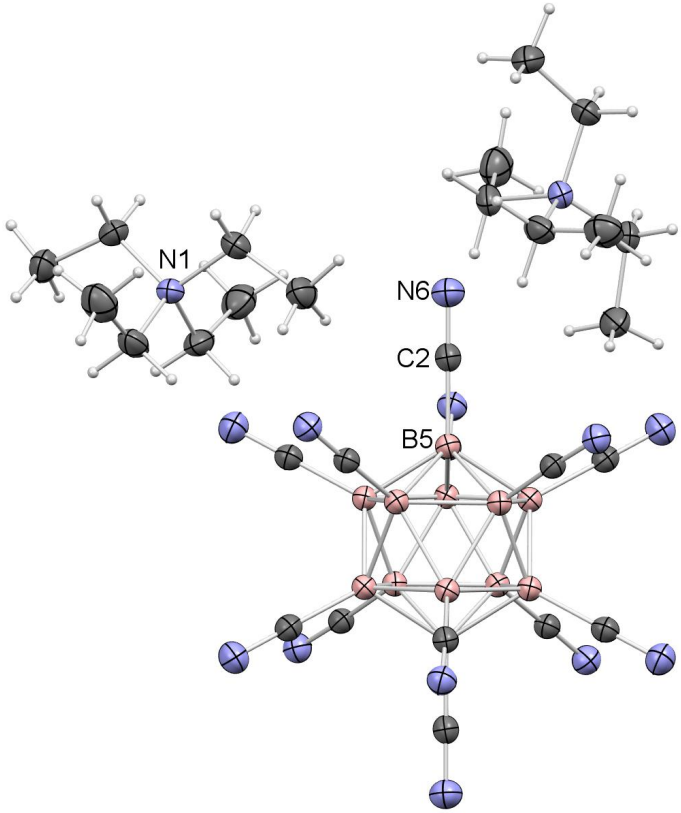

Figure 14. Single-crystal structure of $[Et_4N]_2[B_{12}(CN)_{12}]$. Thermal ellipsoids are drawn at the 50% probability level. The asymmetric unit contains one full Et_4N cation and two cluster fragments, one comprised of two and one comprised of four boron vertexes with their corresponding nitrile groups.

structure with space group P–3 and a unit cell volume of 2958.15(6) Å^3. Like in the copper complex structure, most C≡N groups in $[Et_4N]_2[B_{12}(CN)_{12}]$ are essentially linear (∠B–C≡N = 177.28−179.82˚) with the exception of two nitrile groups in the asymmetric unit that are slightly bent (∠B–C≡N = 173.34˚ and 175.29˚). The B_{12} core of the cluster is essentially icosahedral in the crystal structure with B−B bond lengths of 1.790 ± 0.008 Å, similar to B−B bond distances observed in other dodecaborate clusters and the $(CH_3CN)_3Cu[\mu\text{-}B_{12}(CN)_{12}]Cu(NCCH_3)_3$ crystal structure.[95,96]

2.3 $[B_{12}(CN)_{12}]^{2-}$ Stability and Hydrolysis

Investigation of $[B_{12}(CN)_{12}]^{2-}$ demonstrates its stability under a variety of conditions. The ^{11}B NMR spectrum of isolated $[Et_4N]_2[B_{12}(CN)_{12}]$ was unaffected by treatment with 3 M KOH in 5% aqueous CH_3CN and remained unchanged for over 24 hours at room temperature. By contrast, the periodinated precursor, $[B_{12}I_{12}]^{2-}$, completely decomposed to $B(OH)_4^-$ under the same conditions. The percyanated cluster was also stable in strong aqueous acid, showing no change by ^{11}B NMR for over 24 hours at room temperature in 50% H_2SO_4. Likewise, $[B_{12}(CN)_{12}]^{2-}$ did not react for over 24 hours when treated with excess aqueous Ce^{4+} or with sodium metal in tetrahydrofuran (THF).

The stability of $[B_{12}(CN)_{12}]^{2-}$ in acid suggested the possibility of converting its C≡N groups to carboxylic acids via acid-catalyzed hydrolysis, an approach that has previously been used to prepare carboxylic acid derivatives the CB_{11} cluster.[75,97] Acid hydrolysis of the mono- and di-cyanated CB_{11} carboranes was achieved by Rosenbaum et al.[75] and by Dwulet and Juhasz[97] respectively using a mixture of hydrochloric and acetic acids under MWI. Hydrolysis of $[B_{12}(CN)_{12}]^{2-}$ in hydrochloric acid/acetic acid solutions

were attempted under both MWI and conventional heating. ESI-MS monitoring of MWI reactions showed product mixtures containing unreacted $[B_{12}(CN)_{12}]^{2-}$ as well as clusters with one and two COOH groups (in abundances of up to ca. 40% and 20%, respectively). These reactions were performed between 120–140 ˚C as significant decomposition of the boron cage into $B(OH)_3$ occurred after only 30 min under MWI at higher temperatures (e.g. 180 ˚C). Negligible decomposition was observed for conventionally heated reactions, but these required two weeks under reflux to achieve a comparable product mixture.

2.4 Synthesis of $[CB_{11}H_6(CN)_6]^-$

No degree of cyanation greater than two has previously been reported in carborane systems. In our lab, Rosenbaum previously explored the synthesis of the heavily cyanated species, $[CB_{11}H_6(CN)_6]^-$ and $[CHB_{11}(CN)_{11}]^-$.[98] In attempts to synthesize the hexacyanated cluster from $[CB_{11}H_6I_6]^-$ using $Pd(Ph_3P)_2Cl_2$ and CuCN, extended heating at 250 ˚C under MWI gave a 3:1 mixture of $[CB_{11}H_6(CN)_6]^-$ and $[CB_{11}H_6I(CN)_5]^-$. No methods for improving the ratio of products to intermediates in solution were developed, and the hexacyanated product was not isolated and characterized. A single attempt was made at the undecacyanation of $[CHB_{11}I_{11}]^-$, under the same conditions, but no cyanated products were detected by LC-MS.

The hexaiodinated cross-coupling precursor, $[CB_{11}H_6I_6]^-$, was prepared according to published methods.[89] A small-scale, systematic reaction study was carried out in an attempt to increase the ratio of products to lesser-functionalized intermediates. No decomposition of the CB_{11} cluster was observed at 280 ˚C so all reactions were carried out at this temperature. All palladium catalysts tested gave $[CB_{11}H_6I(CN)_5]^-$ as their major

product after 90 min under MWI, except for $Pd(OAc)_2$ and $Pd_2(dba)_3$ which gave $[CB_{11}H_6(CN)_6]^-$ as a major product. As in the synthesis of the percyanated B_{12} cluster, the use of DMF resulted in higher yields than DMA or NMP. Running the reaction under an inert atmosphere (Ar) also decreased the percentage of desired product.

Extending the period of heating did not have a significant effect on the distribution of products. However, filtration to remove spent catalyst, followed by a second addition of CuCN and $Pd(OAc)_2$ and an additional 90 min of heating under MWI, was able to push the ratio of $[CB_{11}H_6(CN)_6]^-$ to $[CB_{11}H_6I(CN)_5]^-$ as high as 10:1. Subsequent rounds of heating without the further addition of reagents caused the ratio of $[CB_{11}H_6(CN)_6]^-$ to $[CB_{11}H_6I(CN)_5]^-$ to decrease significantly. This reaction reversion suggested that an intermediate iodine removal step, as used in the synthesis of $[B_{12}(CN)_{12}]^{2-}$, might aid in the synthesis and isolation of pure $[CB_{11}H_6(CN)_6]^-$. A modified protocol which included an initial 90 min heating cycle, followed by a wash with aqueous sodium sulfite to remove accumulated iodine, and reheating for 30 minutes with fresh palladium catalyst and CuCN, was not found to be effective at producing higher ratios of $[CB_{11}H_6(CN)_6]^-$ to $[CB_{11}H_6I(CN)_5]^-$ than reactions without the sodium sulfite wash. The synthesis of $[CB_{11}H_6(CN)_6]^-$ in reasonable yields is not excessively difficult, however, the isolation and characterization of a pure product will likely require more forceful reaction conditions, an alternate synthetic approach, selective crystallization, or the performance of a difficult chromatographic purification.

2.5 Attempted Synthesis of $[CHB_{11}(CN)_{11}]^-$

Although computational studies typically focus on perfunctionalized carboranes (e.g. $[CB_{11}X_{12}]^-$ where X is any functional group), from a synthetic perspective, methods for the functionalization of the CB_{11} cluster's carbon vertex often differ from those for the CB_{11} cluster's boron vertices. Because of this, undecafunctionalization (at positions 2–12) of CB_{11} is frequently pursued over perfunctionalization. Additionally, in the case of cyanation via metal-catalyzed cross-coupling, synthesis of the requisite periodinated CB_{11} precursor has not yet been reported in the literature.

The undecaiodinated cross-coupling precursor, $[CHB_{11}I_{11}]^-$, was prepared according to published methods.[89] While the hexaiodinated CB_{11} precursor is stable under the harsh reaction conditions needed for cyanation (i.e. 280 ˚C) with minimal cage decomposition, that is not the case for $[CHB_{11}I_{11}]^-$. Rosenbaum's attempt at the synthesis of $[CB_{11}(CN)_{11}]^-$ showed no cyanated products by LC-MS.[98] A more systematic approach using CuCN and $Pd_2(dba)_2$ in DMF showed a change in the ^{11}B NMR spectrum of $[CHB_{11}I_{11}]^-$ after heating at 200 ˚C for 90 minutes, with the large number of peaks representing a complex mixture of clusters containing both iodine and CN ligands. Subsequent rounds of heating showed significant decomposition of the boron cage after extended heating between 200–220 ˚C or after brief rounds of heating at higher temperatures. While it may later be shown to be possible via other synthetic routes, current protocols for palladium-catalyzed cross-coupling with boron cluster substrates appear to be inadequate for the preparation of $[CHB_{11}(CN)_{11}]^-$.

2.6 Synthesis of $[B_{10}(CN)_{10}]^{2-}$

No degree of cyanation greater than one has previously been achieved with the B_{10} cluster.[83] The B_{10} cluster is not nearly as thermally or electronically stable as the B_{12} cluster, but percyanation using the same method employed in the percyanation of the B_{12} cluster was hypothesized to be successful due to the B_{10} cluster's previously-demonstrated lower resistance to EAS reactions with certain electrophiles (e.g. halogens).[67] The periodinated cross-coupling precursor, $[B_{10}I_{10}]^{2-}$, was prepared according to published methods.[89] The percyanation of $[B_{10}I_{10}]^{2-}$ was first attempted through palladium-catalyzed cross-coupling using $Pd(OAc)_2$ and CuCN in DMF under MWI. Analysis by ESI-MS revealed a mixture of partially and percyanated products after only a short period of heating once the reaction temperature exceeded 200 ˚C.

The complete set of B_{10} cyanation data cannot be accessed during the preparation of this thesis due to campus closures amidst the 2020 COVID-19 pandemic. However, the initial results can be summarized as follows. Cyanation was attempted with multiple palladium catalysts, all of which showed some conversion of the iodinated precursor to $[B_{10}(CN)_{10}]^{2-}$. Some decomposition of the boron cage can be observed by ^{11}B NMR following heating above 220 ˚C. With optimized reaction conditions or chromatographic separation, the isolation and characterization of $[B_{10}(CN)_{10}]^{2-}$ should be possible as long as care is taken to avoid excessive decomposition of the boron cage.

2.6 $[B_{10}(CN)_{10}]^{2-}$ Stability

The computational methodology used to explore the electronic stability of $[B_{12}X_{12}]^{2-}$ (X = CN and BO) clusters can also be applied to derivatives of the B_{10} cluster.[46,48] The electron binding energies for the first and second electrons (ΔE_1 and ΔE_2 respectively) are defined by:

$$\Delta E_1 = E(Y) - E(Y^-) \quad (8)$$

$$\Delta E_2 = E(Y^-) - E(Y^{2-}) \quad (9)$$

wherein E is the ground-state single point energy of the cluster (Y) being studied. DFT geometry optimization and subsequent frequency calculations for $[B_{10}X_{10}]^m$ (X = H, F, SCN, CN, and BO; m = 0, –1, and –2) were performed in ORCA 4.0 using the PBE0 and B3LYP functionals and the def2-TZVP basis set. Optimized geometries were verified to be true minima by the absence of imaginary frequencies for vibrational frequency calculations at the same level. In some instances, the elimination of imaginary frequencies required using 'VeryTightOpt' and 'VeryTightSCF' rather than just "TightOpt' and 'TightSCF' convergence criteria. The one exception was the B3LYP optimization of $[B_{10}(SCN)_{10}]^-$ which contained a small imaginary frequency at ca. 6.5 cm^{-1}; while this frequency's magnitude suggests it is just noise, it could likely be eliminated if the calculation was performed again with 'VeryTightOpt' and 'VeryTightSCF' criteria. Missing data for X = CN and SCN in **Table 4** is a result of calculations that could not be completed due to the inability to resolve server outages during COVID-19 campus closures. Regardless, the calculated electron binding energies for X = H, F, and CN were very similar to previous calculations performed at the B3LYP level with Pople's basis sets,[57] while the values of the binding energies for X = SCN and BO are novel.

	$[B_{10}(BO)_{10}]^{2-}$	$[B_{10}(CN)_{10}]^{2-}$	$[B_{10}(SCN)_{10}]^{2-}$	$[B_{10}F_{10}]^{2-}$	$[B_{10}H_{10}]^{2-}$
ΔE_1	8.35 / 30.66	— / 7.66	— / —	4.72 / 4.68	4.52 / 4.40
ΔE_2	4.50 / 4.28	4.20 / 4.01	— / 2.41	–0.07 / –0.11	–0.50 / –0.65

Table 4. Electron binding energies in eV for the first and second electrons (ΔE_1 and ΔE_2 respectively) of the perfunctionalized B_{10} cluster at the PBE0/def2-TZVP (first) and B3LYP/def2-TZVP (second) level.

The trend in B_{12} cluster stability as a function of ligand (BO > CN > SCN > F > H) also holds for the B_{10} cluster, although all of the electron binding energies for the perfunctionalized B_{10} cluster are slightly lower than those of the B_{12} cluster. At the PBE0/def2-TZVP level, the differences between the B_{12} and B_{10} clusters' outermost electron binding energies amount to 1.4–1.5 eV for all ligands except for CN which is slightly smaller (1.2 eV). The electronic stability induced by perfunctionalization of B_{10} with CN or BO, do however make the B_{10} cluster significantly more stable than B_{12} species like $[B_{12}H_{12}]^{2-}$ and $[B_{12}F_{12}]^{2-}$ — both of which are traditionally hailed as examples of highly stable MCAs. Like $[B_{12}(CN)_{12}]^{2-}$ and $[B_{12}(BO)_{12}]^{2-}$, the $[B_{10}(CN)_{10}]^{2-}$ and $[B_{10}(BO)_{10}]^{2-}$ clusters can be classified as halogen-free superhalogens.

The calculated electron binding energies for the outermost electrons in $[B_{10}H_{10}]^{2-}$ and $[B_{10}F_{10}]^{2-}$ are negative. This was also observed by Zhong et al. in their previous computational studies on these species.[57] While it is well known that B_{10} is most stable as a dianion in the solid phase, in the gas phase (as observed in these calculations), electrostatic repulsion between the excess charges (which increase as the size of the cluster decreases) results in a lack of stability against spontaneous electron emission. In the gas phase, the stability of the B_{10} monoanion is only superseded by that of the dianion when

the cluster is functionalized with electron-withdrawing ligands (e.g. CN) that can assist in the stabilization of the cluster's excess charge.

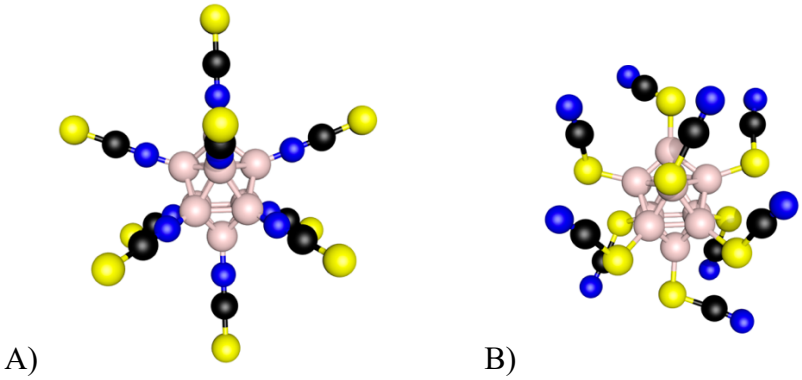

Figure 15. Structures of the B_{10} cluster with thiocyanate ligands coordinating from **(A)** the nitrogen atoms and **(B)** the sulfur atoms.

The B_{10} cluster exhibits a ground-state geometry with all polyatomic ligands in a linear configuration. The B≡O groups in $[B_{10}(BO)_{10}]^{2-}$ and C≡N groups in $[B_{10}(CN)_{10}]^{2-}$ are all essentially linear (∠B–B≡O = 179.0–180.0˚ and ∠B–C≡N = 179.2–180.0˚ at the PBE0/def2-TZVP level). As previously demonstrated in $[B_{12}(SCN)_{12}]^{2-}$,[49] coordination from the nitrogen in the thiocyanate ligand results in a lower energy structure than coordination from the sulfur (which also results in significant torsion of the ligands). The isothiocyanate groups in $[B_{10}(SCN)_{10}]^{2-}$ are also essentially linear (∠B–N=C = 178.7−180.0˚ and ∠N=C=S = 179.9−180.0˚ at the PBE0/def2-TZVP level). For all structures, the geometry of the B_{10} cluster's core is quite normal with optimized B−B bond lengths as summarized below:

	$[B_{10}(BO)_{10}]^{2-}$	$[B_{10}(CN)_{10}]^{2-}$	$[B_{10}(SCN)_{10}]^{2-}$
B_1–$B_{2–5}$	1.712	1.698	1.701
$B_{2–5}$–$B_{2–5}$	1.838	1.838	1.852
$B_{2–5}$–$B_{6–9}$	1.799	1.818	1.838

Table 5. B–B bond lengths in Å for the boron cage in perfunctionalized B_{10} clusters calculated at the PBE0/def2-TZVP level. Positions 1 and 10 are the antipodal vertices while positions 2–5 and 6–9 are the two offset four-membered rings in between.

These values are all similar to the bond lengths observed in the reported crystal structures of $[B_{10}H_{10}]^{2-}$ salts.[99,100]

3. CONCLUSION

3.1 Summary of Results

Synthesis of the heavily cyanated species $[B_{12}(CN)_{12}]^{2-}$, $[CB_{11}H_6(CN)_6]^-$, and $[B_{10}(CN)_{10}]^{2-}$ can be achieved by palladium-catalyzed cross-coupling reactions under MWI. The iodinated precursor for the synthesis of $[CHB_{11}(CN)_{11}]^-$ readily undergoes decomposition under comparable reaction conditions. The isolation of $[CB_{11}H_6(CN)_6]^-$ and $[B_{10}(CN)_{10}]^{2-}$ have not yet been achieved and will likely require reaction optimization or chromatographic purification. The isolation of $[B_{12}(CN)_{12}]^{2-}$ can be achieved as reported through an optimized synthetic procedure containing an intermediate iodine removal step. Characterization of $[B_{12}(CN)_{12}]^{2-}$ was successfully achieved by LC-MS, HRMS, FTIR, NMR, and XRD (as two distinct single-crystal structures).

The $[B_{12}(CN)_{12}]^{2-}$ cluster was shown to be stable under a variety of harsh conditions. Complete acid hydrolysis of the cyanated cluster was not observed, although a low degree of hydrolysis was observed after heating in a mixture of acetic and hydrochloric acids. Computationally, the boronyl and isothiocyanate ligands impart a degree of stability in the B_{10} cluster that is proportional to that previously demonstrated in the B_{12} cluster with the same ligands. While $[B_{10}(CN)_{10}]^{2-}$ is predicted to be the most electronically stable B_{10} species to have been synthesized, the stability of the yet-unsynthesized $[B_{10}(BO)_{10}]^{2-}$ cluster is predicted to be even greater (almost rivaling that of $[B_{12}(CN)_{12}]^{2-}$).

3.2 Future Work

Beyond the isolation and characterization of $[CB_{11}H_6(CN)_6]^-$ and $[B_{10}(CN)_{10}]^{2-}$, these heavily cyanated boron clusters can act as synthetic precursors for a number of organic transformations including but not limited to acid hydrolysis. Additional testing of the $[B_{12}(CN)_{12}]^{2-}$ and $[B_{10}(CN)_{10}]^{2-}$ can be performed to further understand their viability as electrolytes in battery systems, including cyclic voltammetry (CV). The thermal stability of these clusters should also be established by thermogravimetric analysis. Heavily iodinated derivatives of the B_{10}, C_2B_{10}, and CB_9 clusters can also be investigated as substrates for producing additional per- and polycyanated boron cluster species.

Chemistry of the boronyl ligand (B≡O), despite being isoelectronic to cyanide, is extremely limited due to the reactivity of free ligand. The development of a technique for the boronylation of boron clusters — or even of arenes — would be both an important synthetic breakthrough in-and-of-itself, and a large step towards the synthesis of ultrastable, halogen-free, boron cluster-based superhalogens for use in battery electrolyte systems. The perboronylated B_{12} cluster could also serve as a precursor for the $[B_{12}(BO)_{11}]^-$ fragment which could be sufficiently electrophilic to form stable compounds with extremely inert noble gasses such as neon and helium at or near room temperature.

4. EXPERIMENTAL

4.1 Experimental Procedures

General Methods: All reactions were performed in sealed vials using a Biotage Initiator+ microwave irradiation reactor unless noted otherwise. ^{1}H, ^{11}B, and ^{13}C NMR spectra were collected at room temperature using a Bruker Avance III 400 MHz spectrometer operating at 128.37 MHz (^{11}B), 400.13 MHz (^{1}H), and 100.62 MHz (^{13}C). All NMR samples were dissolved in acetone or acetone-d_6 unless otherwise noted and referenced to TMS (^{1}H and ^{13}C) or BF_3•OEt_2 (^{11}B). FTIR spectra were collected using a Thermo Scientific Nicolet iS5 FT-IR spectrometer with an AR-coated diamond crystal. Air-free manipulation of reactions and materials was not employed unless noted otherwise.

Chemicals: $[Et_4N]_2[B_{12}I_{12}]$ was prepared from $Cs_2[B_{12}H_{12}]$ (Strem Chemical) according to published methods.[89] $Cs[CB_{11}H_{12}]$ was prepared from $B_{10}H_{14}$ (UChem Shanghai) according to published methods.[101,102] $[Et_4N][CHB_{11}I_{11}]$, $[Et_4N][CB_{11}H_6I_6]$, and $Cs[CB_{11}H_6I_6]$ were prepared from $Cs[CB_{11}H_{12}]$ according to published methods.[89] $[Et_4N]_2[B_{10}I_{10}]$ was prepared from $[Et_3NN]_2[B_{10}H_{10}]$ according to published methods.[89] $[Et_3NH]_2[B_{10}H_{10}]$ was prepared from $B_{10}H_{14}$ (UChem Shanghai) according to published methods.[103] All other reagents and solvents were purchased from commercial sources.

LC-MS: An Agilent 1220 Infinity LC and 6120 Quadrupole Mass Selective Detector was run in reverse phase mode on a 12.5 cm × 4.6 mm Supelco Discovery C8 column with 5 μm packing, a flow rate of 1 mL/min, and an injection volume of 1 μL. Compounds were

eluted using a binary solvent system of 0.1% acetic acid in H_2O (A) and 0.1% acetic acid in CH_3CN (B). The initial 80:20 (A:B) solvent ratio was changed to 0:100 (A:B) over 35 minutes and held at that ratio for 10 minutes for a total runtime of 45 minutes. Mass spectra were collected by ESI-MS on an Agilent 6120 Quadrupole MS in negative ion mode with an *m/z* range of 70-2000.

HRMS: High-resolution mass spectra were collected at the University of Washington Chemistry Mass Spectrometry Facilities. Samples were prepared by collecting a small amount of sample with a glass capillary and dissolving this in 500 μL of CH_3CN/CH_3OH along with NH_4^+ acetate or bicarbonate. MS were obtained by flow injection analysis of 0.5-1.0 μL injected into 10 μL flow of H_2O/CH_3CN (0.1% formic acid) on an LTQ-Orbitrap XL spectrometer (resolution = 60,000 FWHM).

4.2 Synthetic Procedures

Synthesis of $[Et_4N]_2[B_{12}(CN)_{12}]$, (AAK-101): A 5 mL microwave vial was loaded with $[Et_4N]_2[B_{12}I_{12}]$ (202.6 mg, 105.9 μmol), CuCN (151.9 mg, 1.696 mmol), $PdCl_2$ (10.4 mg, 58.7 μmol), and DMF (2.5 mL). The vial was sealed and heated at 280 ˚C for 30 minutes via MWI. The solution was evaporated to dryness under vacuum and the green-black residue was washed with an aqueous solution of sodium sulfite (1M, 20 mL). The resulting mixture was gravity filtered and washed with a minimal amount of H_2O. The filter paper was rinsed through with acetone into a separate flask and the brown filtrate was evaporated to a dry brown solid under vacuum. The brown solid was taken into DMF (2.5 mL) and

quantitatively transferred to a 5 mL microwave vial. Copper(I) cyanide (144.0 mg, 1.608 mmol) and $PdCl_2$ (8.5 mg, 48 μmol) were added, the vial was sealed, and the solution was heated to 280 ˚C for 12 minutes via MWI. Aqueous NH_4Cl (25%, 10 mL) was added to the reaction and the product was extracted into ether (3 × 10 mL). The ether layer was washed with aqueous NH_4Cl (25%, 15 mL) and NaCl (saturated, 15 mL). The light, translucent brown ether layer was gravity filtered, washing the separatory funnel and filter paper through with acetone. The solution was evaporated to dryness resulting in thin brown crystals. A solution of Et_4NBr (0.45 g, 2.1 mmol) in H_2O (10 mL) was added to the crystals and the resulting solid was collected via vacuum filtration. The solid was washed with minimal cold H_2O and dried under vacuum to give $[Et_4N]_2[B_{12}(CN)_{12}]$ (26.1 mg, 37.2 μmol, 35% yield). ^{11}B NMR (acetone-d_6, ppm) δ = –17.6 (s); ^{1}H NMR (acetone-d_6, ppm) δ = 1.46 (tt, 12H, $N(CH_2C\mathbf{H_3})_4$), 3.56 (q, 8H, $N(C\mathbf{H_2}CH_3)_4$); ^{13}C NMR (acetone-d_6, ppm) δ = 117.6 (br, $(\mathbf{C}N)_{12}$), 52.6 ($N(\mathbf{C}H_2CH_3)_4$), 7.2 ($N(CH_2\mathbf{C}H_3)_4$). LC-MS *m/z* = 220.9. HRMS (for the most abundant mass within each isotopic envelope) *m/z* = 221.0784 ($[B_{12}(CN)_{12}]^{2-}$, theoretical = 221.0777), 572.3154 ($[Et_4N][B_{12}(CN)_{12}]^-$, theoretical = 572.3160), 443.1622 ($H[B_{12}(CN)_{12}]^-$, theoretical = 443.1638).

Alternative Workup Yielding $(CH_3CN)_3Cu[\mu\text{-}B_{12}(CN)_{12}]Cu(CH_3CN)_3$), (AAK-068): After the second round of heating, the solution was evaporated to dryness under vacuum and the resulting dark residue was taken into acetone (ca. 20 mL). The solution was filtered over a plug of Celite and H_2O (8 mL) was added to the filtrate. The acetone was removed under vacuum and the resulting mixture became cloudy. An aqueous solution (5 mL) containing Et_4NBr (0.33 g, 1.6 mmol) was added and a fine off-white precipitate formed.

The solution was cooled, and the precipitate was collected via vacuum filtration. The solid was washed with minimal cold H_2O and dried under vacuum (ca. 39% yield). Small, branching crystals were grown via slow evaporation of a saturated solution of the product dissolved in an H_2O/CH_3CN mixture (ca. 10:1). These crystals were collected via gravity filtration for characterization by XRD.

Attempted Synthesis of $[Et_4N]_2[B_{12}(COOH)_{12}]$, (AAK-087): $[Et_4N]_2[B_{10}(CN)_{12}]$ (ca. 15 mg) was heated by reflux in a mixture of conc. HCl (3 mL) and glacial acetic acid (1 mL). The reaction was monitored by ^{11}B NMR and LC-MS over the course of ca. 10 days. After 2 days, a product mixture containing ca. 2:1 ratio of $[B_{10}(CN)_{11}(COOH)]^{2-}$ (*m/z* = 230.5) to $[B_{10}(CN)_{12}]^{2-}$ (*m/z* = 221.0) was observed by LC-MS (along with a third peak corresponding to a mixture of $[B_{10}(CN)_{10}(COOH)_2]^{2-}$ at *m/z* = 240.0 and an unidentified compound at *m/z* = 456). No decomposition was detected by ^{11}B NMR.

Attempted MWI Synthesis of $[Et_4N]_2[B_{12}(COOH)_{12}]$, (AAK-090): In a 2.5 mL microwave vial, $[Et_4N]_2[B_{10}(CN)_{12}]$ (ca. 15 mg) was heated to between 120–140 ˚C in a mixture of H_2O (0.4 mL), conc. HCl (0.8 mL) and glacial acetic acid (0.4 mL). The reaction was monitored by ^{11}B NMR and LC-MS over the course of ca. 18 hr. After 6 hr, a product mixture containing ca. 1:2:2 ratio of $[B_{10}(CN)_{10}(COOH)_2]^{2-}$ (*m/z* = 240.0) to $[B_{10}(CN)_{11}(COOH)]^{2-}$ (*m/z* = 230.5) to $[B_{10}(CN)_{12}]^{2-}$ *m/z* = 221.0) was observed by LC-MS and no decomposition was detected by ^{11}B NMR.

Synthesis of $[Et_4N][CB_{11}H_6(CN)_6]$, (see AAK-030, -074, & -102): In a 2.5 mL microwave vial, $Cs[CB_{11}H_6I_6]$ (ca. 20 mg), CuCN (ca. 8 eq.), and $Pd(OAc)_2$ (ca. 25 mol%) were combined in DMF (1.0 mL). The solution was heated for 90 min at 280 ˚C under MWI. The solution was filtered through a 0.45 μm syringe filter, CuCN (ca. 4 eq) and $Pd(OAc)_2$ (ca. 45 mol%) were added, and it heated for an additional 30 min at 280 ˚C by MWI. After heating, a 10:1 mixture of $[CB_{11}H_6(CN)_6]^-$ (*m/z* = 293.1) to $[CB_{11}H_6I(CN)_5]^-$ (*m/z* = 394.0) was identified by LC-MS.

Attempted Synthesis of $[Et_4N][CHB_{11}(CN)_{11}]$, (see AAK-009, -010, & -029): In a 2.5 mL microwave vial, $[Et_4N]_2[B_{10}H_{10}]$ (ca. 20 mg), CuCN (ca. 16 eq.), and a Pd(II) catalyst (ca. 15 mol%), were combined in DMF (1.0 mL). The solution was heated via MWI (200–240 ˚C) and cage decomposition was monitored by ^{11}B NMR. No product was identified.

Synthesis of $[Et_4N]_2[B_{10}(CN)_{10}]$, (see AAK-063 through -066): In a 2.5 mL microwave vial, $[Et_4N]_2[B_{10}H_{10}]$ (ca. 20 mg), CuCN (ca. 15 eq.), and a Pd(II) catalyst (25–50 mol%), were combined in DMF (1.0 mL). The solution was heated via MWI and reaction progress was monitored by LC-MS while decomposition was monitored by ^{11}B NMR. After heating for 10 min each at 180 ˚C and increasing the temperature by 20 ˚C intervals (up to 260 ˚C), $[B_{10}(CN)_{10}]^{2-}$ (*m/*z = 184.2) was identified as the major product.

4.3 X-Ray Diffraction Details

XRD of $[Et_4N]_2[B_{12}(CN)_{12}]$, (AAK-101e): Single crystals of $[Et_4N]_2[B_{12}(CN)_{12}]$ were grown by slow evaporation of a saturated solution of the compound (prepared as described above (**Section 4.2**) and dissolved in a ca. 5:1 mixture of H_2O and CH_3CN). A suitable crystal was selected from the solution and fractured to give an appropriately sized fragment. The crystal was mounted on a 0.2 mm diameter polyethylene loop (Hampton Research, Aliso Viejo, CA) using NVH oil and transferred to a Xcalibur, Onyx, Nova diffractometer, where the crystal was kept at 100.3(4) K under a stream of cooled nitrogen gas. The crystal structure was solved using Olex2[104] software with the ShelXS[105] structure solution program using Direct Methods and was refined with the ShelXL[106] refinement package using Least Squares minimization.

XRD of $(CH_3CN)_3Cu[\mu\text{-}B_{12}(CN)_{12}]Cu(CH_3CN)_3$, (AAK-068i): Single crystals of $(CH_3CN)_3Cu[\mu\text{-}B_{12}(CN)_{12}]Cu(CH_3CN)_3$ were prepared via the alternative workup described above. A suitable crystal was selected from the solution and fractured to give an appropriately sized fragment. The crystal was mounted on a 0.1 mm diameter polyethylene loop (Hampton Research, Aliso Viejo, CA) using NVH oil and transferred to a Xcalibur, Onyx, Nova diffractometer, where the crystal was kept at 100.3(4) K under a stream of cooled nitrogen gas. The structure was solved using Olex2 software with the olex2.solve[107] structure solution program using Charge Flipping and was refined with the olex2.refine[107] refinement package using Gauss-Newton minimization.

4.4 Computational Details

Optimization of $[B_{12}H_{12}]^{2-}$: The optimized geometry for $[B_{12}H_{12}]^{2-}$ was calculated at the B3LYP[108–111]/def2-TZVP[112] level using ORCA 4.0.[113,114] The optimized geometry was verified to be a true minimum by the absence of imaginary frequencies for a vibrational frequency calculation at the same level. Molecular orbitals were visualized using Chemcraft[115] (quantum chemistry graphical program).

Optimization of $[B_{12}(CN)_{12}]^{2-}$: The optimized geometry for $[B_{12}(CN)_{12}]^{2-}$ was calculated at the B3LYP/6-311+G(d,p)[116] level of theory using Gaussian03.[117] The optimized geometry was verified to be a true minimum by the absence of imaginary frequencies for a vibrational frequency calculation at the same level. Vibrational frequencies were scaled by a factor of 0.9679 as recommended by Andersson and Uvdal.[118]

Electron Binding in $[B_{10}X_{10}]^{m}$: The optimized geometry and vibrational frequency calculations (for electron binding energy determination) were performed for $[B_{10}X_{10}]^{m}$ (X = H, F, CN, and BO; m = 0, –1, and –2) using the B3LYP and PBE0[119] density functionals with the def2-TZVP basis set. Binding energy calculations were performed with 'TightOpt' and 'TightSCF' convergence criteria using ORCA 4.0 and verified to be true minima by the absence of imaginary frequencies for vibrational frequency calculations at the same level. When a true structural minimum could not be achieved, calculations were performed

again with stricter convergence criteria ('VeryTightOpt' and 'VeryTightSCF') and imaginary frequencies were successfully eliminated. The single exception was for $[B_{10}(SCN)_{10}]^-$ at the B3LYP level, which did not have an opportunity to be rerun using the 'VeryTight' criteria to eliminate imaginary frequencies.

5. ACKNOWLEDGMENTS

Funding for this work was provided through grants from the National Science Foundation (CHE-1764344) and the Murdock College Research Program for the Natural Sciences.

I would like to thank the faculty in both the Department of Chemistry and Department of Music for their unwavering support and mentorship during my time at Whitman College. I would especially like to thank: Prof. Mark Juhasz for giving me the opportunity to conduct research in his lab and for teaching me about everything from instrumentation to writing scientific papers; Prof. Mark Hendricks for crucial insights and support throughout applying to graduate school; and Dr. Sally Singer Tuttle for supporting my creative growth and experimental projects even after I decided not to major in cello performance. Lastly, I would like to thank my parents for making my education here possible.

6. REFERENCES

(1) Dalal, M. *A Textbook of Inorganic Chemistry – Volume 1*; Dalal Institute, 2017.

(2) Eberhardt, W. H.; Jr, B. C.; Lipscomb, W. N. The Valence Structure of the Boron Hydrides. *J. Chem. Phys.* **1954**, *22* (6), 989–1001. https://doi.org/10.1063/1.1740320.

(3) Li, W.-K.; Zhou, G.-D.; Mak, T. C. W.; Mak, T. *Advanced Structural Inorganic Chemistry*; OUP Oxford, 2008.

(4) Longuet-Higgins, H. C.; Roberts, M. D. V.; Emeleus, H. J. The Electronic Structure of an Icosahedron of Boron Atoms. *Proc. R. Soc. Lond. Ser. Math. Phys. Sci.* **1955**, *230* (1180), 110–119. https://doi.org/10.1098/rspa.1955.0115.

(5) Pitochelli, A. R.; Hawthorne, F. M. THE ISOLATION OF THE ICOSAHEDRAL B12H12-2 ION. *J. Am. Chem. Soc.* **1960**, *82* (12), 3228–3229. https://doi.org/10.1021/ja01497a069.

(6) Wade, K. The Structural Significance of the Number of Skeletal Bonding Electron-Pairs in Carboranes, the Higher Boranes and Borane Anions, and Various Transition-Metal Carbonyl Cluster Compounds. *J. Chem. Soc. Chem. Commun.* **1971**, No. 15, 792–793. https://doi.org/10.1039/C29710000792.

(7) King, R. B. Three-Dimensional Aromaticity in Polyhedral Boranes and Related Molecules. *Chem. Rev.* **2001**, *101* (5), 1119–1152. https://doi.org/10.1021/cr000442t.

(8) Chen, Z.; King, R. B. Spherical Aromaticity: Recent Work on Fullerenes, Polyhedral Boranes, and Related Structures. *Chem. Rev.* **2005**, *105* (10), 3613–3642. https://doi.org/10.1021/cr0300892.

(9) Hirsch, A.; Chen, Z.; Jiao, H. Spherical Aromaticity of Inorganic Cage Molecules. *Angew. Chem. Int. Ed.* **2001**, *40* (15), 2834–2838. https://doi.org/10.1002/1521-3773(20010803)40:15<2834::AID-ANIE2834>3.0.CO;2-H.

(10) Igor B. Sivaev; Vladimir I. Bregadze. Polyhedral Boron Hydrides in Use: Current Status and Perspectives. In *Organometallic Chemistry Research Perspectives*; Nova Publishers, 2007.

(11) Clark, J. D.; Asimov, I. *Ignition!: An Informal History of Liquid Rocket Propellants*; Rutgers University Press: New Brunswick, United States, 2018.

(12) Soloway, A. H.; Tjarks, W.; Barnum, B. A.; Rong, F.-G.; Barth, R. F.; Codogni, I. M.; Wilson, J. G. The Chemistry of Neutron Capture Therapy. *Chem. Rev.* **1998**, *98* (4), 1515–1562. https://doi.org/10.1021/cr941195u.

(13) Nedunchezhian, K. Boron Neutron Capture Therapy - A Literature Review. *J. Clin. Diagn. Res.* **2016**. https://doi.org/10.7860/JCDR/2016/19890.9024.

(14) Cerecetto, H.; Couto, M. Medicinal Chemistry of Boron-Bearing Compounds for BNCT- Glioma Treatment: Current Challenges and Perspectives. *Glioma* -

Contemp. Diagn. Ther. Approaches **2018**. https://doi.org/10.5772/intechopen.76369.

(15) Moss, R. L. Critical Review, with an Optimistic Outlook, on Boron Neutron Capture Therapy (BNCT). *Appl. Radiat. Isot.* **2014**, *88*, 2–11. https://doi.org/10.1016/j.apradiso.2013.11.109.

(16) Mochizuki, M.; Sato, S.; Asatyas, S.; Leśnikowski, Z. J.; Hayashi, T.; Nakamura, H. Raman Cell Imaging with Boron Cluster Molecules Conjugated with Biomolecules. *RSC Adv.* **2019**, *9* (41), 23973–23978. https://doi.org/10.1039/C9RA04228H.

(17) Leśnikowski, Z. J. New Opportunities for Boron in Chemistry for Medical Applications. In *Boron Science: New Technologies and Applications*; Hosmane, N. S., Ed.; CRC Press: Boca Raton. FL, 2011.

(18) Endo, Y. Carboranes as Hydrophobic Pharmacophores. In *Boron-Based Compounds*; Evamarie Hey-Hawkins, Clara Viñas Teixidor, Eds.; John Wiley & Sons, Ltd, 2018; pp 1–19. https://doi.org/10.1002/9781119275602.ch1.1.

(19) Jiménez, C. C.; Enríquez-Cabrera, A.; González-Antonio, O.; Ordóñez-Hernández, J.; Lacroix, P. G.; Labra-Vázquez, P.; Farfán, N.; Santillan, R. State of the Art of Boron and Tin Complexes in Second- and Third-Order Nonlinear Optics §. *Inorganics* **2018**, *6* (4), 131. https://doi.org/10.3390/inorganics6040131.

(20) Andrea Vöge; Detlef Gabel. Boron Derivatives for Applications in Nonlinear Optics. In *Boron Science: New Technologies and Applications*; Hosmane, N. S., Ed.; CRC Press: imprint of the Taylor & Francis Group: Boca Raton. FL, 2012.

(21) Strauss, S. H. The Search for Larger and More Weakly Coordinating Anions. *Chem. Rev.* **1993**, *93* (3), 927–942.

(22) Reed, C. A.; Kim, K.-C.; Bolskar, R. D.; Mueller, L. J. Taming Superacids: Stabilization of the Fullerene Cations HC60+ and C60·+. *Science* **2000**, *289* (5476), 101–104. https://doi.org/10.1126/science.289.5476.101.

(23) Kato, T.; Reed, C. A. Putting Tert-Butyl Cation in a Bottle. *Angew. Chem. Int. Ed.* **2004**, *43* (22), 2908–2911. https://doi.org/10.1002/anie.200453931.

(24) Kim, K.-C.; Reed, C. A.; Elliott, D. W.; Mueller, L. J.; Tham, F.; Lin, L.; Lambert, J. B. Crystallographic Evidence for a Free Silylium Ion. *Science* **2002**, *297* (5582), 825–827. https://doi.org/10.1126/science.1073540.

(25) Reed, C. A. Isolating Benzenium Ion Salts. *J Am Chem Soc* **2003**, *125*, 1796–1804.

(26) Ivanov, S. V.; Miller, S. M.; Anderson, O. P.; Solntsev, K. A.; Strauss, S. H. Synthesis and Stability of Reactive Salts of Dodecafluoro-Closo-Dodecaborate(2−). *J. Am. Chem. Soc.* **2003**, *125* (16), 4694–4695. https://doi.org/10.1021/ja0296374.

(27) Juhasz, M.; Hoffmann, S.; Stoyanov, E.; Kim, K. C.; Reed, C. A. The Strongest Isolable Acid. *Angew. Chem.-Int. Ed.* **2004**, *43* (40), 5352–5355. https://doi.org/10.1002/anie.200460005.

(28) Nieuwenhuyzen, M.; Seddon, K. R.; Teixidor, F.; Puga, A. V.; Viñas, C. Ionic Liquids Containing Boron Cluster Anions. *Inorg. Chem.* **2009**, *48* (3), 889–901. https://doi.org/10.1021/ic801448w.

(29) Zhu, Y.; Hosmane, N. S. Ionic Liquids: Recent Advances and Applications in Boron Chemistry. *Eur. J. Inorg. Chem.* **2017**, *2017* (38–39), 4369–4377. https://doi.org/10.1002/ejic.201700553.

(30) Ringstrand, B. Boron Clusters as Structural Elements of Novel Liquid Crystalline Materials. *Liq. Cryst. Today* **2013**, *22* (2), 22–35. https://doi.org/10.1080/1358314X.2013.829932.

(31) Kaniowski, D.; Ebenryter-Olbinska, K.; Kulik, K.; Janczak, S.; Maciaszek, A.; Bednarska-Szczepaniak, K.; Nawrot, B.; Lesnikowski, Z. Boron Clusters as a Platform for New Materials: Composites of Nucleic Acids and Oligofunctionalized Carboranes (C2B10H12) and Their Assembly into Functional Nanoparticles. *Nanoscale* **2019**, *12* (1), 103–114. https://doi.org/10.1039/C9NR06550D.

(32) Sebastian Bauer; Evamarie Hey-Hawkins. Phosphorus-Substituted Carboranes in Catalysis. In *Boron Science: New Technologies and Applications*; Hosmane, N. S., Ed.; CRC Press: imprint of the Taylor & Francis Group: Boca Raton. FL, 2012.

(33) Larm, N. E.; Madugula, D.; Lee, M. W.; Baker, G. A. Polyhedral Borane-Capped Coinage Metal Nanoparticles as High-Performing Catalysts for 4-Nitrophenol Reduction. *Chem. Commun.* **2019**, *55* (55), 7990–7993. https://doi.org/10.1039/C9CC03428E.

(34) Qi, B.; Wu, C.; Li, X.; Wang, D.; Sun, L.; Chen, B.; Liu, W.; Zhang, H.; Zhou, X. Self-Assembled Magnetic Gold Catalysts from Dual-Functional Boron Clusters. *ChemCatChem* **2018**, *10* (10), 2285–2290. https://doi.org/10.1002/cctc.201702011.

(35) Dash, B. P.; Satapathy, R.; Maguire, J. A.; Hosmane, N. S. Polyhedral Boron Clusters in Materials Science. *New J. Chem.* **2011**, *35* (10), 1955–1972. https://doi.org/10.1039/C1NJ20228F.

(36) Núñez, R.; Romero, I.; Teixidor, F.; Viñas, C. Icosahedral Boron Clusters: A Perfect Tool for the Enhancement of Polymer Features. *Chem. Soc. Rev.* **2016**, *45* (19), 5147–5173. https://doi.org/10.1039/C6CS00159A.

(37) Housecroft, C. E. Carboranes as Guests, Counterions and Linkers in Coordination Polymers and Networks. *J. Organomet. Chem.* **2015**, *798*, 218–228. https://doi.org/10.1016/j.jorganchem.2015.04.047.

(38) Spokoyny, A. M.; Farha, O. K.; Mulfort, K. L.; Hupp, J. T.; Mirkin, C. A. Porosity Tuning of Carborane-Based Metal–Organic Frameworks (MOFs) via Coordination Chemistry and Ligand Design. *Inorganica Chim. Acta* **2010**, *364* (1), 266–271. https://doi.org/10.1016/j.ica.2010.08.007.

(39) Grimes, R. N. Boron Clusters Come of Age. *J. Chem. Educ.* **2004**, *81* (5), 657. https://doi.org/10.1021/ed081p657.

(40) Nishi, Y. Chapter 2 – Past, Present and Future of Lithium-Ion Batteries: Can New Technologies Open up New Horizons? In *Lithium-Ion Batteries: Advances and Applications*; Newnes, 2013.

(41) Liu, C.; Neale, Z. G.; Cao, G. Understanding Electrochemical Potentials of Cathode Materials in Rechargeable Batteries. *Mater. Today* **2016**, *19* (2), 109–123. https://doi.org/10.1016/j.mattod.2015.10.009.

(42) Wang, Q.; Ping, P.; Zhao, X.; Chu, G.; Sun, J.; Chen, C. Thermal Runaway Caused Fire and Explosion of Lithium Ion Battery. *J. Power Sources* **2012**, *208*, 210–224. https://doi.org/10.1016/j.jpowsour.2012.02.038.

(43) Hammami, A.; Raymond, N.; Armand, M. Runaway Risk of Forming Toxic Compounds. *Nature* **2003**, *424* (6949), 635. https://doi.org/10.1038/424635b.

(44) Larsson, F.; Andersson, P.; Blomqvist, P.; Mellander, B.-E. Toxic Fluoride Gas Emissions from Lithium-Ion Battery Fires. *Sci. Rep.* **2017**, *7*. https://doi.org/10.1038/s41598-017-09784-z.

(45) Giri, S.; Behera, S.; Jena, P. Superhalogens as Building Blocks of Halogen-Free Electrolytes in Lithium-Ion Batteries. *Angew. Chem. Int. Ed.* **2014**, *53* (50), 13916–13919. https://doi.org/10.1002/anie.201408648.

(46) Zhao, H.; Zhou, J.; Jena, P. Stability of B12(CN)122−: Implications for Lithium and Magnesium Ion Batteries. *Angew. Chem. Int. Ed.* **2016**, *55* (11), 3704–3708. https://doi.org/10.1002/anie.201600275.

(47) Singh-Miller, N. E.; Scherlis, D. A.; Marzari, N. Effect of Counterions on the Interactions of Charged Oligothiophenes. *J. Phys. Chem. B* **2006**, *110* (49), 24822–24826. https://doi.org/10.1021/jp063478j.

(48) Moon, J.; Baek, H.; Kim, J. Unusually High Stability of B 12 (BO) 12 2− Achieved by Boronyl Ligand Manipulation: Theoretical Investigation. *Chem. Phys. Lett.* **2018**, *698*, 72–76. https://doi.org/10.1016/j.cplett.2018.03.015.

(49) Fang, H.; Jena, P. B12(SCN)12–: An Ultrastable Weakly Coordinating Dianion. *J. Phys. Chem. C* **2017**, *121* (14), 7697–7702. https://doi.org/10.1021/acs.jpcc.7b00669.

(50) Marcinek, M.; Syzdek, J.; Marczewski, M.; Piszcz, M.; Niedzicki, L.; Kalita, M.; Plewa-Marczewska, A.; Bitner, A.; Wieczorek, P.; Trzeciak, T.; Kasprzyk, M.; P.Łężak; Zukowska, Z.; Zalewska, A.; Wieczorek, W. Electrolytes for Li-Ion Transport – Review. *Solid State Ion.* **2015**, *276*, 107–126. https://doi.org/10.1016/j.ssi.2015.02.006.

(51) Lide, D. R. *CRC Handbook of Chemistry and Physics, 90th Edition*; Taylor & Francis, 2009.

(52) Roedern, E.; Kühnel, R.-S.; Remhof, A.; Battaglia, C. Magnesium Ethylenediamine Borohydride as Solid-State Electrolyte for Magnesium Batteries. *Sci. Rep.* **2017**, *7* (1), 1–6. https://doi.org/10.1038/srep46189.

(53) Zhao-Karger, Z.; Fichtner, M. Beyond Intercalation Chemistry for Rechargeable Mg Batteries: A Short Review and Perspective. *Front. Chem.* **2019**, *6*. https://doi.org/10.3389/fchem.2018.00656.

(54) Song, J.; Sahadeo, E.; Noked, M.; Lee, S. B. Mapping the Challenges of Magnesium Battery. *J. Phys. Chem. Lett.* **2016**, *7* (9), 1736–1749. https://doi.org/10.1021/acs.jpclett.6b00384.

(55) Aurbach, D.; Moshkovich, M.; Schechter, A.; Turgeman, R. Magnesium Deposition and Dissolution Processes in Ethereal Grignard Salt Solutions Using Simultaneous EQCM-EIS and In Situ FTIR Spectroscopy. *Electrochem. Solid State Lett.* **1999**, *3* (1), 31. https://doi.org/10.1149/1.1390949.

(56) Tutusaus, O.; Mohtadi, R.; Arthur, T. S.; Mizuno, F.; Nelson, E. G.; Sevryugina, Y. V. An Efficient Halogen-Free Electrolyte for Use in Rechargeable Magnesium Batteries. *Angew. Chem. Int. Ed.* **2015**, *54* (27), 7900–7904. https://doi.org/10.1002/anie.201412202.

(57) Zhong, M.; Zhou, J.; Fang, H.; Jena, P. Role of Ligands in the Stability of BnXn and CBn−1Xn (n = 5–10; X = H, F, CN) and Their Potential as Building Blocks of Electrolytes in Lithium Ion Batteries. *Phys. Chem. Chem. Phys.* **2017**, *19* (27), 17937–17943. https://doi.org/10.1039/C7CP02642K.

(58) Zhao, Q.; Stalin, S.; Zhao, C.-Z.; Archer, L. A. Designing Solid-State Electrolytes for Safe, Energy-Dense Batteries. *Nat. Rev. Mater.* **2020**, *5* (3), 229–252. https://doi.org/10.1038/s41578-019-0165-5.

(59) Tang, W. S.; Unemoto, A.; Zhou, W.; Stavila, V.; Matsuo, M.; Wu, H.; Orimo, S.; Udovic, T. J. Unparalleled Lithium and Sodium Superionic Conduction in Solid Electrolytes with Large Monovalent Cage-like Anions. *Energy Environ. Sci.* **2015**, *8* (12), 3637–3645. https://doi.org/10.1039/C5EE02941D.

(60) Kim, S.; Oguchi, H.; Toyama, N.; Sato, T.; Takagi, S.; Otomo, T.; Arunkumar, D.; Kuwata, N.; Kawamura, J.; Orimo, S. A Complex Hydride Lithium Superionic Conductor for High-Energy-Density All-Solid-State Lithium Metal Batteries. *Nat. Commun.* **2019**, *10* (1), 1–9. https://doi.org/10.1038/s41467-019-09061-9.

(61) Duchêne, L.; Kühnel, R.-S.; Rentsch, D.; Remhof, A.; Hagemann, H.; Battaglia, C. A Highly Stable Sodium Solid-State Electrolyte Based on a Dodeca/Deca-Borate Equimolar Mixture. *Chem. Commun.* **2017**, *53* (30), 4195–4198. https://doi.org/10.1039/C7CC00794A.

(62) Udovic, T. J.; Matsuo, M.; Unemoto, A.; Verdal, N.; Stavila, V.; Skripov, A. V.; Rush, J. J.; Takamura, H.; Orimo, S. Sodium Superionic Conduction in Na2B12H12. *Chem. Commun.* **2014**, *50* (28), 3750–3752. https://doi.org/10.1039/C3CC49805K.

(63) Udovic, T. J.; Matsuo, M.; Tang, W. S.; Wu, H.; Stavila, V.; Soloninin, A. V.; Skoryunov, R. V.; Babanova, O. A.; Skripov, A. V.; Rush, J. J.; Unemoto, A.; Takamura, H.; Orimo, S. Exceptional Superionic Conductivity in Disordered Sodium Decahydro-Closo-Decaborate. *Adv. Mater.* **2014**, *26* (45), 7622–7626. https://doi.org/10.1002/adma.201403157.

(64) Duchêne, L.; Remhof, A.; Hagemann, H.; Battaglia, C. Status and Prospects of Hydroborate Electrolytes for All-Solid-State Batteries. *Energy Storage Mater.* **2020**, *25*, 782–794. https://doi.org/10.1016/j.ensm.2019.08.032.

(65) Axtell, J. C.; Saleh, L. M. A.; Qian, E. A.; Wixtrom, A. I.; Spokoyny, A. M. Synthesis and Applications of Perfunctionalized Boron Clusters. *Inorg. Chem.* **2018**, *57* (5), 2333–2350. https://doi.org/10.1021/acs.inorgchem.7b02912.

(66) Axtell, J. C.; Saleh, L. M. A.; Qian, E. A.; Wixtrom, A. I.; Spokoyny, A. M. Synthesis and Applications of Perfunctionalized Boron Clusters. *Inorg. Chem.* **2018**, *57* (5), 2333–2350. https://doi.org/10.1021/acs.inorgchem.7b02912.

(67) Knoth, W. H., M., H. C.; Sauer, J. C., B., J. H.; T., M., E. L. Chia, Y. Chemistry of Boranes. IX. Halogenation of B10H102- and B12H122-. *Inorg. Chem.* **1964**, *3* (2), 159–167.

(68) Warneke, J.; Konieczka, S. Z.; Hou, G.-L.; Aprà, E.; Kerpen, C.; Keppner, F.; Schäfer, T. C.; Deckert, M.; Yang, Z.; Bylaska, E. J.; Johnson, G. E.; Laskin, J.; Xantheas, S. S.; Wang, X.-B.; Finze, M. Properties of Perhalogenated {closo-B10} and {closo-B11} Multiply Charged Anions and a Critical Comparison with {closo-B12} in the Gas and the Condensed Phase. *Phys. Chem. Chem. Phys.* **2019**, *21* (11), 5903–5915. https://doi.org/10.1039/C8CP05313H.

(69) Amine, K.; Grove, D.; Chen, Z.; Grove, D. LITHIUM-ION BATTERIES WITH INTRINSIC PULSE OVERCHARGE PROTECTION. US 2007/0178370 A l. August 2, 2007.

(70) Trofimenko, S. Photoinduced Nucleophilic Substitution in Halogenated Clovoboranes. *J. Am. Chem. Soc.* **1966**, *88* (9), 1899–1904. https://doi.org/10.1021/ja00961a010.

(71) Trofimenko, S.; Cripps, H. N. Photoinduced Nucleophilic Substitution in Polyhedral Boranes. *J. Am. Chem. Soc.* **1965**, *87* (3), 653–654. https://doi.org/10.1021/ja01081a046.

(72) Mayer, M.; van Lessen, V.; Rohdenburg, M.; Hou, G.-L.; Yang, Z.; Exner, R. M.; Aprà, E.; Azov, V. A.; Grabowsky, S.; Xantheas, S. S.; Asmis, K. R.; Wang, X.-B.; Jenne, C.; Warneke, J. Rational Design of an Argon-Binding Superelectrophilic Anion. *Proc. Natl. Acad. Sci.* **2019**, *116* (17), 8167–8172. https://doi.org/10.1073/pnas.1820812116.

(73) Mayer, M.; Rohdenburg, M.; Lessen, V. van; C. Nierstenhöfer, M.; Aprà, E.; Grabowsky, S.; R. Asmis, K.; Jenne, C.; Warneke, J. First Steps towards a Stable Neon Compound: Observation and Bonding Analysis of [B12(CN)11Ne]-. *Chem. Commun.* **2020**. https://doi.org/10.1039/D0CC01423K.

(74) van Lessen, V. Aktivierung dreiatomiger Moleküle mit Silyliumionen und die Synthese von $[B_{12}(CN)_{12}]^{2-}$. Wissenschaftliche Abschlussarbeiten » Dissertation, Universität Wuppertal, Fakultät für Mathematik und Naturwissenschaften » Chemie » Dissertationen, 2020. https://doi.org/10.25926/g83v-q711.

(75) Rosenbaum, A. J.; Juers, D. H.; Juhasz, M. A. Copper-Promoted Cyanation of a Boron Cluster: Synthesis, X-Ray Structure, and Reactivity of 12-CN-Closo-CHB11H10–. *Inorg. Chem.* **2013**. https://doi.org/10.1021/ic4015306.

(76) Juhasz, M. A.; Juers, D. H.; Dwulet, G. E.; Rosenbaum, A. J. Tetra-ethyl-ammonium 7,12-Di-cyano-1-Carba-Closo-Dodeca-borate. *Acta Crystallogr. Sect. E Struct. Rep. Online* **2014**, *70* (4), o411–o412. https://doi.org/10.1107/S1600536814004759.

(77) Rosenmund, K. W.; Struck, E. Das Am Ringkohlenstoff Gebundene Halogen Und Sein Ersatz Durch Andere Substituenten. I. Mitteilung: Ersatz Des Halogens Durch Die Carboxylgruppe. *Berichte Dtsch. Chem. Ges. B Ser.* **1919**, *52* (8), 1749–1756. https://doi.org/10.1002/cber.19190520840.

(78) Braun, J. v; Manz, G. Fluoranthen Und Seine Derivate. III. Mitteilung. *Justus Liebigs Ann. Chem.* **1931**, *488* (1), 111–126. https://doi.org/10.1002/jlac.19314880107.

(79) Sakamoto, T.; Ohsawa, K. Palladium-Catalyzed Cyanation of Aryl and Heteroaryl Iodides with Copper(I) Cyanide. *J. Chem. Soc. Perkin 1* **1999**, No. 16, 2323–2326. https://doi.org/10.1039/A903345I.

(80) Finze, M.; Sprenger, J. A. P.; Schaack, B. B. Salts of the 1-Cyanocarba-Closo-Dodecaborate Anions [1-NC-Closo-1-CB11X11]− (X = H, F, Cl, Br, I). *Dalton Trans.* **2010**, *39* (10), 2708–2716. https://doi.org/10.1039/B922720B.

(81) Finze, M. Carbon Extrusion/Cluster Contraction: Synthesis of the Fluorinated Cyano-*Closo*-Undecaborate K_2[3-NC-Closo-$B_{11}F_{10}$]. *Angew. Chem. Int. Ed.* **2007**, *46* (46), 8880–8882. https://doi.org/10.1002/anie.200703385.

(82) Żurawiński, R.; Jakubowski, R.; Domagała, S.; Kaszyński, P.; Woźniak, K. Regioselective Functionalization of the [Closo-1-CB9H10]− Anion through Iodonium Zwitterions. *Inorg. Chem.* **2018**, *57* (16), 10442–10456. https://doi.org/10.1021/acs.inorgchem.8b01701.

(83) Kaszyński, P.; Ringstrand, B. Functionalization of Closo-Borates via Iodonium Zwitterions. *Angew. Chem. Int. Ed.* **2015**, *54* (22), 6576–6581. https://doi.org/10.1002/anie.201411858.

(84) Wingen, L. M.; Scholz, M. S. B-Cyanodicarba-Closo-Dodecaboranes: Facile Synthesis and Spectroscopic Features. *Inorg. Chem.* **2016**, *55* (17), 8274–8276. https://doi.org/10.1021/acs.inorgchem.6b01667.

(85) Grushin, V. V.; Shcherbina, T. M.; Tolstaya, T. P. The Reactions of Phenyl(B-Carboranyl)Iodonium Salts with Nucleophiles. *J. Organomet. Chem.* **1985**, *292* (1), 105–117. https://doi.org/10.1016/0022-328X(85)87326-5.

(86) Zhao, D.; Xie, Z. [3-N2-o-C2B10H11][BF4]: A Useful Synthon for Multiple Cage Boron Functionalizations of o-Carborane. *Chem. Sci.* **2016**, *7* (9), 5635–5639. https://doi.org/10.1039/C6SC01566B.

(87) Grandinetti, F. Neon behind the Signs. *Nat. Chem.* **2013**, *5* (5), 438–438. https://doi.org/10.1038/nchem.1631.

(88) Kamin, A. A.; Juhasz, M. A. Exhaustive Cyanation of the Dodecaborate Dianion: Synthesis, Characterization, and X-Ray Crystal Structure of [B12(CN)12]2–. *Inorg. Chem.* **2020**, *59* (1), 189–192. https://doi.org/10.1021/acs.inorgchem.9b03037.

(89) Juhasz, M. A.; Matheson, G. R.; Chang, P. S.; Rosenbaum, A.; Juers, D. H. Microwave-Assisted Iodination: Synthesis of Heavily Iodinated 10-Vertex and 12-Vertex Boron Clusters. *Synth. React. Inorg. Met.-Org. Nano-Met. Chem.* **2016**, *46* (4), 583–588. https://doi.org/10.1080/15533174.2014.988819.

(90) Csöregh, I.; Kierkegaard, P.; Norrestam, R. Copper(I) Tetraacetonitrile Perchlorate. *Acta Crystallogr. B* **1975**, *31* (1), 314–317. https://doi.org/10.1107/S0567740875002634.

(91) Neuhaus, A.; Dehnicke, K. Synthese und Kristallstruktur des tetrameren Nitridokomplexes [Cu(CH3CN)4]2[W4N4Cl14(CH3CN)2]. *Z. Für Anorg. Allg. Chem.* **1993**, *619* (4), 775–778. https://doi.org/10.1002/zaac.19936190423.

(92) Black, J. R.; Levason, W.; Webster, M. Tetrakis(Acetonitrile-N)Copper(I) Hexafluorophosphate(V) Acetonitrile Solvate. *Acta Crystallogr. C* **1995**, *51* (4), 623–625. https://doi.org/10.1107/S0108270194012527.

(93) Jones, P. G.; Crespo, O. Tetrakis(Acetonitrile-N)Copper(I) Tetrafluoroborate. *Acta Crystallogr. Sect. C* **1998**, *54* (1), 18–20. https://doi.org/10.1107/S0108270197013322.

(94) Knaust, J. M.; Knight, D. A.; Keller, S. W. Crystal and Molecular Structures of Several Tetrakis (Nitrile)Copper(I) Complexes. *J. Chem. Crystallogr.* **2003**, *33* (11), 813–823. https://doi.org/10.1023/A:1027445410426.

(95) Tiritiris, I.; Schleid, T.; Müller, K.; Preetz, W. Strukturelle Untersuchungen an Cs2[B12H12]. *Z. Für Anorg. Allg. Chem.* **2000**, *626* (2), 323–325. https://doi.org/10.1002/(SICI)1521-3749(200002)626:2<323::AID-ZAAC323>3.0.CO;2-Q.

(96) Tiritiris, I.; Schleid, T. Single Crystals of the Dodecaiodo-Closo-Dodecaborate Cs2[B12I12] · 2 CH3CN (≡ Cs(NCCH3)2[B12I12]) from Acetonitrile. *Z. Für Anorg. Allg. Chem.* **2001**, *627* (12), 2568–2570. https://doi.org/10.1002/1521-3749(200112)627:12<2568::AID-ZAAC2568>3.0.CO;2-0.

(97) Dwulet, G. E.; Juhasz, M. A. A Boron Cluster with a Pair of Carboxylic Acid Groups on Adjacent Borons: Synthesis and Structure of 7,12-(COOH)2-CB11H10−. *Inorg. Chem. Commun.* **2015**, *51*, 26–28. https://doi.org/10.1016/j.inoche.2014.10.028.

(98) Aaron Rosenbaum. Microwave-Assisted Metal-Catalyzed Reactions of Halogenated Carboranes. Undergraduate Thesis, Whiman College, Walla Walla, WA, 2012.

(99) Wu, H.; Tang, W. S.; Stavila, V.; Zhou, W.; Rush, J. J.; Udovic, T. J. Structural Behavior of Li2B10H10. *J. Phys. Chem. C* **2015**, *119* (12), 6481–6487. https://doi.org/10.1021/acs.jpcc.5b00533.

(100) Hofmann, K.; Albert, B. Crystal Structure of Bis(Triethylammonium)Closo-Decahydrodecaborate, [(C2H5)3NH]2[B10H10]. *Z. Für Naturforschung B* **2000**, *55* (6), 499–503. https://doi.org/10.1515/znb-2000-0610.

(101) Plesek, J.; Jelinek, T.; Dradakova, E.; Hermanek, S.; stibr, B. A Convenient Preparation of 1-CB11H12- and Its C-Amino Derivatives. *Collect. Czechoslov. Chem. Commun.* **1984**, *49* (7), 1559–1562.

(102) Ringstrand, B.; Bateman, D.; Shoemaker, R. K.; Janoušek, Z. Improved Synthesis of [Closo-1-CB9H10]– Anion and New C-Substituted Derivatives. *Collect. Czechoslov. Chem. Commun.* **2009**, *74* (3), 419–431. https://doi.org/10.1135/cccc2008151.

(103) Hawthorne, M. F.; Pilling, R. L.; Knoth, W. H. Bis(Triethylammonium) Decahydrodecaborate(2−). In *Inorganic Syntheses*; Tyree, Jr., S. Y., Ed.; John Wiley & Sons, Inc., 1967; Vol. 9, pp 16–19.

(104) Dolomanov, O. V.; Bourhis, L. J.; Gildea, R. J.; Howard, J. a. K.; Puschmann, H. OLEX2: A Complete Structure Solution, Refinement and Analysis Program. *J. Appl. Crystallogr.* **2009**, *42* (2), 339–341. https://doi.org/10.1107/S0021889808042726.

(105) Sheldrick, G. M. A Short History of SHELX. *Acta Crystallogr. A* **2008**, *64* (1), 112–122. https://doi.org/10.1107/S0108767307043930.

(106) Sheldrick, G. M. Crystal Structure Refinement with SHELXL. *Acta Crystallogr. Sect. C Struct. Chem.* **2015**, *71* (1), 3–8. https://doi.org/10.1107/S2053229614024218.

(107) Bourhis, L. J.; Dolomanov, O. V.; Gildea, R. J.; Howard, J. a. K.; Puschmann, H. The Anatomy of a Comprehensive Constrained, Restrained Refinement Program for the Modern Computing Environment – Olex2 Dissected. *Acta Crystallogr. Sect. Found. Adv.* **2015**, *71* (1), 59–75. https://doi.org/10.1107/S2053273314022207.

(108) Becke, A. D. Density-functional Thermochemistry. III. The Role of Exact Exchange. *J. Chem. Phys.* **1993**, *98* (7), 5648–5652. https://doi.org/10.1063/1.464913.

(109) Lee, C.; Yang, W.; Parr, R. G. Development of the Colle-Salvetti Correlation-Energy Formula into a Functional of the Electron Density. *Phys. Rev. B* **1988**, *37* (2), 785–789. https://doi.org/10.1103/PhysRevB.37.785.

(110) Vosko, S. H.; Wilk, L.; Nusair, M. Accurate Spin-Dependent Electron Liquid Correlation Energies for Local Spin Density Calculations: A Critical Analysis. *Can. J. Phys.* **1980**, *58* (8), 1200–1211. https://doi.org/10.1139/p80-159.

(111) Stephens, P. J.; Devlin, F. J.; Chabalowski, C. F.; Frisch, M. J. Ab Initio Calculation of Vibrational Absorption and Circular Dichroism Spectra Using Density Functional Force Fields. *J. Phys. Chem.* **1994**, *98* (45), 11623–11627. https://doi.org/10.1021/j100096a001.

(112) Weigend, F.; Ahlrichs, R. Balanced Basis Sets of Split Valence, Triple Zeta Valence and Quadruple Zeta Valence Quality for H to Rn: Design and Assessment of Accuracy. *Phys. Chem. Chem. Phys.* **2005**, *7* (18), 3297–3305. https://doi.org/10.1039/B508541A.

(113) Neese, F. The ORCA Program System. *WIREs Comput. Mol. Sci.* **2012**, *2* (1), 73–78. https://doi.org/10.1002/wcms.81.

(114) Neese, F. Software Update: The ORCA Program System, Version 4.0. *WIREs Comput. Mol. Sci.* **2018**, *8* (1), e1327. https://doi.org/10.1002/wcms.1327.

(115) Zhurko, G.A.; Zhurko, D.A. *Chemcraft*; Version 1.8 (Build 574). www.chemcraftprog.com.

(116) Frisch, M. J.; Pople, J. A.; Binkley, J. S. Self-consistent Molecular Orbital Methods 25. Supplementary Functions for Gaussian Basis Sets. *J. Chem. Phys.* **1984**, *80* (7), 3265–3269. https://doi.org/10.1063/1.447079.

(117) Frisch, M. J.; Trucks, G. W.; Schlegel, H. B.; Scuseria, G. E.; Robb, M. A.; Cheeseman, J. R.; Montgomery, Jr., J. A.; Vreven, T.; Kudin, K. N.; Burant, J. C.; Millam, J. M.; Iyengar, S. S.; Tomasi, J.; Barone, V.; Mennucci, B.; Cossi, M.; Scalmani, G.; Rega, N.; Petersson, G. A.; Nakatsuji, H.; Hada, M.; Ehara, M.; Toyota, K.; Fukuda, R.; Hasegawa, J.; Ishida, M.; Nakajima, T.; Honda, Y.; Kitao, O.; Nakai, H.; Klene, M.; Li, X.; Knox, J. E.; Hratchian, H. P.; Cross, J. B.; Bakken, V.; Adamo, C.; Jaramillo, J.; Gomperts, R.; Stratmann, R. E.; Yazyev, O.; Austin, A. J.; Cammi, R.; Pomelli, C.; Ochterski, J. W.; Ayala, P. Y.; Morokuma, K.; Voth, G. A.; Salvador, P.; Dannenberg, J. J.; Zakrzewski, V. G.; Dapprich, S.; Daniels, A. D.; Strain, M. C.; Farkas, O.; Malick, D. K.; Rabuck, A. D.; Raghavachari, K.; Foresman, J. B.; Ortiz, J. V.; Cui, Q.; Baboul, A. G.; Clifford, S.; Cioslowski, J.; Stefanov, B. B.; Liu, G.; Liashenko, A.; Piskorz, P.; Komaromi, I.; Martin, R. L.; Fox, D. J.; Keith, T.; Al-Laham, M. A.; Peng, C. Y.; Nanayakkara, A.; Challacombe, M.; Gill, P. M. W.; Johnson, B.; Chen, W.; Wong, M. W.; Gonzalez, C.; and Pople, J. A. *Gaussian 03, Revision C.02*; Gaussian Inc.: Wallingford CT, 2004.

(118) Andersson, M. P.; Uvdal, P. New Scale Factors for Harmonic Vibrational Frequencies Using the B3LYP Density Functional Method with the Triple-ζ Basis Set 6-311+G(d,p). *J. Phys. Chem. A* **2005**, *109* (12), 2937–2941. https://doi.org/10.1021/jp045733a.

(119) Adamo, C.; Barone, V. Toward Reliable Density Functional Methods without Adjustable Parameters: The PBE0 Model. *J. Chem. Phys.* **1999**, *110* (13), 6158–6170. https://doi.org/10.1063/1.478522.

7. APPENDIX A: SUPPORTING INFORMATION

7.1 Relevant Spectra

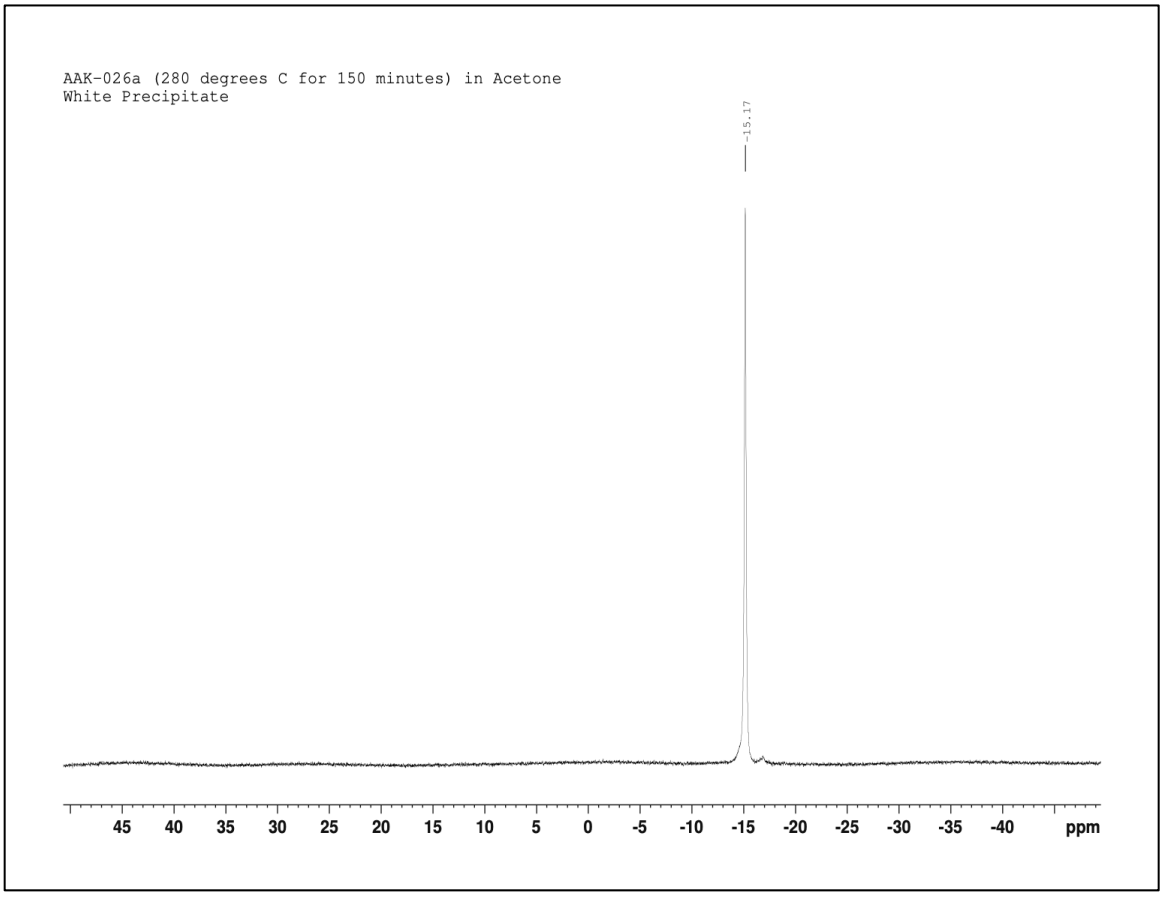

Figure A1. ^{11}B NMR spectrum of $[Et_4N]_2[B_{12}I_{12}]$ in acetone-d_6.

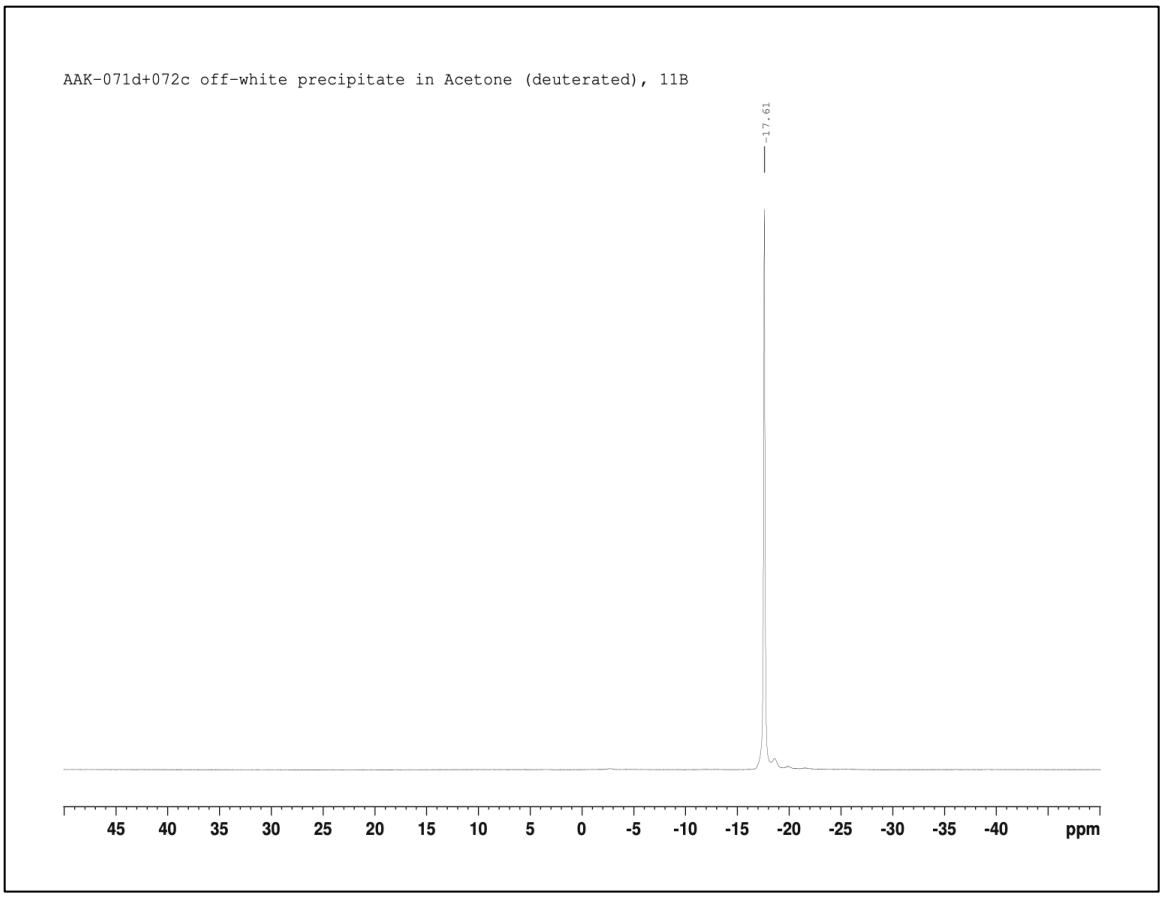

Figure A2. ^{11}B NMR spectrum of $[Et_4N]_2[B_{12}(CN)_{12}]$ in acetone-d_6.

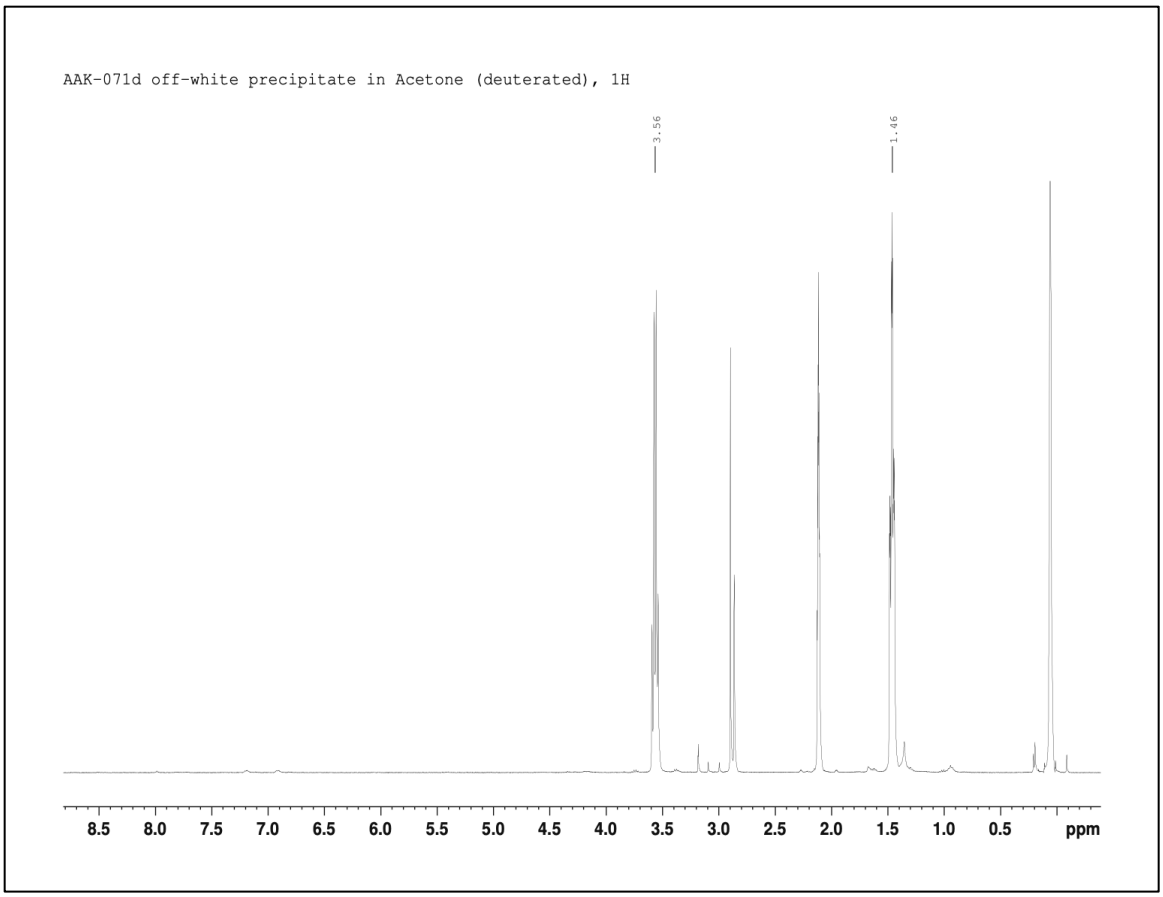

Figure A3. ^{1}H NMR spectrum of $[Et_4N]_2[B_{12}(CN)_{12}]$ in acetone-d_6.

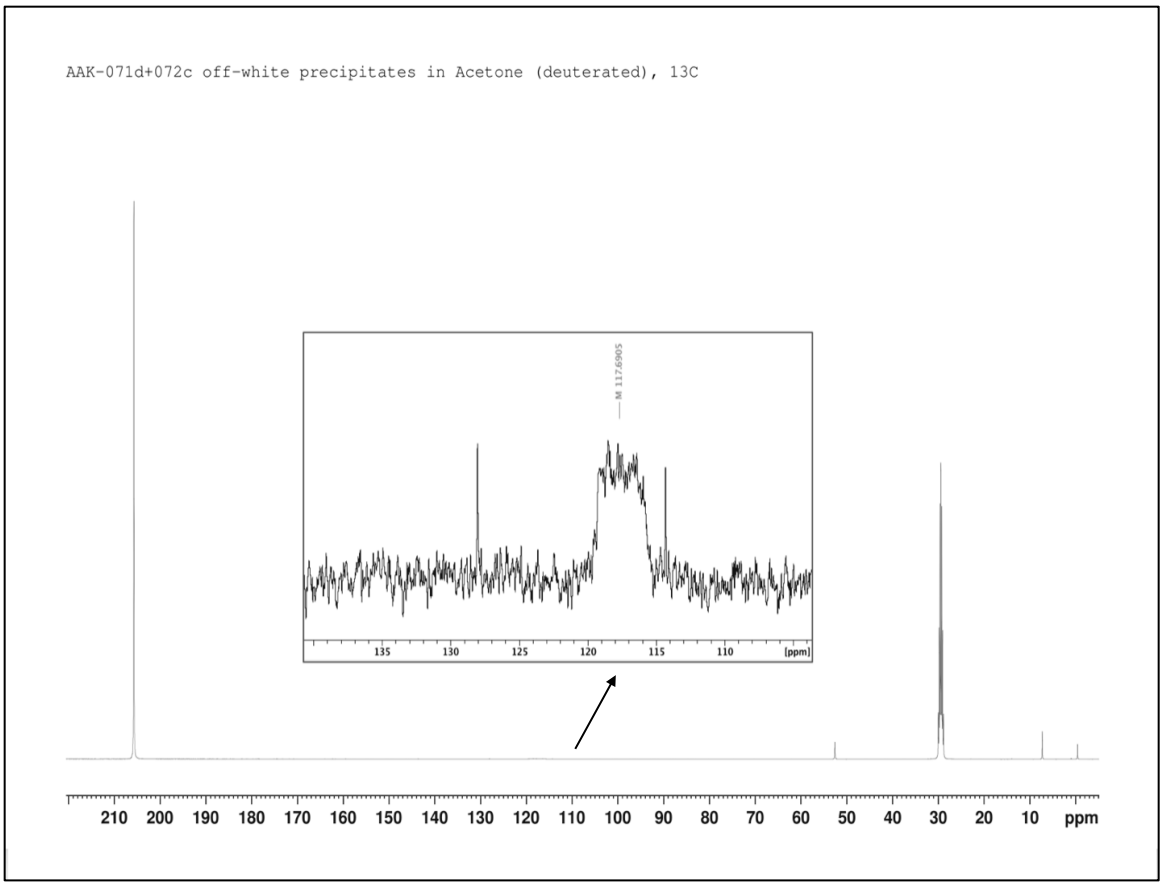

Figure A4. ^{13}C NMR spectrum of $[Et_4N]_2[B_{12}(CN)_{12}]$ in acetone-d_6.

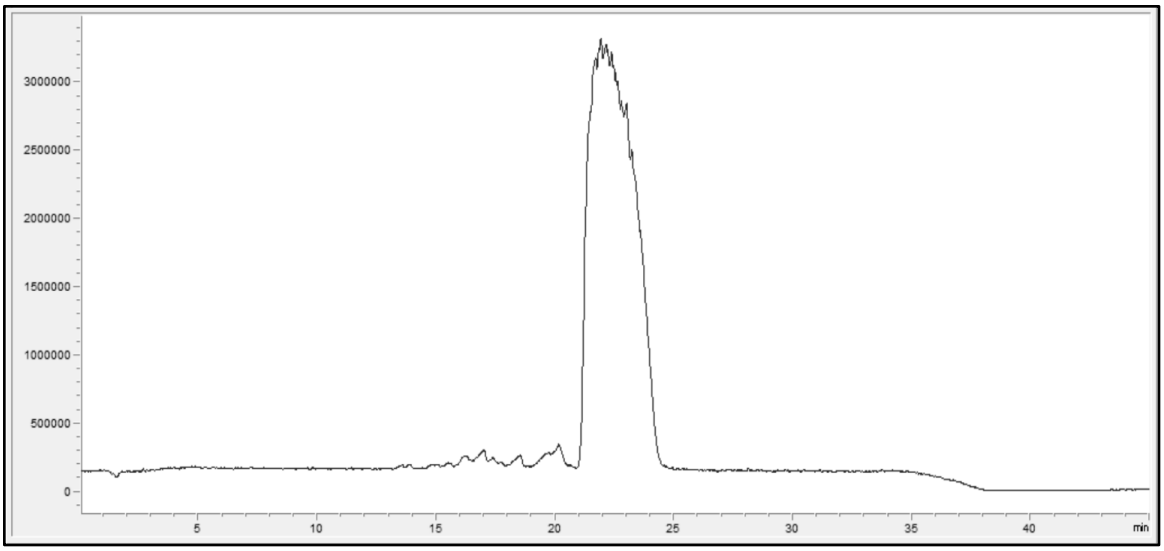

Figure A5. LC-MS chromatogram of $[B_{12}(CN)_{12}]^{2-}$ in negative ion mode (range: *m/z* = 70-2000).

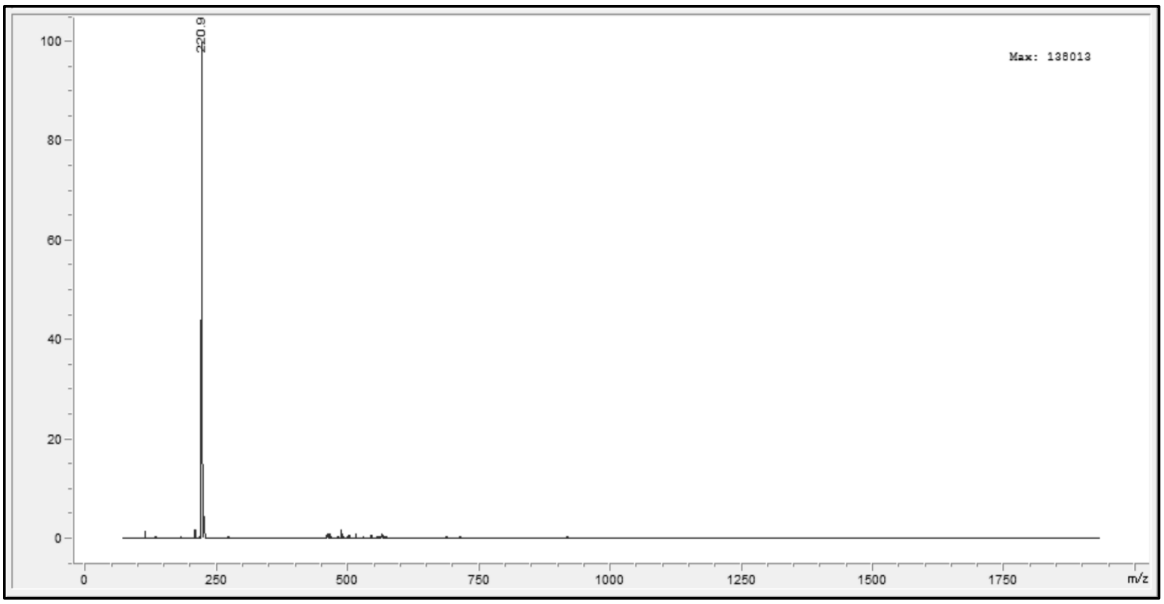

Figure A6. LC-MS negative ion mass spectrum corresponding to the $[B_{12}(CN)_{12}]^{2-}$ peak in Figure A5 from 20.9 min until 24.4 min.

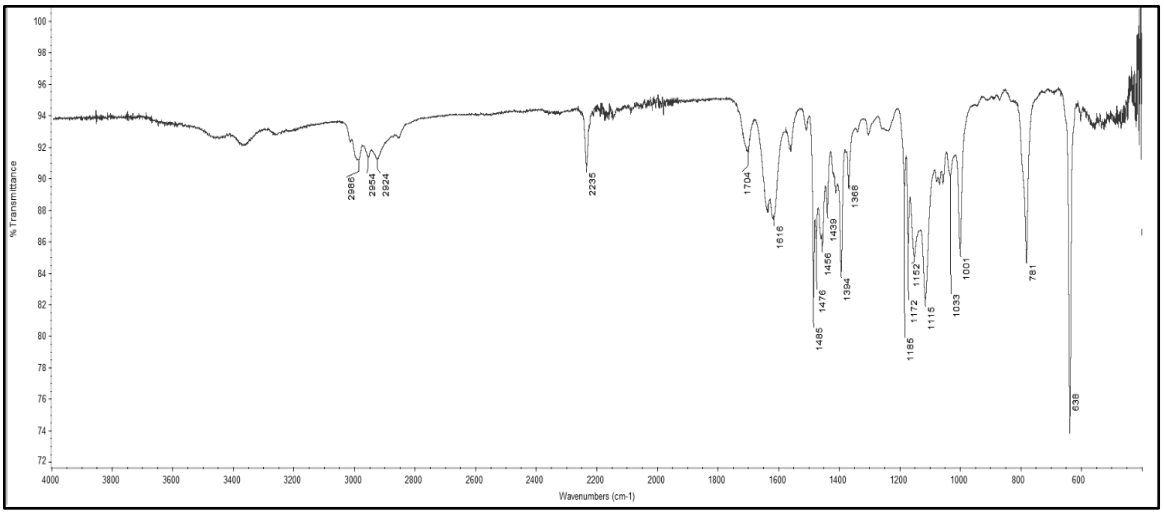

Figure A7. FTIR spectrum of $[Et_4N]_2[B_{12}(CN)_{12}]$.

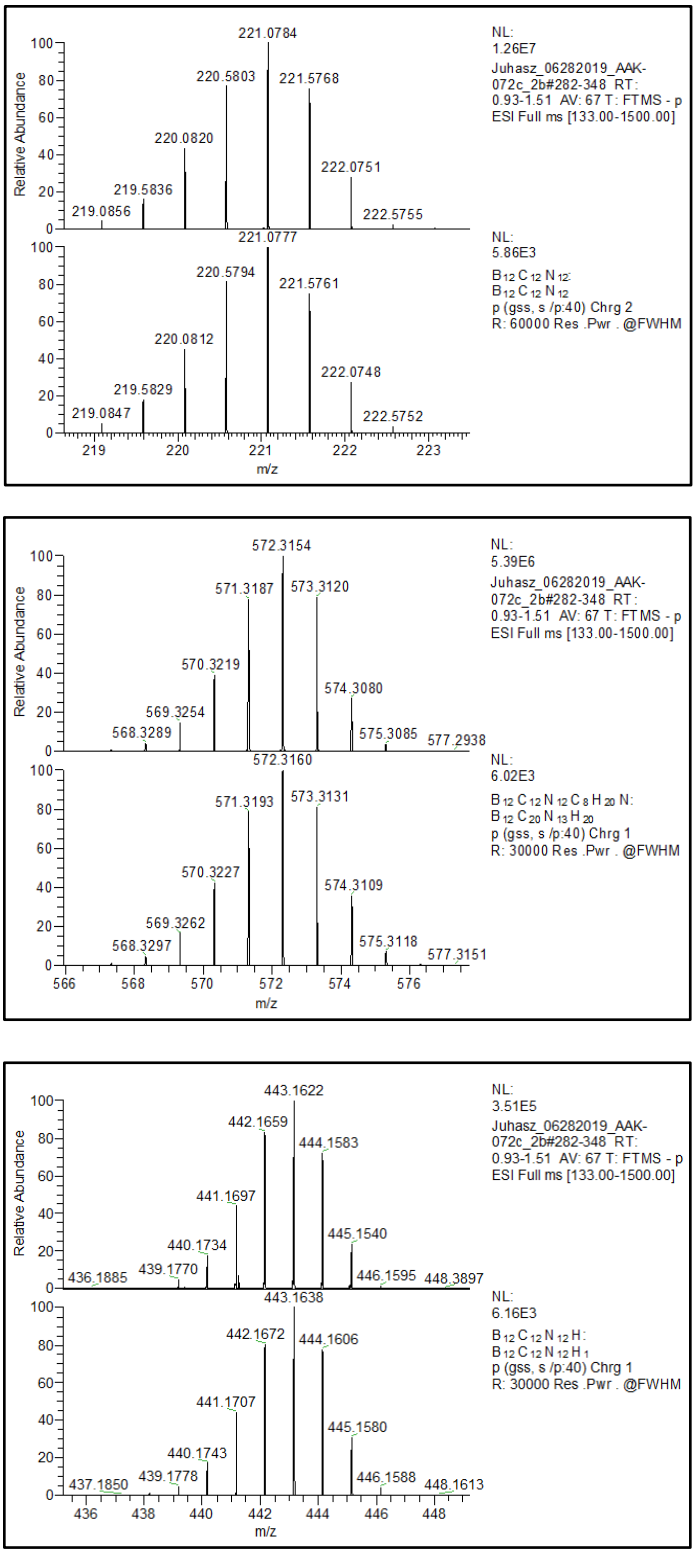

Figure A8. HRMS analysis of $[B_{12}(CN)_{12}]^{2-}$, which was detected in three separate forms: **(A)** $[B_{12}(CN)_{12}]^{2-}$, **(B)** $[Et_4N][(B_{12}(CN)_{12})]^-$, and **(C)** $H[B_{12}(CN)_{12}]^-$. A calculated theoretical mass spectrum is displayed below the experimental spectrum for each ion.

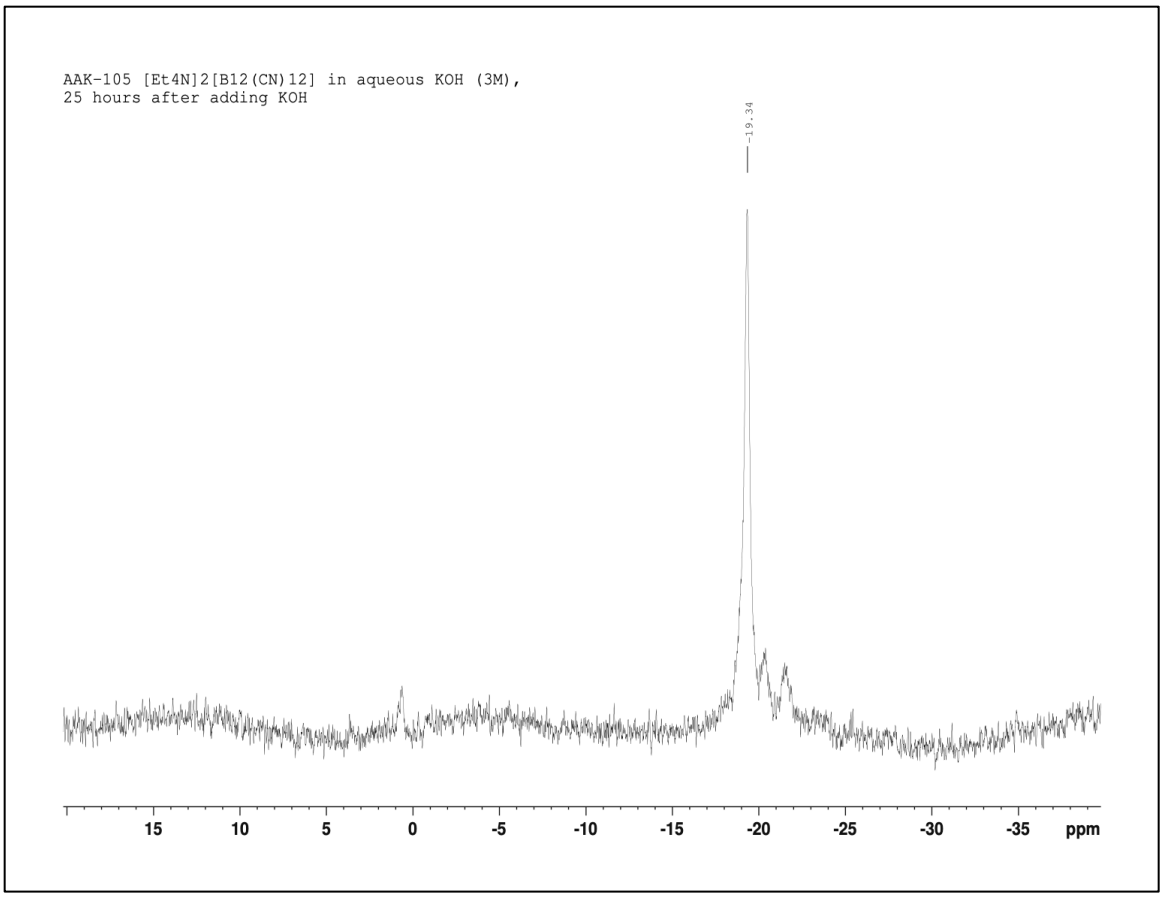

Figure A9. ^{11}B NMR spectrum of $[Et_4N]_2[B_{12}(CN)_{12}]$ after >24 hr in 3M KOH in 5% aqueous CH_3CN.

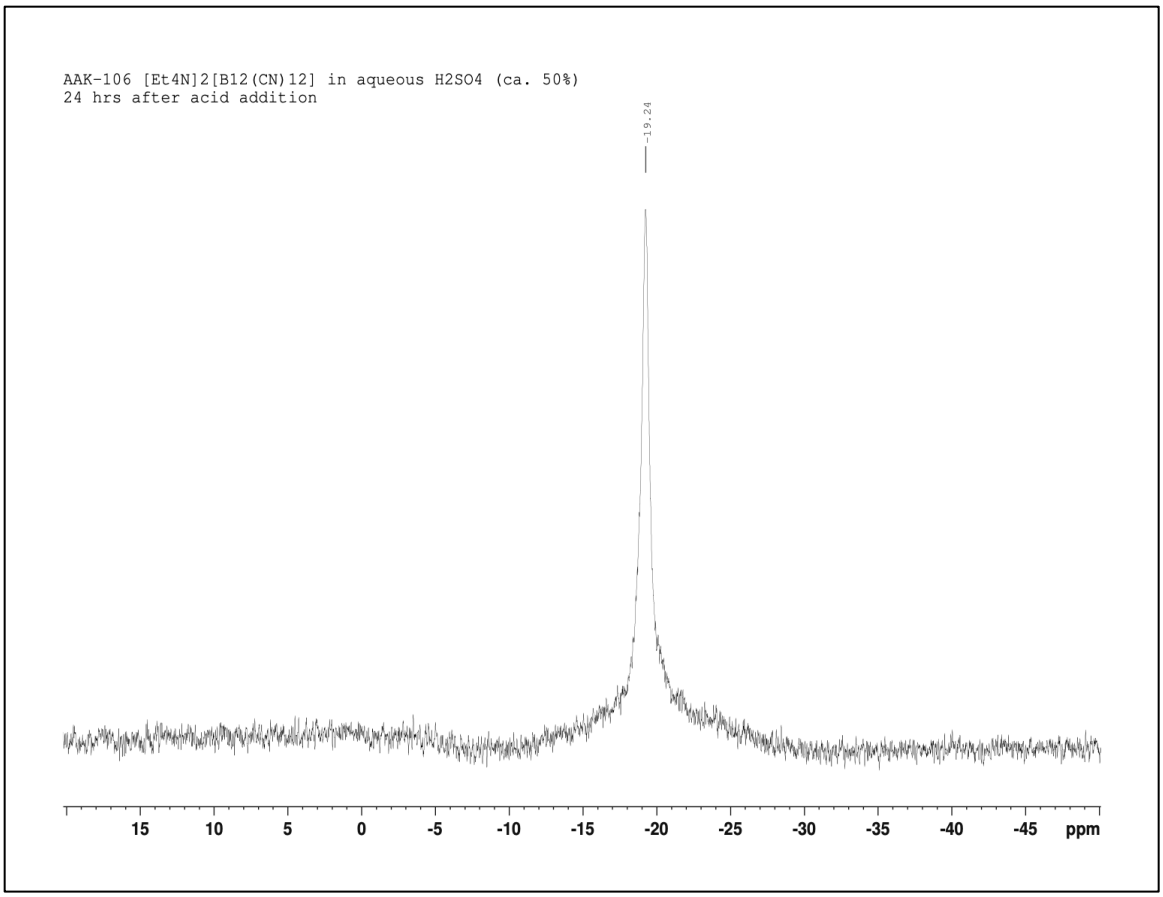

Figure A10. ^{11}B NMR spectrum of $[Et_4N]_2[B_{12}(CN)_{12}]$ after 24 hr in 50% H_2SO_4.

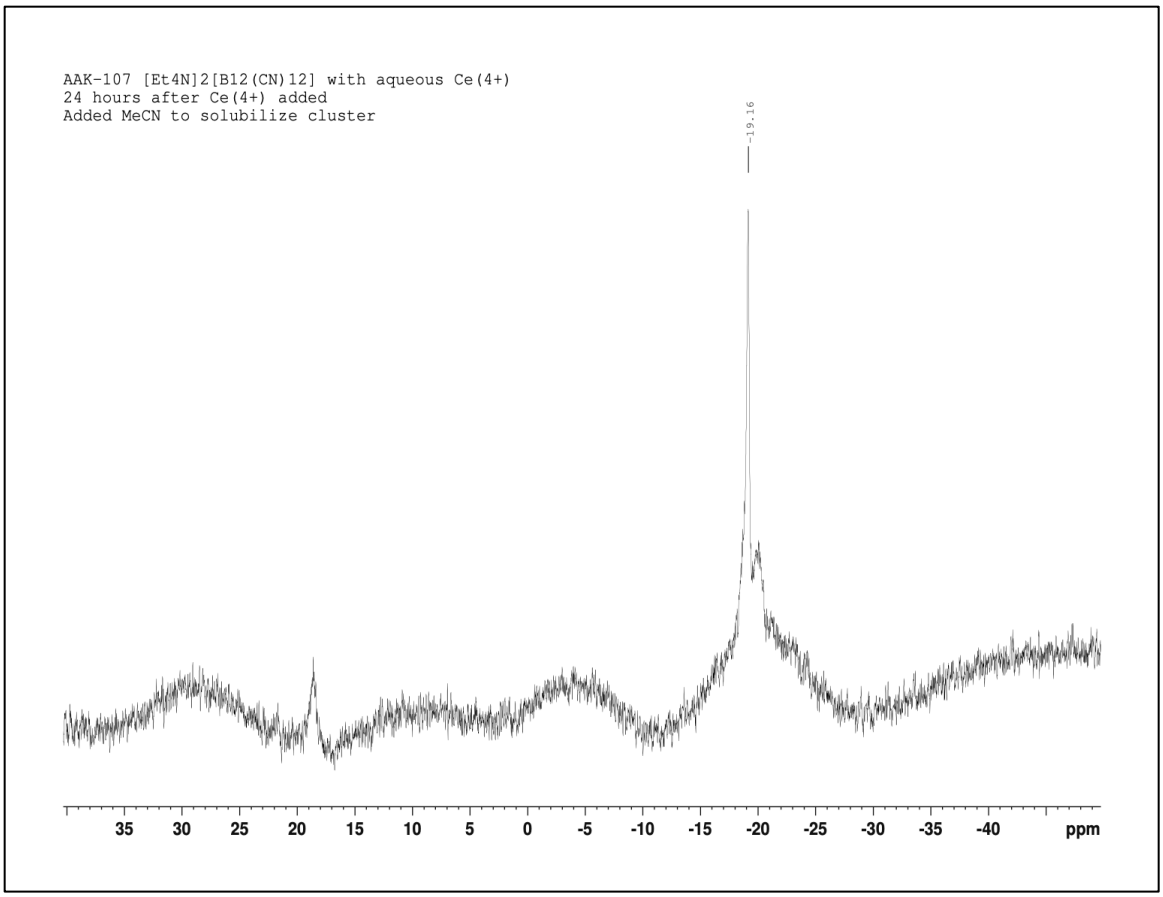

Figure A11. ^{11}B NMR spectrum of $[Et_4N]_2[B_{12}(CN)_{12}]$ after 24 hr in the presence of excess aqueous Ce^{4+}.

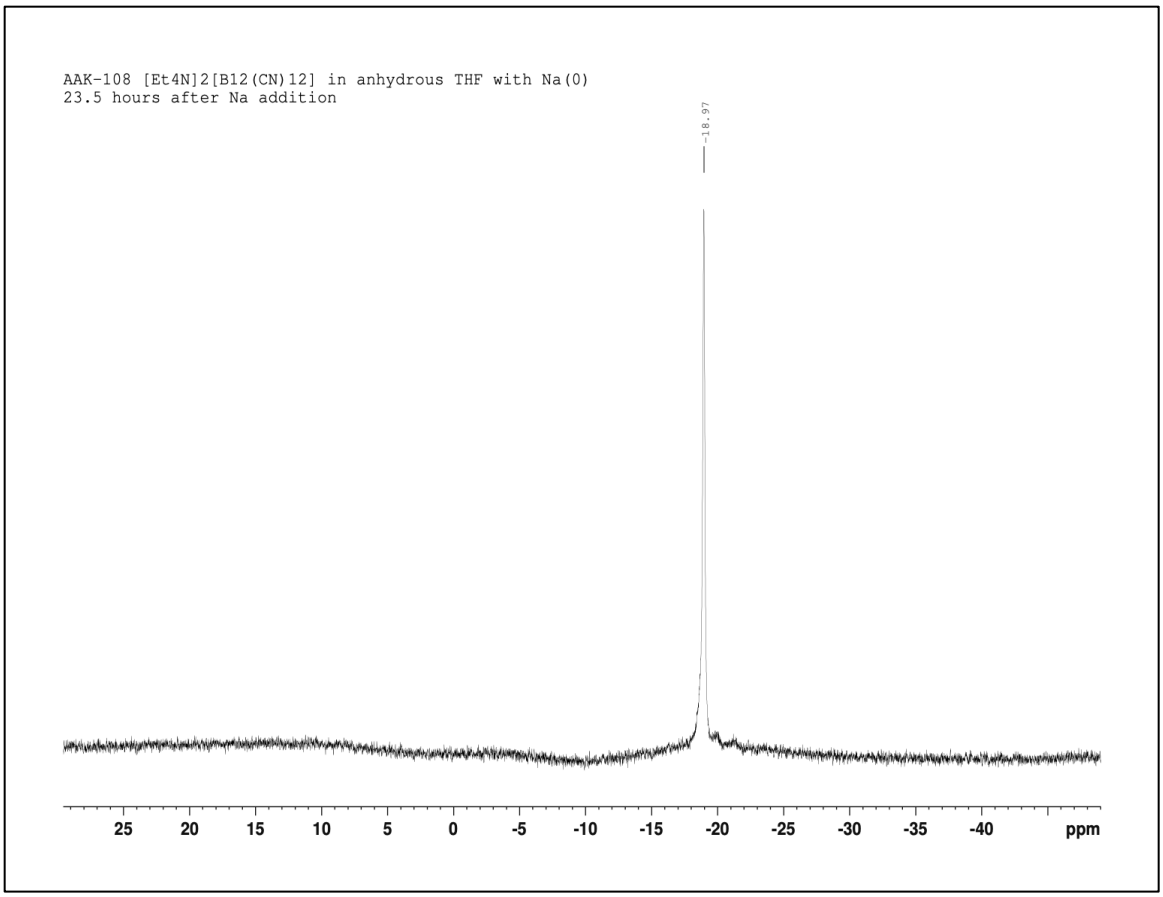

Figure A12. ^{11}B NMR spectrum of $[Et_4N]_2[B_{12}(CN)_{12}]$ after ca. 24 hr in the presence of Na in THF.

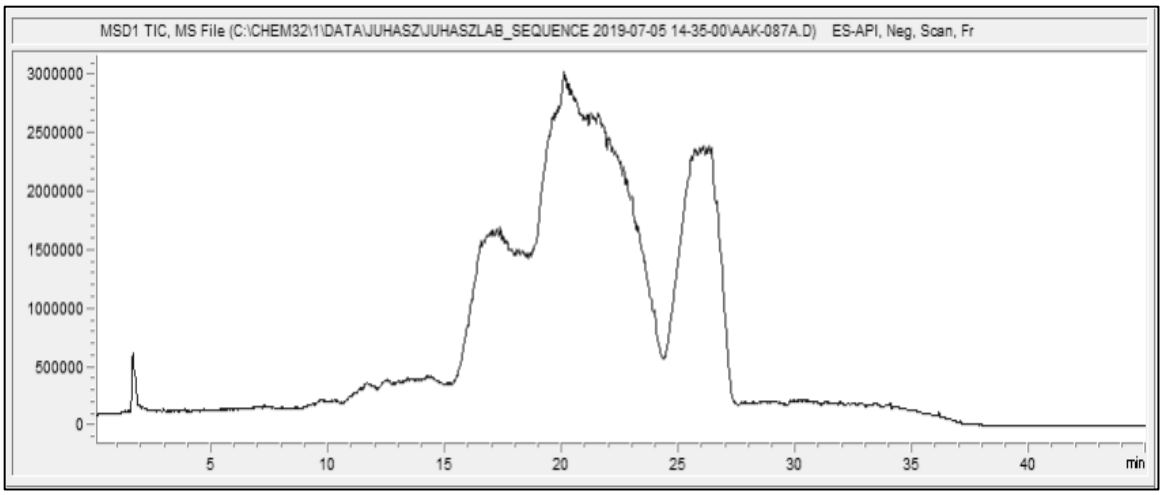

Figure A13. LC-MS negative ion chromatogram (range: *m/z* = 70-2000) showing the partial acid hydrolysis of $[B_{12}(CN)_{12}]^{2-}$ after 48 hr under reflux in aqueous HCl and HOAc.

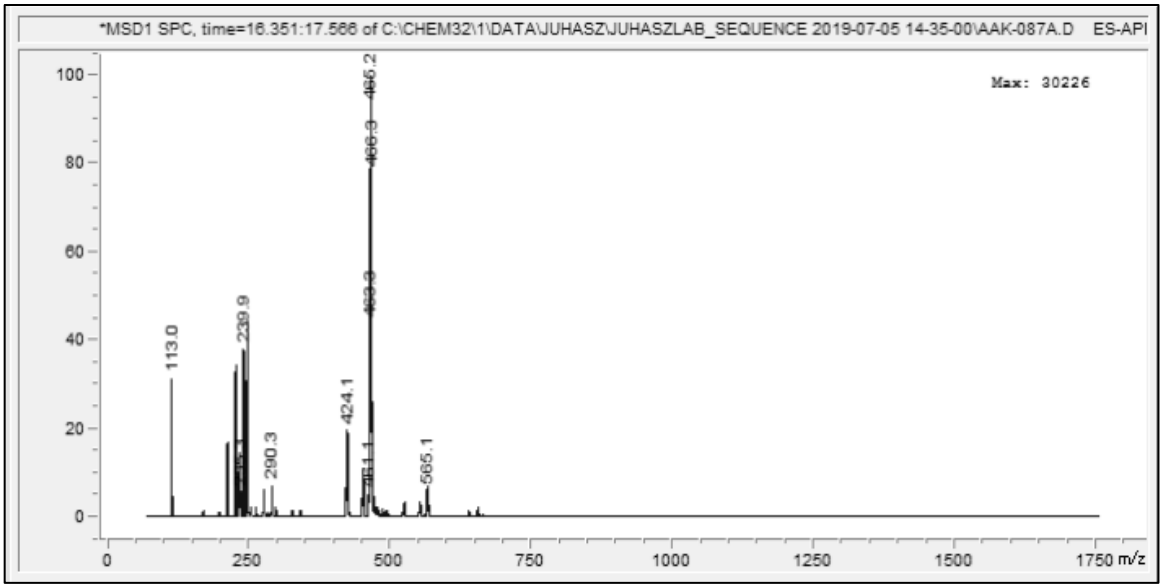

Figure A14. LC-MS negative ion mass spectrum corresponding to Figure A13 from 16.4 min until 17.6 min. The peak at *m/z* = 239.9 corresponds to $[B_{12}(CN)_{10}(COOH)_2]^{2-}$ (calc'd *m/z* = 240). The major peak at *m/z* = 465.2 has not been identified. The peak at *m/z* = 113.0 is trifluoroacetate carry-over from a previous user's solvent system.

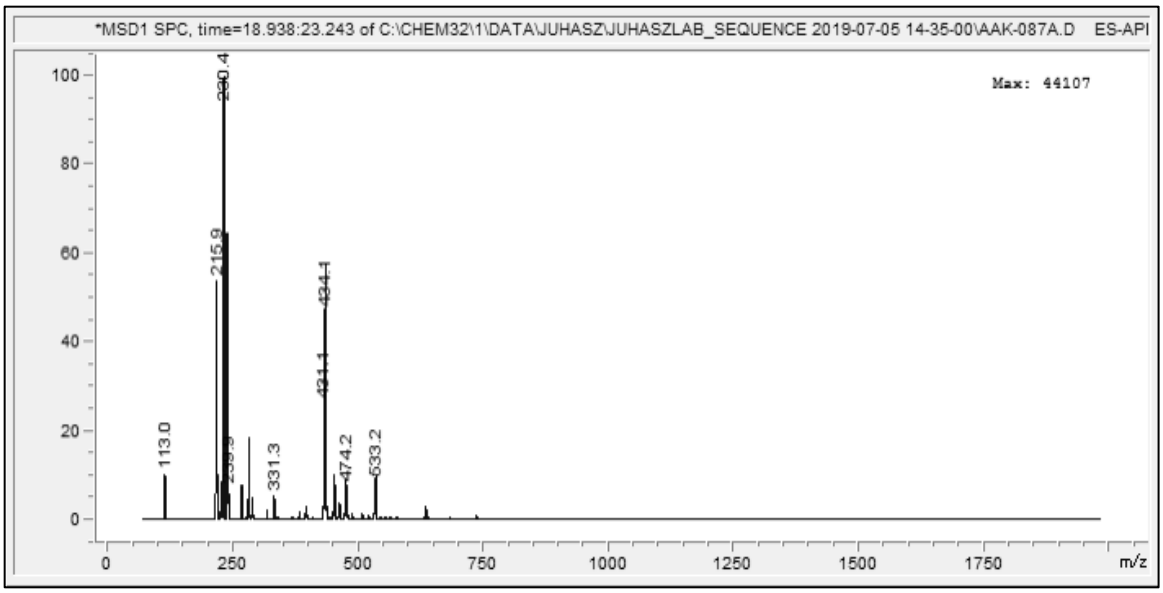

Figure A15. LC-MS negative ion mass spectrum corresponding to Figure A13 from 18.9 min until 23.2 min. The peak at m/z = 230.4 corresponds to $[B_{12}(CN)_{11}(COOH)]^{2-}$ (calc'd m/z = 230.5).

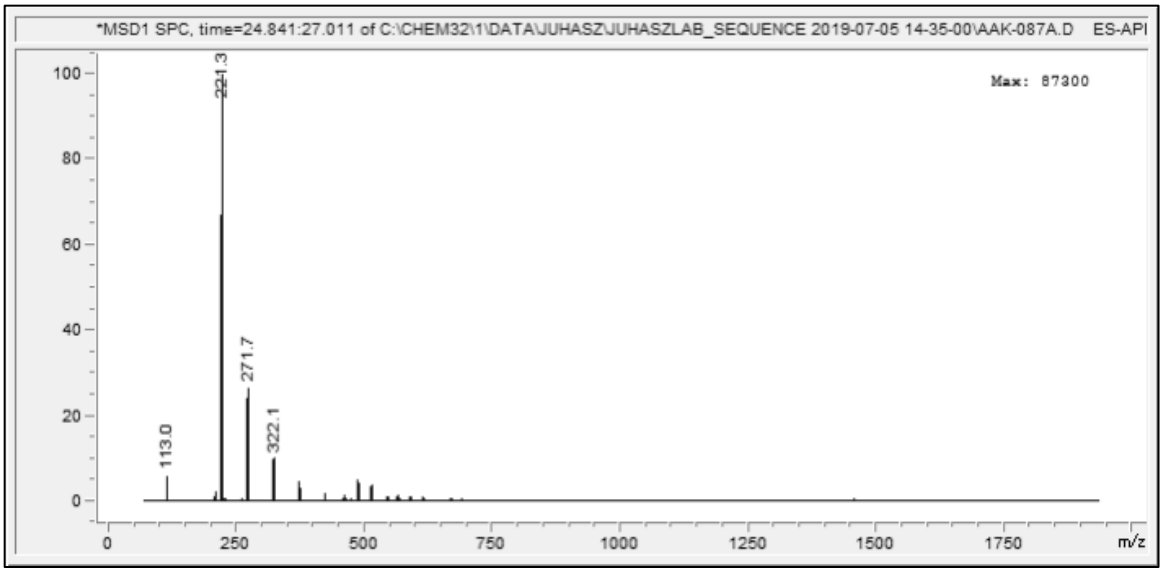

Figure A16. LC-MS negative ion mass spectrum corresponding to Figure A13 from 24.8 min until 27.0 min. The peak at m/z = 221.3 corresponds to $[B_{12}(CN)_{12}]^{2-}$ (calc'd m/z = 221).

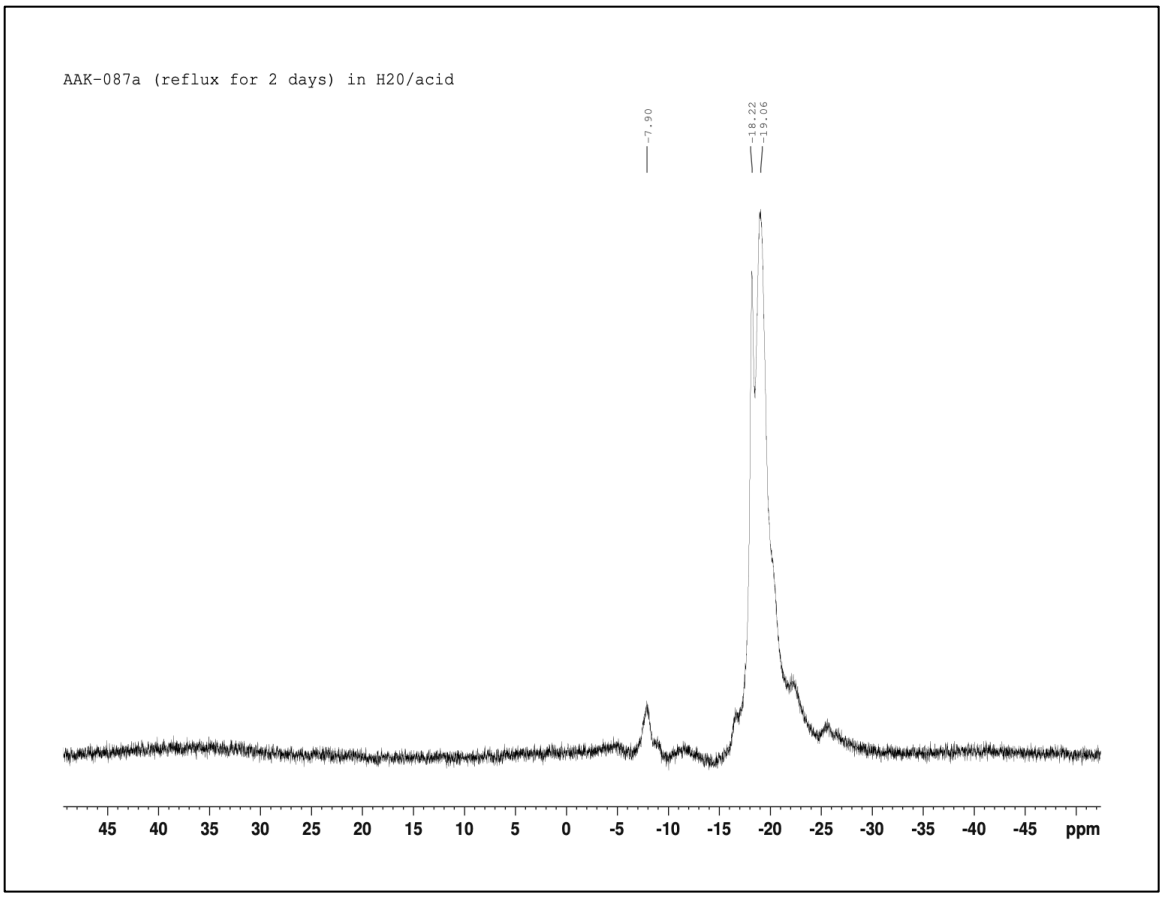

Figure A17. ^{11}B NMR spectrum showing the partial acid hydrolysis of $[B_{12}(CN)_{12}]^{2-}$ after 2 days under reflux in aqueous HCl and HOAc.

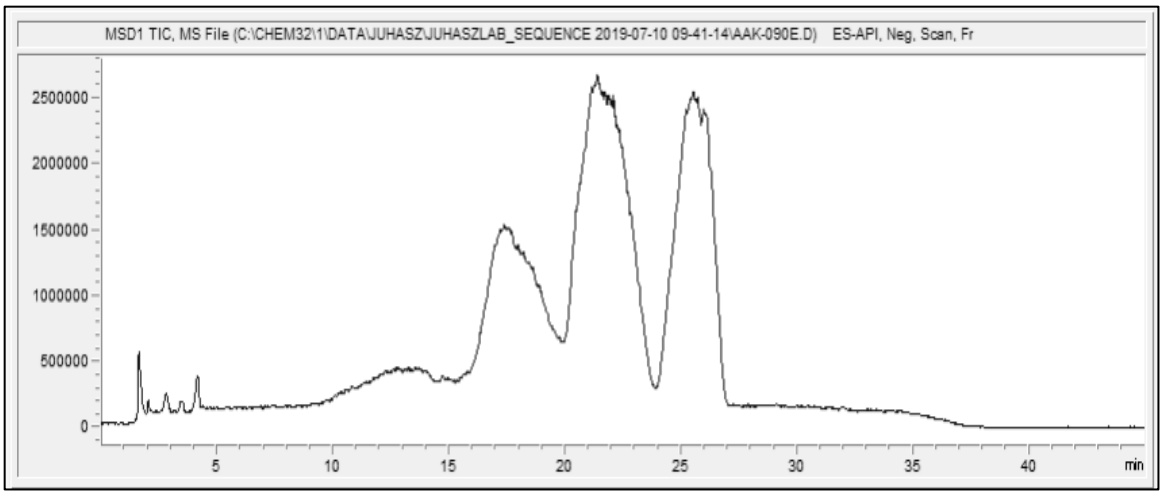

Figure A18. LC-MS negative ion chromatogram (range: *m/z* = 70-2000) showing the partial acid hydrolysis of $[B_{12}(CN)_{12}]^{2-}$ after heating for 8 hr at 120–140 ˚C under MWI in aqueous HCl and HOAc.

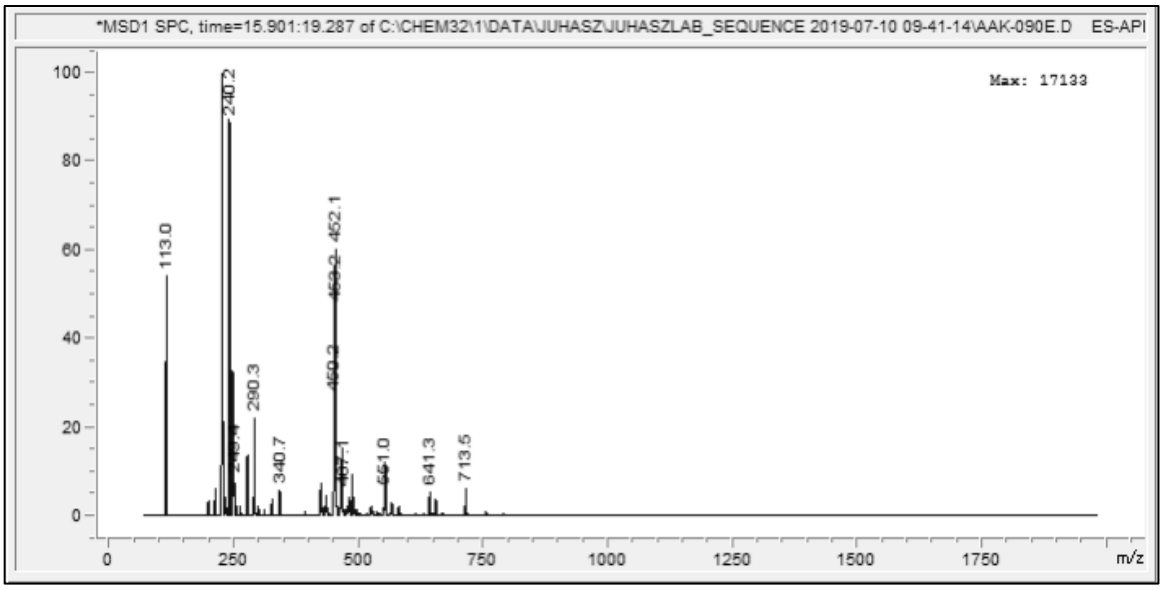

Figure A19. LC-MS negative ion mass spectrum corresponding to Figure A18 from 15.9 min until 19.3 min. The peak at *m/z* = 240.2 corresponds to $[B_{12}(CN)_{10}(COOH)_2]^{2-}$ (calc'd *m/z* = 240). The peak at *m/z* = 113.0 is trifluoroacetate carry-over from a previous user's solvent system.

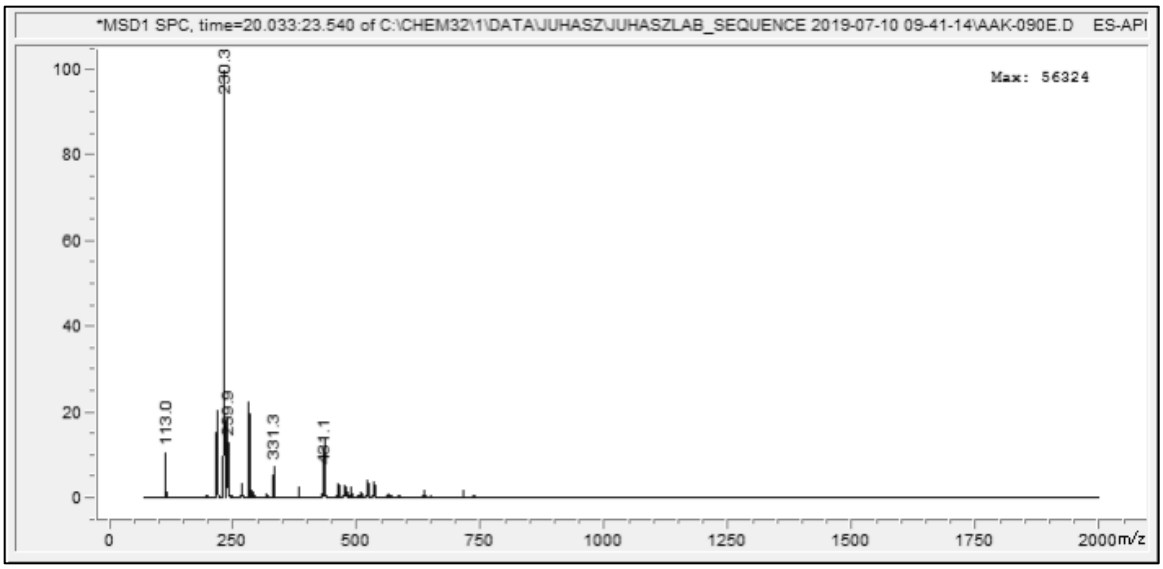

Figure A20. LC-MS negative ion mass spectrum corresponding to Figure A18 from 20.3 min until 23.5 min. The peak at m/z = 230.3 corresponds to $[B_{12}(CN)_{11}(COOH)]^{2-}$ (calc'd m/z = 230.5).

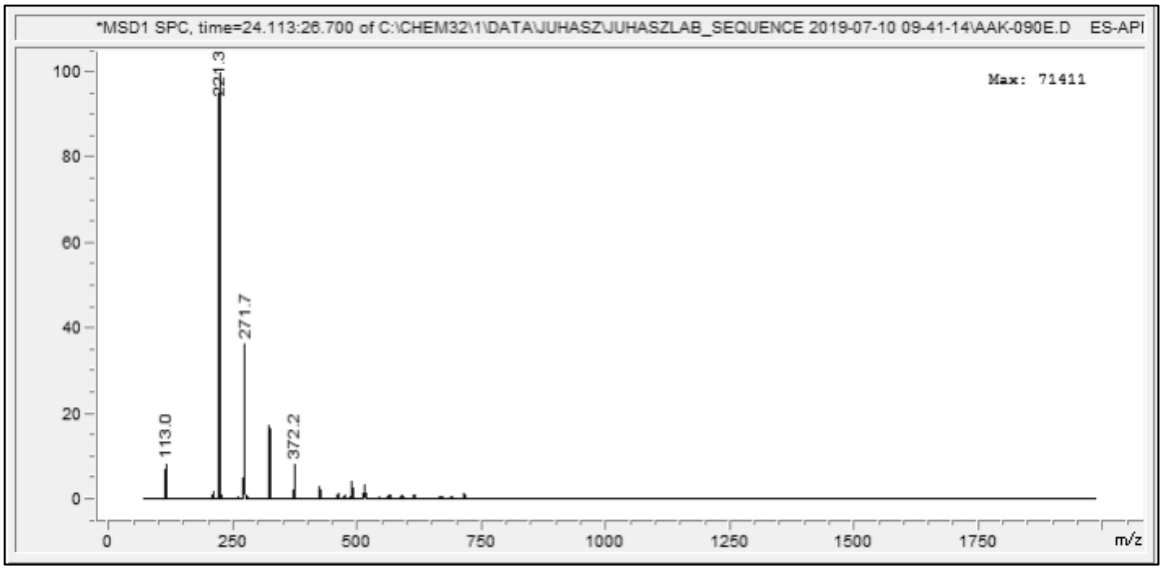

Figure A21. LC-MS negative ion mass spectrum corresponding to Figure A18 from 24.1 min until 26.7 min. The peak at m/z = 221.3 corresponds to $[B_{12}(CN)_{12}]^{2-}$ (calc'd m/z = 221).

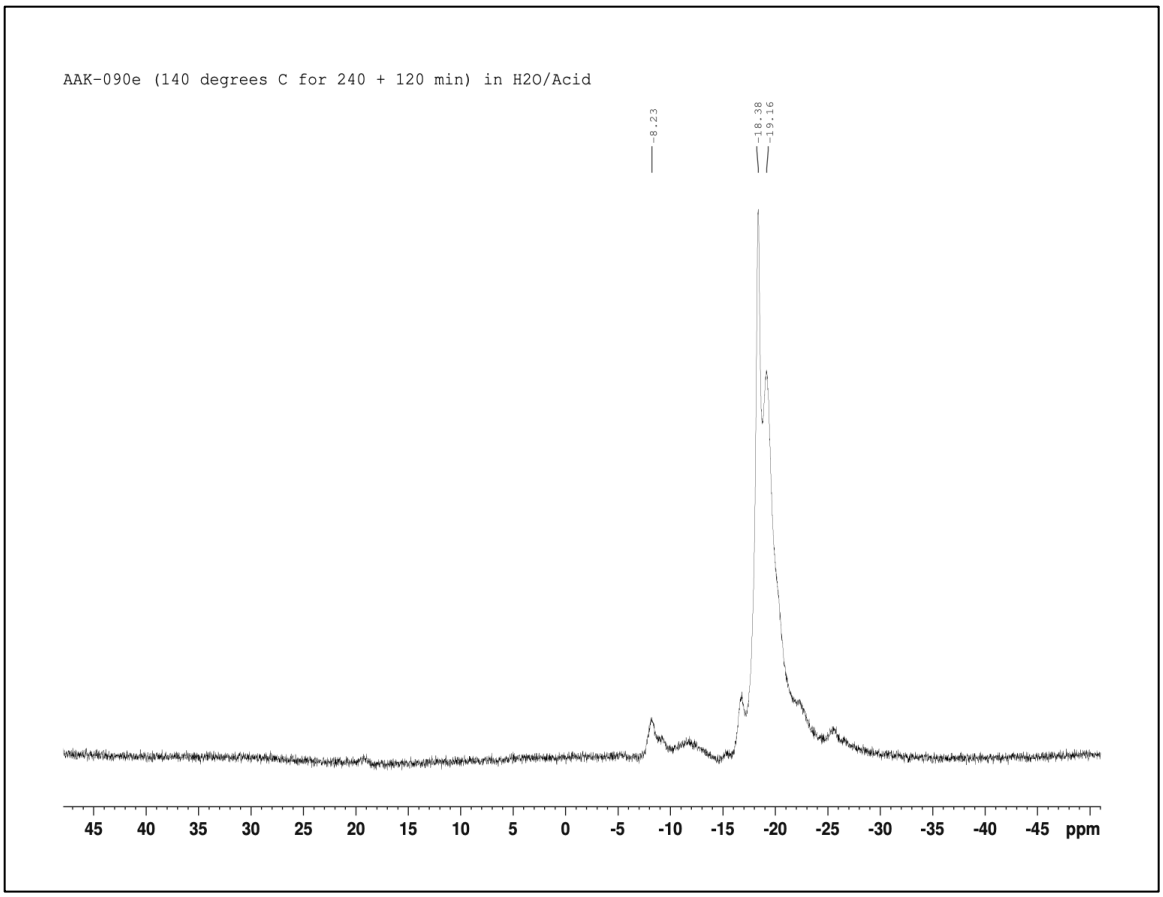

Figure A22. ^{11}B NMR spectrum showing the partial acid hydrolysis of $[B_{12}(CN)_{12}]^{2-}$ after heating for 8 hr at 120–140 ˚C under MWI in aqueous HCl and HOAc.

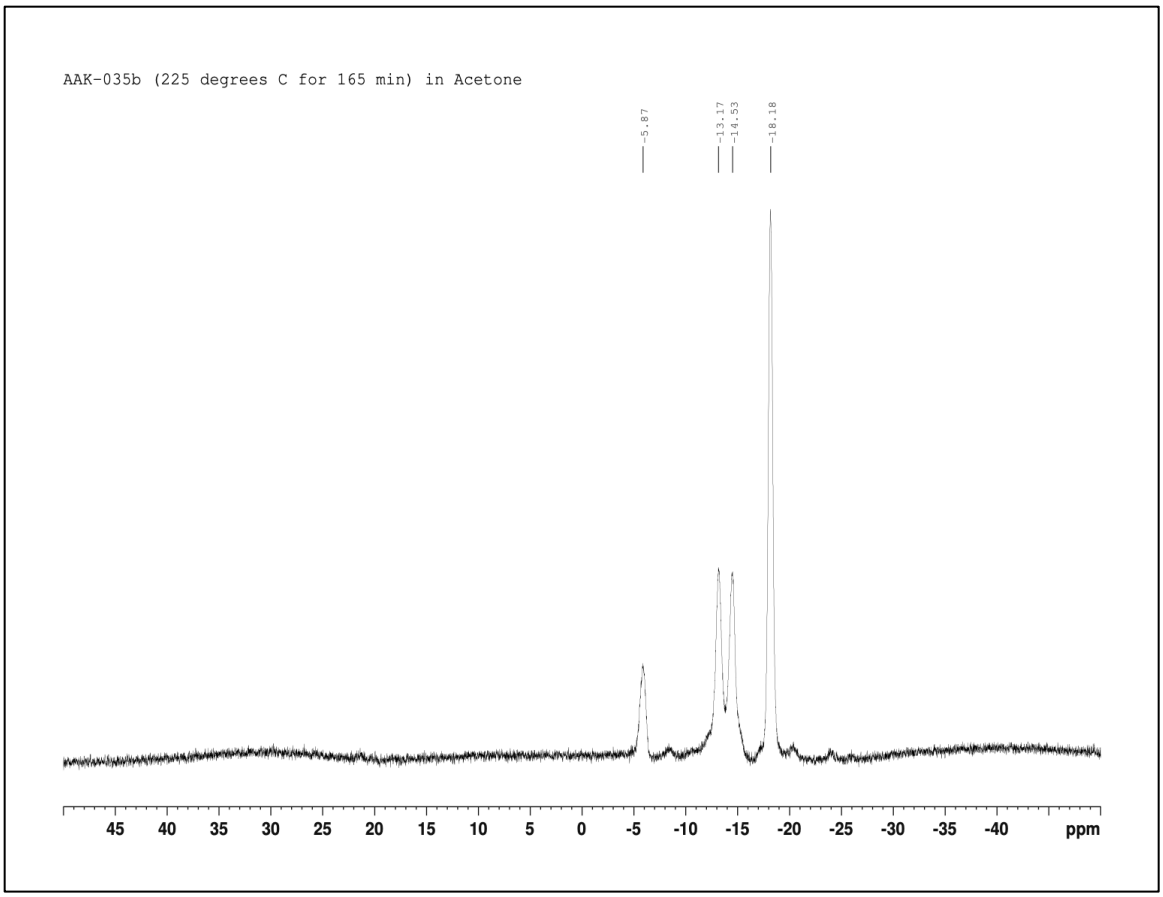

Figure A23. ^{11}B NMR spectrum of $[Et_4N][CB_{11}H_6I_6]$ in acetone.

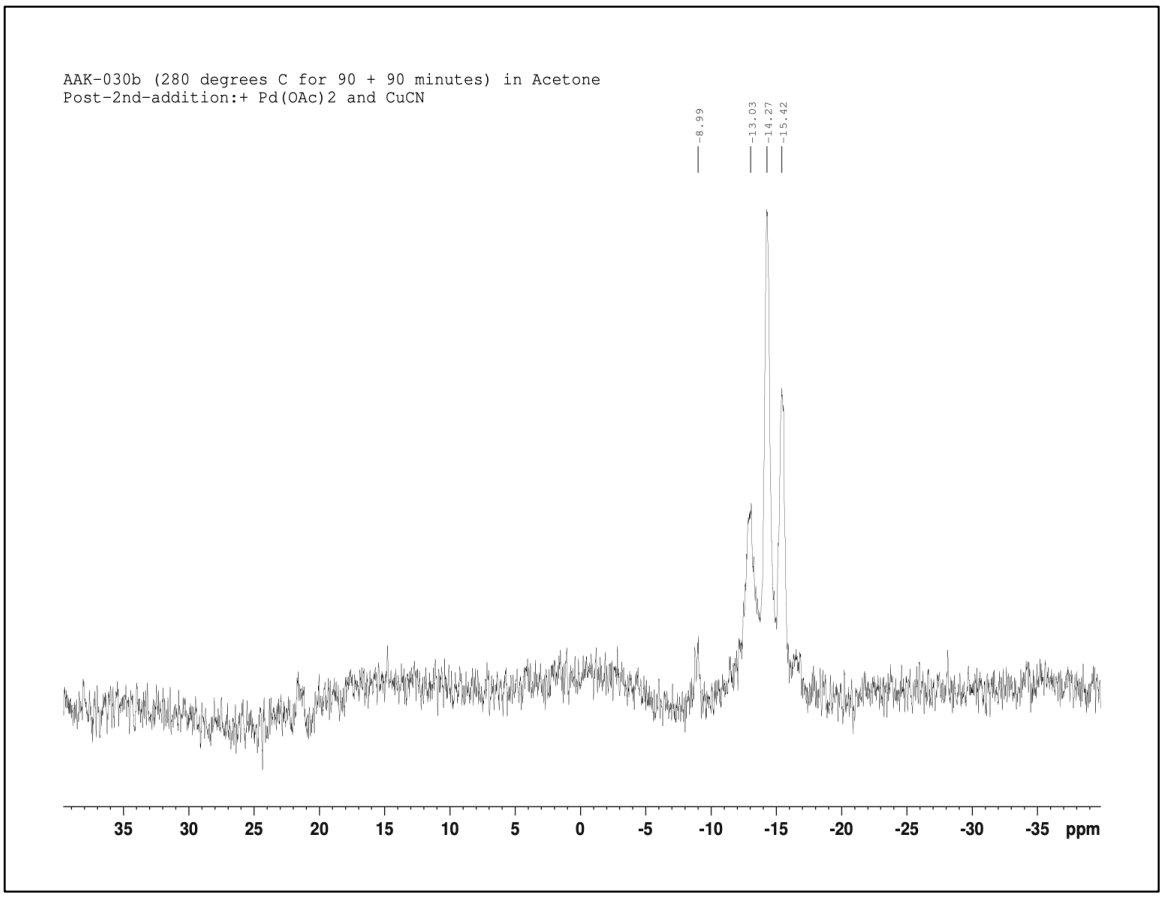

Figure A24. ^{11}B NMR spectrum in acetone of the hexacyanation of $Cs[CB_{11}H_6I_6]$ after two rounds of heating at 280 ˚C under MWI with an intermediate filtration and second addition of CuCN and $Pd(OAc)_2$.

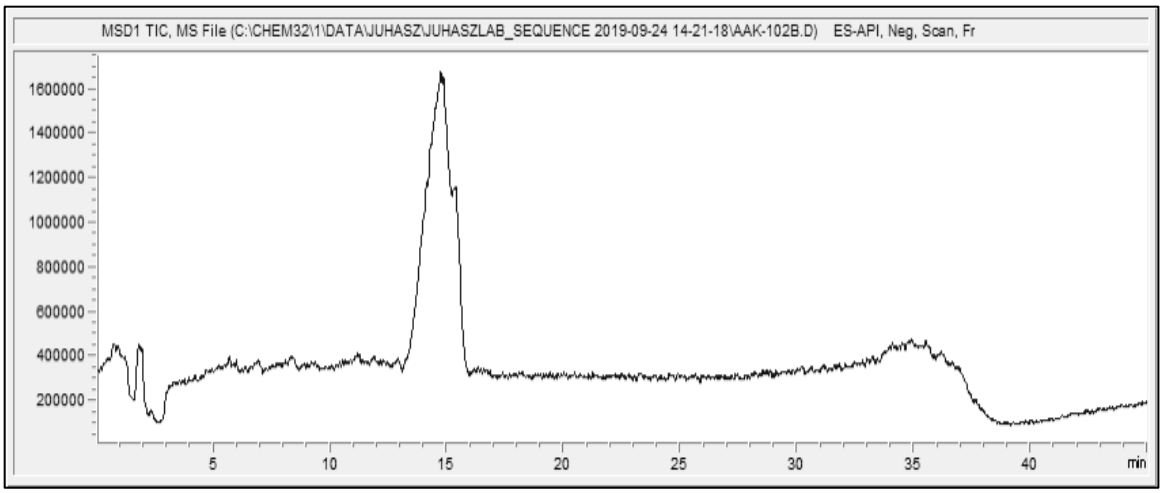

Figure A25. LC-MS negative ion chromatogram (range: *m/z* = 70-2000) showing a mixture of $[CB_{11}H_6(CN)_6]^-$ and $[CB_{11}H_6I(CN)_5]^-$ after heating with CuCN (*first addition*: 7.7 eq.; *second*: 13.2 eq.) and $Pd(OAc)_2$ (22 mol%; 56 mol%) in DMF for 9 hr (4 hr; 5 hr) at 280 ˚C under MWI. This chromatogram actually shows two overlapping peaks where $[CB_{11}H_6(CN)_6]^-$ begins elution slightly before $[CB_{11}H_6I(CN)_5]^-$; resolution of these peaks may be possible with a modified solvent gradient.

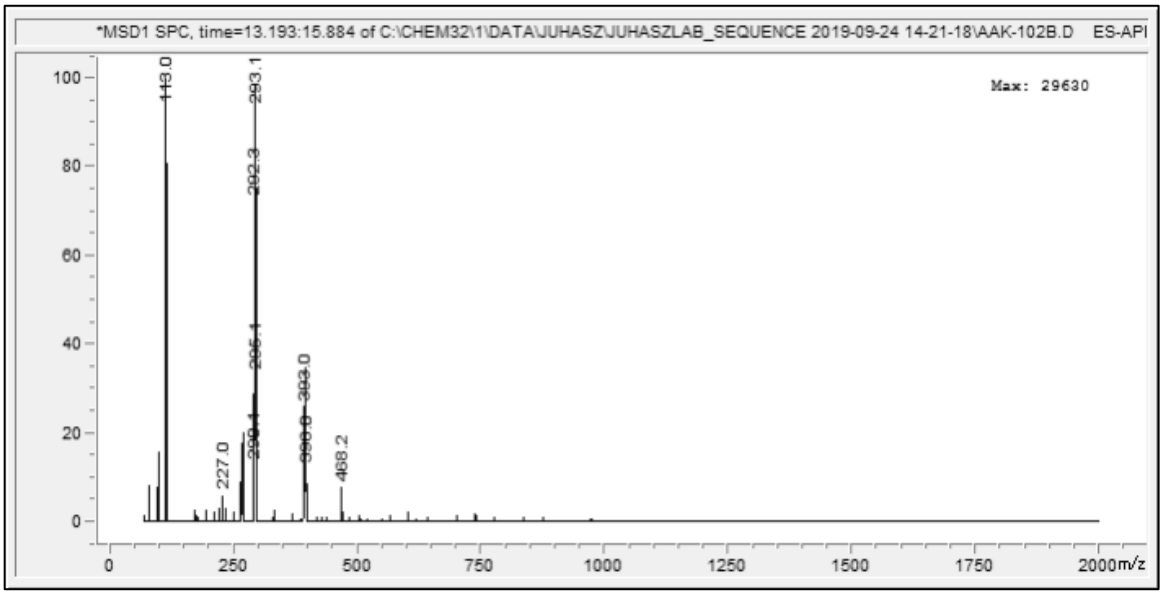

Figure A26. LC-MS negative ion mass spectrum corresponding to Figure A25 from 13.2 min until 15.9 min. The peak at *m/z* = 293.1 corresponds to $[CB_{11}H_6(CN)_6]^-$ (calc'd *m/z* = 293.1) and the peak at *m/z* = 393.0 corresponds to $[CB_{11}H_6(CN)_5I]^-$ (calc'd *m/z* = 394.0). The peak at *m/z* = 113.0 is trifluoroacetate carry-over from a previous user's solvent system.

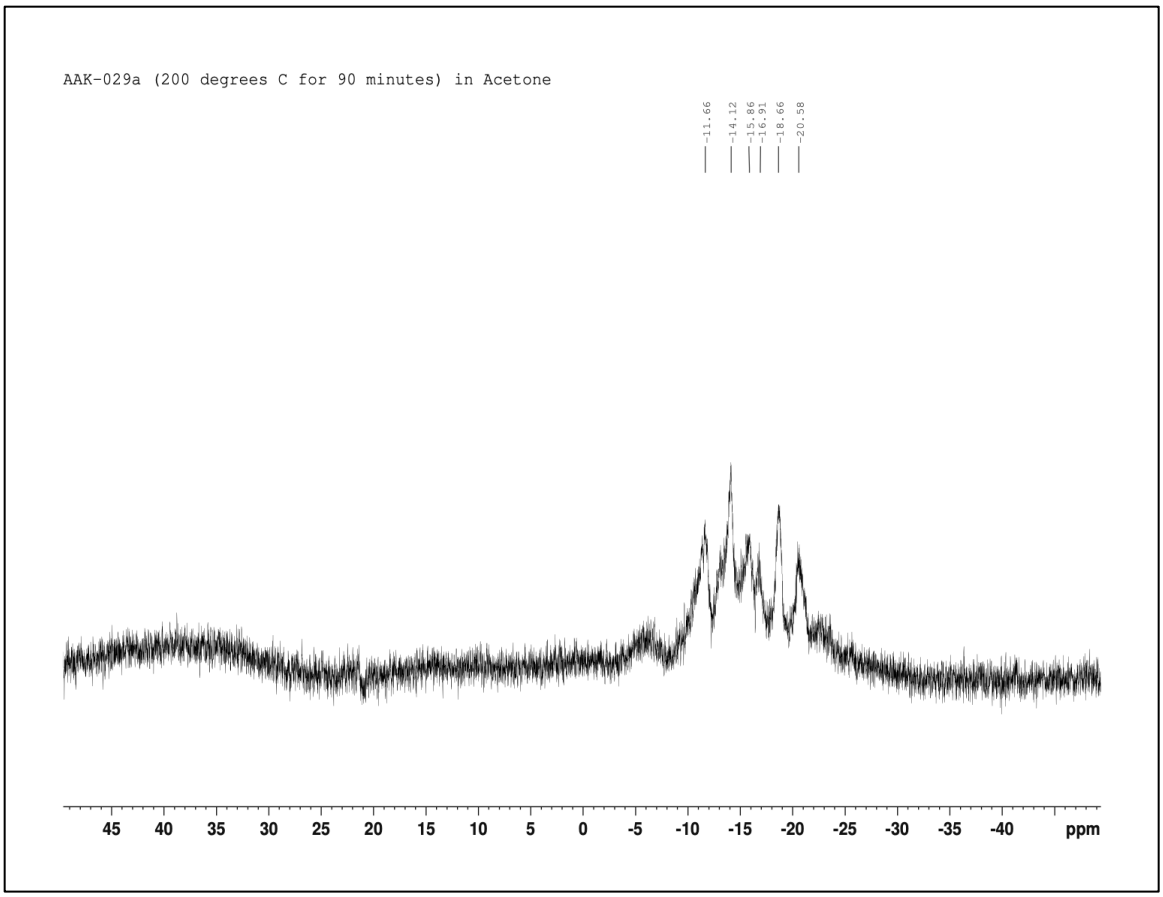

Figure A27. ^{11}B NMR spectrum in acetone showing the partial cyanation of $[Et_4N][CHB_{11}I_{11}]$ after heating with CuCN and $Pd_2(dba)_3$ in DMF for 90 min at 200 ˚C under MWI.

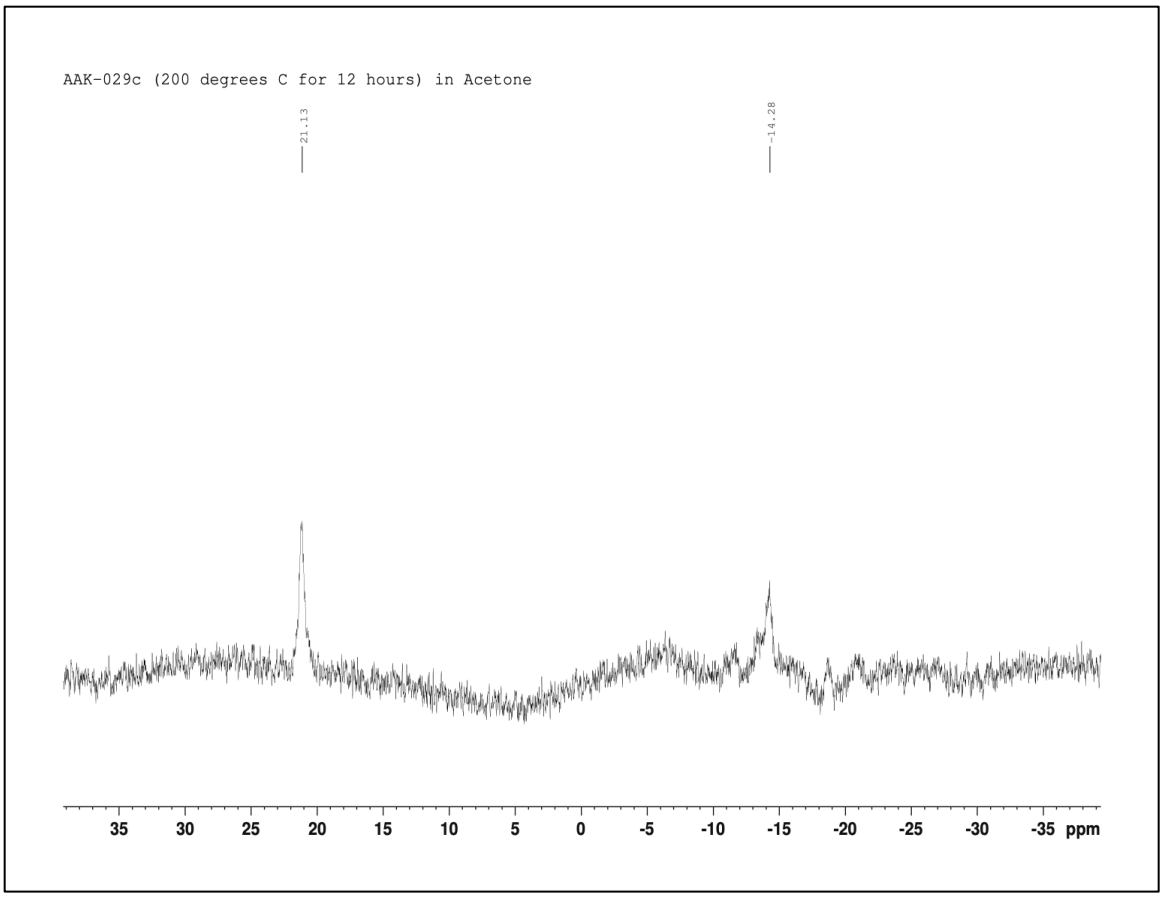

Figure A28. ^{11}B NMR spectrum in acetone showing $[Et_4N][CHB_{11}I_{11}]$ after heating with CuCN and $Pd_2(dba)_3$ in DMF for 12 hr at 200 ˚C under MWI.

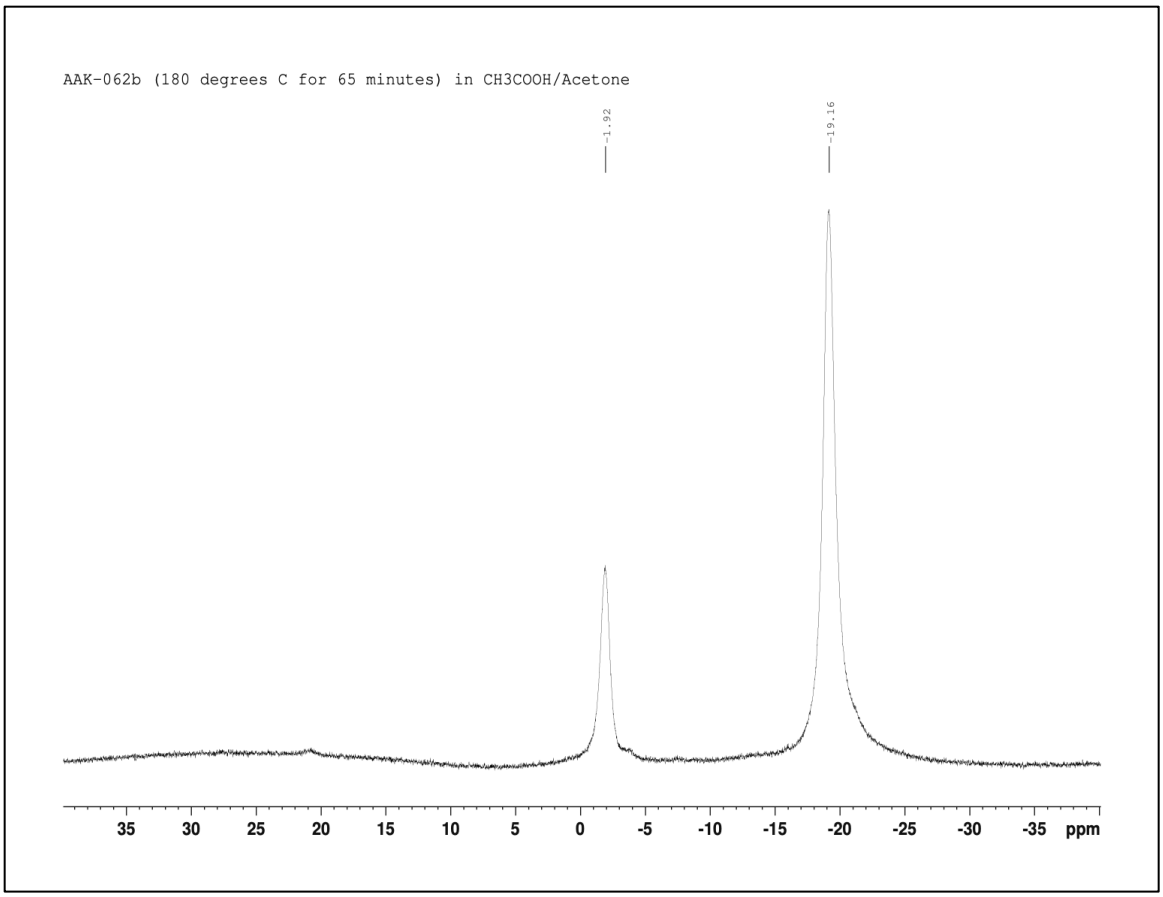

Figure A29. ^{11}B NMR spectrum of $[Et_4N]_2[B_{10}I_{10}]$ in acetic acid and acetone.

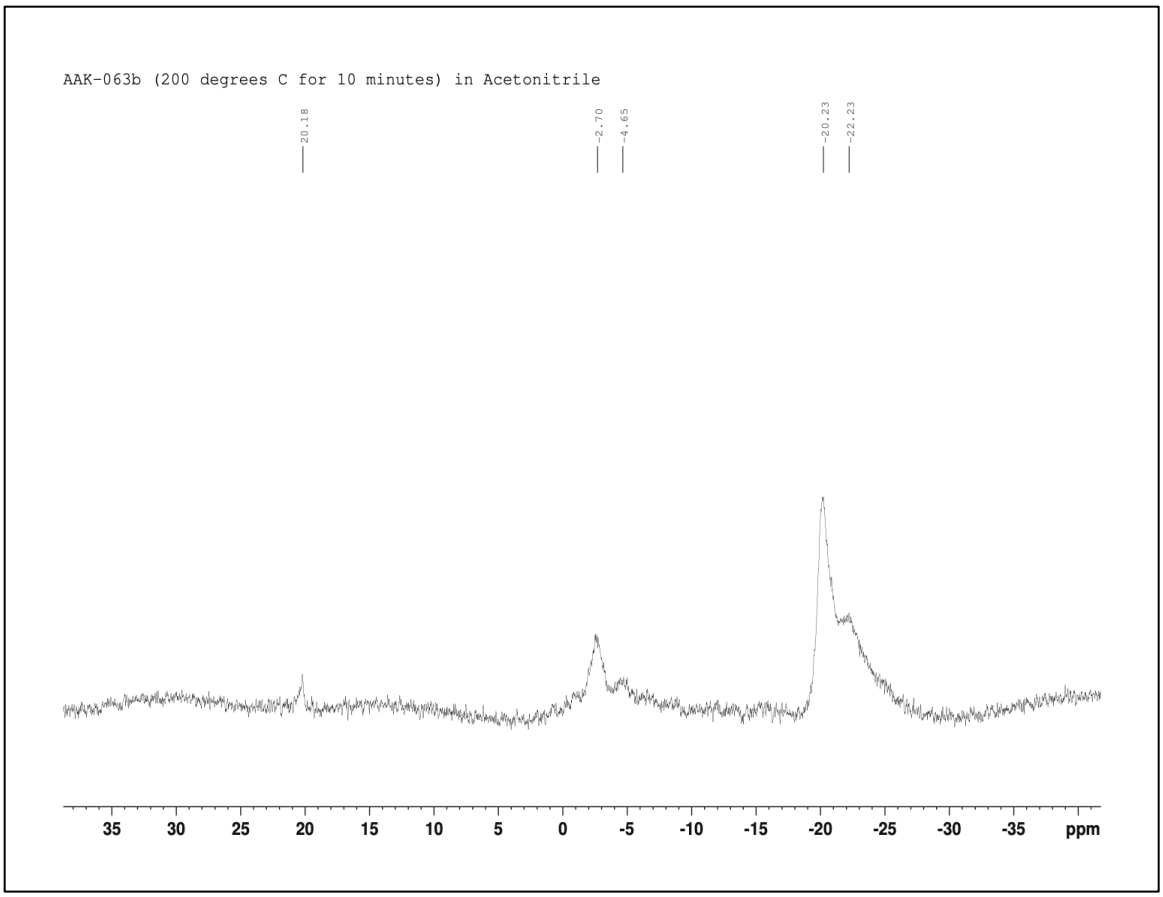

Figure A30. ^{11}B NMR spectrum in acetone of the partial cyanation of $[Et_4N]_2[B_{10}I_{10}]$ after 10 minutes of heating with CuCN and $Pd(OAc)_2$ at 200 ˚C under MWI.

7.2 X-Ray Diffraction Data

Crystal Structure Determination of $[Et_4N]_2[B_{12}(CN)_{12}]$:

Crystal Data for $C_{28}H_{40}B_{12}N_{14}$ (M =702.46 g/mol): trigonal, space group P-3 (no. 147), a = 20.87937(17) Å, c = 7.83528(8) Å, V = 2958.15(6) Å^3, Z = 3, T = 100.3(4) K, μ(CuKα) = 0.554 mm^{-1}, *Dcalc* = 1.183 g/cm^3, 36416 reflections measured (4.888° ≤ 2Θ ≤ 150.358°), 4054 unique (R_{int} = 0.0416, R_{sigma} = 0.0190) which were used in all calculations. The final R_1 was 0.0395 (I > 2σ(I)) and wR_2 was 0.1384 (all data).

Refinement Model Description:

Number of restraints - 0, number of constraints - unknown.
Details:
1. Fixed Uiso
   At 1.2 times of: all C(H,H) groups
   At 1.5 times of: all C(H,H,H) groups
2.a Secondary CH2 refined with riding coordinates: C9(H9A,H9B), C7(H7A,H7B), C13(H13A,H13B), C11(H11A,H11B)
2.b Idealized Me refined as rotating group: C8(H8A,H8B,H8C), C14(H14A,H14B,H14C), C10(H10A,H10B,H10C), C12(H12A,H12B,H12C)

Crystal Data and Structure Refinement for [AAK-101e]:

Identification code	exp_2227
Empirical formula	$C_{28}H_{40}B_{12}N_{14}$
Formula weight	702.46
Temperature/K	100.3(4)
Crystal system	trigonal
Space group	P-3
a/Å	20.87937(17)
b/Å	20.87937(17)
c/Å	7.83528(8)
α/°	90
β/°	90
γ/°	120
Volume/Å^3	2958.15(6)
Z	3
ρ_{calc}g/cm^3	1.183

μ/mm^{-1}	0.554
F(000)	1098.0
Crystal size/mm^3	0.1 × 0.16 × 0.18
Radiation	CuKα (λ = 1.54184)
2Θ range for data collection/°	4.888 to 150.358
Index ranges	$-25 \leq h \leq 25$, $-25 \leq k \leq 25$, $-9 \leq l \leq 9$
Reflections collected	36416
Independent reflections	4054 [R_{int} = 0.0416, R_{sigma} = 0.0190]
Data/restraints/parameters	4054/0/248
Goodness-of-fit on F^2	1.125
Final R indexes [$I \geq 2\sigma(I)$]	R_1 = 0.0395, wR_2 = 0.1322
Final R indexes [all data]	R_1 = 0.0454, wR_2 = 0.1384
Largest diff. peak/hole / e $Å^{-3}$	0.25/-0.26

Fractional Atomic Coordinates (× 10^4) and Equivalent Isotropic Displacement Parameters ($Å^2$ × 10^3) for [AAK-101e]. U_{eq} is defined as $^1/_3$ of the trace of the orthogonalized U_{IJ} tensor.

Atom	*x*	*y*	*z*	U(eq)
N2	2469.8(6)	4311.8(6)	3430.8(15)	36.0(3)
N4	1791.8(6)	5697.9(6)	148.0(13)	33.1(3)
C3	2895.1(6)	5501.0(6)	7583.3(14)	25.8(2)
C6	2219.7(6)	5964.4(6)	1210.7(14)	24.8(2)
N7	985.8(6)	5153.5(7)	5322.0(15)	36.7(3)
N3	2698.3(6)	5008.8(6)	8494.3(14)	34.3(3)
C5	1586.3(7)	5553.6(6)	5157.8(14)	26.6(3)
B1	2996.7(7)	5756.6(7)	4028.3(15)	21.9(2)
B4	3123.5(6)	6098.9(7)	6183.5(15)	22.1(3)
C4	2688.6(6)	4923.3(6)	3677.0(14)	25.6(2)
B2	2423.3(7)	6092.8(7)	4849.0(15)	22.2(2)
B3	2770.0(6)	6312.1(7)	2703.8(15)	21.5(3)
N5	1216.6(6)	1524.1(6)	813.7(13)	29.4(2)
C1	855.2(6)	1092.0(6)	1812.5(14)	23.6(2)
N6	-542.0(6)	1735.4(6)	3962.4(15)	35.2(3)
C2	-399.4(6)	1289.0(6)	4226.6(14)	25.1(2)
B6	419.9(7)	546.9(7)	3264.2(15)	22.0(2)
B5	-206.2(6)	674.4(7)	4590.2(15)	21.5(2)
N1	6773.0(5)	229.8(5)	446.5(13)	28.1(2)

C9	7295.1(7)	940.8(6)	-488.0(16)	31.1(3)
C7	7140.5(7)	130.9(7)	2016.3(17)	34.7(3)
C13	6102.4(7)	290.7(7)	936.1(16)	30.4(3)
C8	7409.2(8)	751.4(9)	3311.5(18)	43.3(3)
C14	5509.6(7)	-361.5(7)	1905.6(19)	38.6(3)
C10	8027.8(8)	1012.7(8)	-1006(2)	41.1(3)
C11	6555.1(8)	-443.4(7)	-684.2(18)	36.4(3)
C12	6166.3(9)	-464.7(8)	-2327(2)	47.2(4)

Anisotropic Displacement Parameters ($Å^2 \times 10^3$) for [AAK-101e]. The anisotropic displacement factor exponent takes the form: $-2\pi^2[h^2a^{*2}U_{11}+2hka^*b^*U_{12}+\ldots]$.

Atom	U_{11}	U_{22}	U_{33}	U_{23}	U_{13}	U_{12}
N2	33.7(6)	24.2(5)	47.5(6)	-2.0(4)	-2.1(4)	12.6(4)
N4	28.4(5)	32.7(5)	35.3(5)	-5.5(4)	-4.6(4)	13.1(4)
C3	23.2(5)	23.9(5)	30.3(5)	-0.3(4)	0.6(4)	11.8(4)
C6	22.2(5)	21.4(5)	30.5(5)	0.2(4)	1.5(4)	10.8(4)
N7	26.1(6)	38.9(6)	44.7(6)	7.5(5)	0.2(4)	16.0(5)
N3	37.1(6)	30.4(5)	35.7(5)	6.3(4)	4.5(4)	17.0(5)
C5	29.6(6)	22.9(5)	29.8(5)	2.9(4)	0.6(4)	14.9(5)
B1	19.0(6)	19.2(5)	27.7(5)	0.1(4)	-0.1(4)	9.6(5)
B4	18.5(5)	18.8(5)	28.6(5)	0.9(4)	0.4(4)	9.1(5)
C4	21.3(5)	24.5(6)	31.6(5)	0.1(4)	-0.2(4)	11.8(4)
B2	20.4(5)	20.2(6)	26.9(5)	0.0(4)	0.6(4)	10.8(5)
B3	18.7(5)	18.5(5)	27.5(5)	0.1(4)	0.4(4)	9.4(4)
N5	26.9(5)	27.2(5)	33.8(5)	2.4(4)	2.2(4)	13.3(4)
C1	20.3(5)	22.2(5)	29.3(5)	-1.8(4)	-1.1(4)	11.4(4)
N6	33.6(6)	30.4(5)	45.5(6)	2.0(4)	1.6(4)	18.9(5)
C2	21.1(5)	22.3(5)	29.5(5)	1.1(4)	0.7(4)	9.2(4)
B6	18.6(5)	18.7(5)	28.4(5)	0.0(4)	-0.6(4)	9.2(4)
B5	18.9(5)	18.9(5)	27.3(5)	0.1(4)	0.4(4)	9.8(5)
N1	24.5(5)	20.8(5)	41.1(5)	2.8(4)	3.0(4)	12.9(4)
C9	29.5(6)	20.8(5)	42.3(6)	3.7(4)	1.8(5)	12.1(5)
C7	28.7(6)	34.9(6)	46.9(7)	9.8(5)	4.1(5)	20.8(5)
C13	25.0(6)	28.5(6)	42.5(6)	-1.4(5)	-0.6(5)	16.9(5)
C8	36.7(7)	50.8(8)	46.6(7)	0.9(6)	-6.3(6)	25.1(7)
C14	25.0(6)	32.5(7)	56.0(8)	-1.6(6)	5.8(5)	12.7(5)
C10	33.3(7)	30.5(7)	59.4(8)	10.2(6)	13.3(6)	15.8(6)

C11	34.6(7)	21.1(6)	53.3(7)	-0.8(5)	8.7(6)	13.9(5)
C12	49.5(8)	34.3(7)	51.7(8)	-11.0(6)	-1.0(7)	16.4(6)

Bond Lengths for [AAK-101e]:

Atom	Atom	Length/Å	Atom	Atom	Length/Å
N2	C4	1.1369(16)	N5	C1	1.1467(15)
N4	C6	1.1420(16)	C1	B6	1.5430(16)
C3	N3	1.1456(16)	N6	C2	1.1303(16)
C3	B4	1.5470(16)	C2	B5	1.5519(16)
C6	B3	1.5432(16)	B6	B6[3]	1.793(2)
N7	C5	1.1131(17)	B6	B6[4]	1.793(2)
C5	B2	1.5534(17)	B6	B5[3]	1.7874(17)
B1	B4	1.8009(17)	B6	B5	1.7909(17)
B1	C4	1.5484(16)	B6	B5[5]	1.7955(17)
B1	B2[1]	1.7848(17)	B5	B5[5]	1.7852(14)
B1	B2	1.7832(17)	B5	B5[6]	1.7851(14)
B1	B3[1]	1.7863(17)	N1	C9	1.5198(15)
B1	B3	1.7876(17)	N1	C7	1.5176(16)
B4	B4[1]	1.798(2)	N1	C13	1.5172(14)
B4	B4[2]	1.798(2)	N1	C11	1.5259(16)
B4	B2	1.7922(17)	C9	C10	1.5157(18)
B4	B2[1]	1.7926(17)	C7	C8	1.515(2)
B2	B3	1.7965(16)	C13	C14	1.5093(18)
B3	B3[1]	1.784(2)	C11	C12	1.511(2)
B3	B3[2]	1.784(2)			

[1]1-Y,1+X-Y,+Z; [2]+Y-X,1-X,+Z; [3]+Y-X,-X,+Z; [4]-Y,+X-Y,+Z; [5]+Y,-X+Y,1-Z; [6]-Y+X,+X,1-Z

Bond Angles for [AAK-101e]:

Atom	Atom	Atom	Angle/°	Atom	Atom	Atom	Angle/°
N3	C3	B4	173.34(12)	C6	B3	B3[2]	124.45(7)
N4	C6	B3	177.49(12)	B1[2]	B3	B1	107.51(10)
N7	C5	B2	177.28(13)	B1	B3	B2	59.67(6)
C4	B1	B4	120.58(9)	B1[2]	B3	B2	59.76(6)
C4	B1	B2[1]	121.54(9)	B3[2]	B3	B1[2]	60.09(8)
C4	B1	B2	121.53(9)	B3[2]	B3	B1	107.87(7)
C4	B1	B3[1]	121.96(9)	B3[1]	B3	B1[2]	107.93(7)

C4	B1	B3	122.00(9)	B3[1]	B3	B1	60.02(7)
B2	B1	B4	60.00(7)	B3[2]	B3	B2	107.84(6)
B2[1]	B1	B4	59.99(7)	B3[1]	B3	B2	107.76(6)
B2	B1	B2[1]	107.76(10)	B3[1]	B3	B3[2]	60.0
B2[1]	B1	B3[1]	60.41(7)	N5	C1	B6	175.29(12)
B2	B1	B3[1]	108.25(8)	N6	C2	B5	179.82(13)
B2	B1	B3	60.41(7)	C1	B6	B6[3]	125.03(7)
B2[1]	B1	B3	108.19(8)	C1	B6	B6[4]	126.57(7)
B3	B1	B4	108.72(8)	C1	B6	B5	121.50(9)
B3[1]	B1	B4	108.74(8)	C1	B6	B5[5]	116.94(9)
B3[1]	B1	B3	59.89(8)	C1	B6	B5[3]	119.10(9)
C3	B4	B1	114.81(9)	B6[4]	B6	B6[3]	60.0
C3	B4	B4[2]	127.28(8)	B6[4]	B6	B5[5]	107.65(6)
C3	B4	B4[1]	128.00(8)	B6[3]	B6	B5[5]	107.76(6)
C3	B4	B2	119.12(9)	B5	B6	B6[3]	107.70(7)
C3	B4	B2[1]	120.18(9)	B5[3]	B6	B6[3]	60.03(7)
B4[2]	B4	B1	107.51(6)	B5[3]	B6	B6[4]	107.84(7)
B4[1]	B4	B1	107.53(6)	B5	B6	B6[4]	59.84(8)
B4[1]	B4	B4[2]	60.0	B5	B6	B5[5]	59.70(5)
B2[1]	B4	B1	59.56(7)	B5[3]	B6	B5[5]	59.76(5)
B2	B4	B1	59.51(6)	B5[3]	B6	B5	107.45(10)
B2	B4	B4[1]	107.61(7)	C2	B5	B6[6]	121.14(9)
B2[1]	B4	B4[1]	59.88(7)	C2	B5	B6	121.82(9)
B2	B4	B4[2]	59.90(8)	C2	B5	B6[4]	121.40(9)
B2[1]	B4	B4[2]	107.59(7)	C2	B5	B5[6]	121.36(9)
B2	B4	B2[1]	107.03(10)	C2	B5	B5[5]	121.93(9)
N2	C4	B1	179.11(13)	B6[4]	B5	B6[6]	108.64(9)
C5	B2	B1	120.30(9)	B6	B5	B6[6]	108.49(9)
C5	B2	B1[2]	121.94(9)	B6[4]	B5	B6	60.13(8)
C5	B2	B4[2]	123.20(9)	B5[6]	B5	B6[4]	60.34(6)
C5	B2	B4	122.17(9)	B5[6]	B5	B6[6]	60.02(7)
C5	B2	B3	119.63(9)	B5[6]	B5	B6	108.30(6)
B1	B2	B1[2]	107.77(10)	B5[5]	B5	B6	60.28(6)
B1	B2	B4[2]	108.53(8)	B5[5]	B5	B6[6]	59.90(7)
B1[2]	B2	B4[2]	60.45(7)	B5[5]	B5	B6[4]	108.34(6)
B1[2]	B2	B4	108.50(8)	B5[6]	B5	B5[5]	107.81(7)
B1	B2	B4	60.49(7)	C9	N1	C11	110.98(9)

B1	B2	B3	59.92(7)	C7	N1	C9	111.03(9)
B1[2]	B2	B3	59.84(7)	C7	N1	C11	106.46(9)
B4	B2	B4[2]	60.22(8)	C13	N1	C9	106.34(9)
B4	B2	B3	108.71(8)	C13	N1	C7	110.92(9)
B4[2]	B2	B3	108.65(8)	C13	N1	C11	111.19(9)
C6	B3	B1	120.75(9)	C10	C9	N1	114.92(10)
C6	B3	B1[2]	120.91(9)	C8	C7	N1	115.00(10)
C6	B3	B2	118.63(9)	C14	C13	N1	115.25(10)
C6	B3	B3[1]	124.33(7)	C12	C11	N1	115.48(11)

[1]1-Y,1+X-Y,+Z; [2]+Y-X,1-X,+Z; [3]+Y-X,-X,+Z; [4]-Y,+X-Y,+Z; [5]+Y,-X+Y,1-Z; [6]-Y+X,+X,1-Z

Torsion Angles for [AAK-101e]:

A	B	C	D	Angle/°	A	B	C	D	Angle/°
C3	B4	B2	C5	5.93(15)	B2[2]	B1	B2	B4[1]	-0.03(12)
C3	B4	B2	B1[1]	156.34(9)	B2[2]	B1	B2	B4	-37.68(8)
C3	B4	B2	B1	-103.27(11)	B2[2]	B1	B2	B3	101.25(9)
C3	B4	B2	B4[1]	118.59(11)	B2[2]	B1	B3	C6	152.15(9)
C3	B4	B2	B3	-140.15(10)	B2	B1	B3	C6	-107.33(11)
C5	B2	B3	C6	0.88(15)	B2	B1	B3	B1[1]	37.21(7)
C5	B2	B3	B1[1]	111.93(11)	B2[2]	B1	B3	B1[1]	-63.32(9)
C5	B2	B3	B1	-109.95(11)	B2[2]	B1	B3	B2	-100.53(10)
C5	B2	B3	B3[2]	-147.27(10)	B2	B1	B3	B3[1]	100.62(8)
C5	B2	B3	B3[1]	149.37(10)	B2	B1	B3	B3[2]	138.20(8)
B1	B4	B2	C5	109.20(11)	B2[2]	B1	B3	B3[2]	37.67(7)
B1	B4	B2	B1[1]	-100.39(10)	B2[2]	B1	B3	B3[1]	0.09(10)
B1	B4	B2	B4[1]	-138.14(8)	B2[2]	B4	B2	C5	146.51(11)
B1	B4	B2	B3	-36.88(8)	B2[2]	B4	B2	B1[1]	-63.08(9)
B1[1]	B2	B3	C6	-111.05(11)	B2[2]	B4	B2	B1	37.31(7)
B1	B2	B3	C6	110.83(11)	B2[2]	B4	B2	B4[1]	-100.82(7)
B1[1]	B2	B3	B1	138.12(9)	B2[2]	B4	B2	B3	0.43(10)
B1	B2	B3	B1[1]	-138.12(9)	B3[2]	B1	B4	C3	-148.81(9)
B1[1]	B2	B3	B3[1]	37.45(9)	B3	B1	B4	C3	147.58(9)
B1	B2	B3	B3[2]	-37.32(9)	B3[2]	B1	B4	B4[1]	63.46(12)
B1	B2	B3	B3[1]	-100.67(9)	B3	B1	B4	B4[1]	-0.16(12)
B1[1]	B2	B3	B3[2]	100.80(9)	B3[2]	B1	B4	B4[2]	0.22(12)
B4	B1	B2	C5	-112.21(11)	B3	B1	B4	B4[2]	-63.40(11)

B4	B1	B2	B1[1]	101.62(9)
B4	B1	B2	B4[1]	37.65(8)
B4	B1	B2	B3	138.93(9)
B4	B1	B3	C6	-144.25(10)
B4	B1	B3	B1[1]	0.29(10)
B4	B1	B3	B2	-36.92(8)
B4	B1	B3	B3[2]	101.28(9)
B4	B1	B3	B3[1]	63.70(9)
B4[1]	B4	B2	C5	-112.66(11)
B4[2]	B4	B2	C5	-150.45(9)
B4[1]	B4	B2	B1	138.14(8)
B4[2]	B4	B2	B1	100.35(8)
B4[2]	B4	B2	B1[1]	-0.04(10)
B4[1]	B4	B2	B1[1]	37.75(7)
B4[2]	B4	B2	B4[1]	-37.78(4)
B4[2]	B4	B2	B3	63.47(9)
B4[1]	B4	B2	B3	101.26(9)
B4	B2	B3	C6	147.96(9)
B4[1]	B2	B3	C6	-148.09(9)
B4[1]	B2	B3	B1	101.08(9)
B4	B2	B3	B1	37.13(8)
B4	B2	B3	B1[1]	-100.99(9)
B4[1]	B2	B3	B1[1]	-37.04(8)
B4	B2	B3	B3[1]	-63.54(11)
B4[1]	B2	B3	B3[1]	0.41(12)
B4[1]	B2	B3	B3[2]	63.76(11)
B4	B2	B3	B3[2]	-0.19(12)
C4	B1	B4	C3	-0.64(15)
C4	B1	B4	B4[2]	148.38(10)
C4	B1	B4	B4[1]	-148.38(10)
C4	B1	B4	B2	-111.12(11)
C4	B1	B4	B2[2]	111.12(11)
C4	B1	B2	C5	-2.64(15)
C4	B1	B2	B1[1]	-148.81(8)
C4	B1	B2	B4[1]	147.22(10)
C4	B1	B2	B4	109.57(11)
C4	B1	B2	B3	-111.50(11)
B3	B1	B4	B2	37.10(8)
B3[2]	B1	B4	B2[2]	-37.04(8)
B3[2]	B1	B4	B2	100.72(9)
B3	B1	B4	B2[2]	-100.66(9)
B3	B1	B2	C5	108.86(11)
B3[2]	B1	B2	C5	146.24(9)
B3	B1	B2	B1[1]	-37.31(8)
B3[2]	B1	B2	B1[1]	0.07(12)
B3	B1	B2	B4	-138.93(9)
B3[2]	B1	B2	B4[1]	-63.90(10)
B3[2]	B1	B2	B4	-101.55(9)
B3	B1	B2	B4[1]	-101.28(9)
B3[2]	B1	B2	B3	37.38(8)
B3[2]	B1	B3	C6	114.47(10)
B3[2]	B1	B3	B1[1]	-100.99(7)
B3[2]	B1	B3	B2	-138.20(8)
B3[2]	B1	B3	B3[1]	-37.58(4)
C1	B6	B5	C2	6.34(15)
C1	B6	B5	B6[3]	116.87(11)
C1	B6	B5	B6[4]	-141.79(8)
C1	B6	B5	B5[5]	-104.91(10)
C1	B6	B5	B5[4]	154.59(10)
B6[6]	B6	B5	C2	-148.12(9)
B6[3]	B6	B5	C2	-110.53(11)
B6[3]	B6	B5	B6[4]	101.34(11)
B6[6]	B6	B5	B6[3]	-37.59(4)
B6[6]	B6	B5	B6[4]	63.75(11)
B6[6]	B6	B5	B5[5]	100.63(7)
B6[6]	B6	B5	B5[4]	0.13(11)
B6[3]	B6	B5	B5[4]	37.72(8)
B6[3]	B6	B5	B5[5]	138.22(7)
B5[6]	B6	B5	C2	148.58(11)
B5[5]	B6	B5	C2	111.25(11)
B5[6]	B6	B5	B6[3]	-100.88(7)
B5[5]	B6	B5	B6[3]	-138.22(7)
B5[5]	B6	B5	B6[4]	-36.87(8)
B5[6]	B6	B5	B6[4]	0.46(11)

C4	B1	B3	C6	3.43(15)	B5^{6}	B6	B5	B5^{4}	-63.16(11)
C4	B1	B3	B1^{1}	147.96(11)	B5^{6}	B6	B5	B5^{5}	37.33(4)
C4	B1	B3	B2	110.75(11)	B5^{5}	B6	B5	B5^{4}	-100.49(10)
C4	B1	B3	B3^{2}	-111.05(11)	C9	N1	C7	C8	58.48(14)
C4	B1	B3	B3^{1}	-148.63(9)	C9	N1	C13	C14	-179.38(11)
B2	B1	B4	C3	110.48(10)	C9	N1	C11	C12	-59.85(15)
B2^{2}	B1	B4	C3	-111.76(10)	C7	N1	C9	C10	55.89(14)
B2^{2}	B1	B4	B4^{1}	100.50(9)	C7	N1	C13	C14	-58.56(14)
B2^{2}	B1	B4	B4^{2}	37.26(9)	C7	N1	C11	C12	179.22(11)
B2	B1	B4	B4^{1}	-37.26(9)	C13	N1	C9	C10	176.65(11)
B2	B1	B4	B4^{2}	-100.50(9)	C13	N1	C7	C8	-59.53(14)
B2	B1	B4	B2^{2}	-137.76(9)	C13	N1	C11	C12	58.30(14)
B2^{2}	B1	B4	B2	137.76(9)	C11	N1	C9	C10	-62.30(14)
B2^{2}	B1	B2	C5	-149.89(8)	C11	N1	C7	C8	179.38(11)
B2^{2}	B1	B2	B1^{1}	63.94(12)	C11	N1	C13	C14	59.70(14)

^{1}+Y-X,1-X,+Z; ^{2}1-Y,1+X-Y,+Z; ^{3}-Y,+X-Y,+Z; ^{4}-Y+X,+X,1-Z; ^{5}+Y,-X+Y,1-Z; ^{6}+Y-X,-X,+Z

Hydrogen Atom Coordinates (Å × 10^{4}) and Isotropic Displacement Parameters (Å^{2} × 10^{3}) for [AAK-101e]:

Atom	***x***	***y***	***z***	**U(eq)**
H9A	7048.49	973.43	-1505.72	37
H9B	7392.76	1356.11	238.58	37
H7A	6791.57	-328.01	2572.83	42
H7B	7558.69	83.17	1651.66	42
H13A	6266.8	731.31	1626.53	37
H13B	5885.25	356.08	-96.71	37
H8A	7766.71	1207.39	2787.33	65
H8B	7632.93	644.51	4257.34	65
H8C	6998.12	795.45	3710.18	65
H14A	5328.39	-799.66	1221.22	58
H14B	5110.25	-274.12	2164.58	58
H14C	5712.95	-425.47	2947.65	58
H10A	7939.29	595.46	-1692.38	62
H10B	8299.38	1029.01	-2.34	62
H10C	8308.65	1459.23	-1650.53	62
H11A	6998.42	-461.39	-963.38	44

H11B	6234.77	-884.74	-32.28	44
H12A	6081.58	-887.98	-2984.85	71
H12B	6468.89	-22.61	-2970.19	71
H12C	5701.48	-496.84	-2071.02	71

Crystal Structure Determination of $(CH_3CN)_3Cu[\mu\text{-}B_{12}(CN)_{12}]$

$Cu(CH_3CN)_3$:

Crystal Data for $C_{24}H_{18}B_{12}Cu_2N_{18}$ (M =815.51 g/mol): triclinic, space group P-1 (no. 2), a = 9.7190(5) Å, b = 10.0684(4) Å, c = 10.8171(3) Å, α = 101.043(3)°, β = 94.300(3)°, γ = 98.888(4)°, V = 1020.44(8) Å^3, Z = 1, T = 100.3(4) K, μ(Cu Kα) = 1.639 mm^{-1}, *Dcalc* = 1.3267 g/cm^3, 29919 reflections measured (8.38° ≤ 2Θ ≤ 150.76°), 4166 unique (R_{int} = 0.0849, R_{sigma} = 0.0459) which were used in all calculations. The final R_1 was 0.0462 (I ≥ 2u(I)) and wR_2 was 0.1172 (all data).

Refinement Model Description:

Number of restraints - 0, number of constraints - 12.
Details:
1. Fixed Uiso
 At 1.5 times of: all C(H,H,H) groups
2.a Idealized Me refined as rotating group: C10(H10a,H10b,H10c), C9(H9a,H9b,H9c), C0aa(H0aa,H0ab,H0ac)

Crystal Data and Structure Refinement for [AAK-068i]:

Identification code	1956907
Empirical formula	$C_{24}H_{18}B_{12}Cu_2N_{18}$
Formula weight	815.51
Temperature/K	100.3(4)
Crystal system	triclinic
Space group	P-1
a/Å	9.7190(5)
b/Å	10.0684(4)
c/Å	10.8171(3)
α/°	101.043(3)
β/°	94.300(3)

γ/°	98.888(4)
Volume/Å^3	1020.44(8)
Z	1
ρ_{calc}g/cm^3	1.3267
μ/mm^{-1}	1.639
F(000)	403.1
Crystal size/mm^3	0.2 × 0.1 × 0.1
Radiation	Cu Kα (λ = 1.54184)
2Θ range for data collection/°	8.38 to 150.76
Index ranges	-11 ≤ h ≤ 11, -12 ≤ k ≤ 12, -13 ≤ l ≤ 13
Reflections collected	29919
Independent reflections	4166 [R_{int} = 0.0849, R_{sigma} = 0.0459]
Data/restraints/parameters	4166/0/256
Goodness-of-fit on F^2	1.057
Final R indexes [I ≥ 2σ (I)]	R_1 = 0.0462, wR_2 = 0.0994
Final R indexes [all data]	R_1 = 0.0695, wR_2 = 0.1172
Largest diff. peak/hole / e Å^{-3}	0.42/-0.62

Fractional Atomic Coordinates (× 10^4) and Equivalent Isotropic Displacement Parameters (Å^2 × 10^3) for [AAK-068i]. U_{eq} is defined as $^1/_3$ of the trace of the orthogonalized U_{IJ} tensor.

Atom	*x*	*y*	*z*	U(eq)
Cu1	3401.4(5)	843.4(4)	1981.2(4)	35.06(15)
C4	261(3)	7961(3)	4165(2)	26.1(6)
N1	2682(3)	2260(2)	3204(2)	32.4(5)
N3	4784(3)	27(2)	2895(2)	35.9(6)
N2	4379(3)	1767(3)	757(2)	39.9(6)
N6	320(3)	8948(3)	3820(2)	38.4(6)
C1	2063(3)	3003(3)	3768(2)	28.1(6)
C7	3135(3)	6498(3)	4687(3)	31.6(6)
N4	3289(3)	4377(3)	7735(2)	42.7(7)
N7	1730(3)	8632(3)	7963(2)	41.7(6)
C6	2473(3)	4563(3)	7004(3)	29.7(6)
N8	4211(3)	7023(3)	4538(3)	46.1(7)
C2	5073(4)	2344(3)	157(3)	38.1(7)
C3	790(3)	5138(3)	2159(3)	28.9(6)
C5	1320(3)	7674(3)	7207(3)	29.7(6)

B5	1322(4)	4788(3)	6039(3)	28.0(7)
B6	1109(3)	3965(3)	4403(3)	26.0(6)
N5	1130(3)	5221(3)	1198(2)	41.7(6)
B1	1659(3)	5786(3)	4858(3)	26.5(6)
B4	713(4)	6387(3)	6156(3)	27.8(7)
B3	147(4)	6559(3)	4589(3)	26.8(6)
B2	395(4)	5057(3)	3512(3)	27.0(7)
N9	1664(3)	-460(3)	1229(2)	36.8(6)
C8	5685(3)	-325(3)	3412(3)	32.8(6)
C10	5970(4)	3083(3)	-601(3)	42.1(8)
C9	6835(3)	-759(3)	4064(3)	41.5(8)
C11	574(4)	-1106(3)	938(3)	35.1(7)
C0aa	-820(4)	-1909(3)	580(3)	45.9(8)

Anisotropic Displacement Parameters ($Å^2 \times 10^3$) for [AAK-068i]. The Anisotropic displacement factor exponent takes the form: $-2\pi^2[h^2a^{*2}U_{11}+2hka^*b^*U_{12}+\ldots]$.

Atom	**U_{11}**	**U_{22}**	**U_{33}**	**U_{12}**	**U_{13}**	**U_{23}**
Cu1	32.8(3)	39.0(2)	36.6(2)	14.7(2)	6.65(19)	7.99(18)
C4	23.8(16)	32.8(14)	22.4(12)	9.8(12)	2.9(10)	3.3(10)
N1	27.3(15)	35.9(12)	35.8(12)	8.3(11)	3.5(11)	9.5(10)
N3	31.5(16)	36.4(13)	41.2(13)	10.2(11)	7.5(11)	6.4(11)
N2	37.3(17)	44.9(15)	38.9(14)	10.5(13)	6.5(12)	8.5(12)
N6	37.8(17)	41.9(14)	37.8(13)	10.0(12)	9.9(11)	8.9(11)
C1	25.2(16)	30.1(13)	29.4(13)	4.9(12)	1.1(11)	7.4(11)
C7	30.6(19)	34.3(14)	29.8(14)	7.7(13)	3.3(12)	4.4(11)
N4	36.9(17)	51.5(16)	40.1(14)	15.3(13)	-2.6(12)	7.0(12)
N7	46.1(18)	39.7(14)	34.9(13)	2.3(13)	5.2(12)	1.1(11)
C6	24.5(16)	31.4(14)	32.2(14)	4.3(12)	3.1(12)	4.2(11)
N8	33.7(18)	50.6(16)	51.3(16)	-0.9(14)	9.4(13)	8.3(13)
C2	36(2)	40.3(16)	38.0(16)	14.9(15)	1.5(14)	2.6(13)
C3	25.9(17)	28.9(13)	32.4(14)	5.4(12)	5.2(12)	6.0(11)
C5	28.1(17)	32.7(14)	29.9(13)	6.6(12)	4.9(12)	8.4(12)
B5	26.4(19)	30.3(15)	27.8(14)	6.4(13)	3.2(13)	5.7(12)
B6	19.7(17)	29.1(14)	28.9(14)	3.4(13)	3.6(12)	5.2(12)
N5	41.6(18)	49.3(15)	33.3(13)	4.1(13)	4.1(12)	9.0(11)
B1	23.2(18)	28.8(14)	27.5(14)	4.4(13)	4.9(12)	5.2(11)
B4	25.5(18)	30.0(15)	27.2(14)	5.1(13)	2.4(13)	4.5(12)

B3	26.6(18)	27.6(14)	26.9(14)	7.1(13)	4.5(12)	4.9(11)
B2	26.7(18)	30.6(15)	25.4(14)	8.7(13)	5.6(12)	5.5(11)
N9	41.1(18)	39.9(13)	31.8(12)	11.9(13)	7.9(12)	8.0(10)
C8	29.2(18)	31.4(14)	38.9(15)	6.1(13)	7.6(13)	7.5(12)
C10	35(2)	45.0(17)	45.6(17)	2.7(15)	11.9(15)	8.2(14)
C9	27.3(19)	45.4(17)	55.1(19)	7.0(14)	1.5(15)	19.4(15)
C11	38(2)	36.7(15)	32.1(14)	10.7(15)	4.8(13)	7.7(12)
C0aa	45(2)	43.4(17)	46.5(18)	5.8(16)	-4.2(15)	7.1(14)

Bond Lengths for [AAK-068i]:

Atom	Atom	Length/Å	Atom	Atom	Length/Å
Cu1	N1	2.000(2)	B5	B6	1.787(4)
Cu1	N3	1.977(3)	B5	B1	1.790(4)
Cu1	N2	1.977(3)	B5	B4	1.785(4)
Cu1	N9	1.984(3)	B5	B3[1]	1.801(5)
C4	N6	1.121(4)	B5	B2[1]	1.795(5)
C4	B3	1.557(4)	B6	B1	1.790(4)
N1	C1	1.145(4)	B6	B4[1]	1.787(5)
N3	C8	1.142(4)	B6	B3[1]	1.783(5)
N2	C2	1.141(4)	B6	B2	1.778(4)
C1	B6	1.545(4)	B1	B4	1.795(4)
C7	N8	1.135(4)	B1	B3	1.796(4)
C7	B1	1.541(5)	B1	B2	1.792(4)
N4	C6	1.140(4)	B4	B3	1.792(4)
N7	C5	1.135(4)	B4	B2[1]	1.783(5)
C6	B5	1.544(4)	B3	B2	1.784(4)
C2	C10	1.458(5)	N9	C11	1.141(4)
C3	N5	1.128(4)	C8	C9	1.446(4)
C3	B2	1.554(4)	C11	C0aa	1.450(5)
C5	B4	1.555(4)			

[1]-X,1-Y,1-Z

Bond Angles for [AAK-068i]:

Atom	Atom	Atom	Angle/°	Atom	Atom	Atom	Angle/°
N3	Cu1	N1	109.69(10)	B3	B1	B4	59.85(17)
N2	Cu1	N1	108.22(10)	B2	B1	C7	120.6(2)

N2	Cu1	N3	107.74(11)
N9	Cu1	N1	102.51(10)
N9	Cu1	N3	114.21(10)
N9	Cu1	N2	114.21(11)
B3	C4	N6	177.6(3)
C1	N1	Cu1	168.3(2)
C8	N3	Cu1	172.7(3)
C2	N2	Cu1	172.0(3)
B6	C1	N1	173.8(3)
B1	C7	N8	178.7(3)
B5	C6	N4	177.8(3)
C10	C2	N2	179.5(3)
B2	C3	N5	177.2(3)
B4	C5	N7	177.9(3)
B6	B5	C6	123.0(2)
B1	B5	C6	123.7(3)
B1	B5	B6	60.05(17)
B4	B5	C6	122.3(2)
B4	B5	B6	107.7(2)
B4	B5	B1	60.28(17)
$B3^1$	B5	C6	120.3(2)
$B3^1$	B5	B6	59.61(17)
$B3^1$	B5	B1	108.0(2)
$B3^1$	B5	B4	107.5(2)
$B2^1$	B5	C6	120.4(2)
$B2^1$	B5	B6	107.0(2)
$B2^1$	B5	B1	107.9(2)
$B2^1$	B5	B4	59.75(18)
$B2^1$	B5	$B3^1$	59.48(18)
B5	B6	C1	125.1(2)
B1	B6	C1	122.2(2)
B1	B6	B5	60.06(17)
$B4^1$	B6	C1	118.3(2)
$B4^1$	B6	B5	108.9(2)
$B4^1$	B6	B1	108.8(2)
$B3^1$	B6	C1	122.6(2)
$B3^1$	B6	B5	60.58(17)
B2	B1	B5	107.6(2)
B2	B1	B6	59.53(17)
B2	B1	B4	107.2(2)
B2	B1	B3	59.60(17)
B5	B4	C5	123.1(2)
$B6^1$	B4	C5	120.2(2)
$B6^1$	B4	B5	108.2(2)
B1	B4	C5	122.6(3)
B1	B4	B5	60.00(17)
B1	B4	$B6^1$	108.0(2)
B3	B4	C5	120.8(2)
B3	B4	B5	108.1(2)
B3	B4	$B6^1$	59.79(18)
B3	B4	B1	60.12(17)
$B2^1$	B4	C5	121.7(2)
$B2^1$	B4	B5	60.40(18)
$B2^1$	B4	$B6^1$	59.76(18)
$B2^1$	B4	B1	108.2(2)
$B2^1$	B4	B3	107.7(2)
$B5^1$	B3	C4	120.1(2)
$B6^1$	B3	C4	122.6(2)
$B6^1$	B3	$B5^1$	59.80(17)
B1	B3	C4	121.9(2)
B1	B3	$B5^1$	108.5(2)
B1	B3	$B6^1$	108.1(2)
B4	B3	C4	123.7(2)
B4	B3	$B5^1$	108.0(2)
B4	B3	$B6^1$	59.97(17)
B4	B3	B1	60.03(17)
B2	B3	C4	120.3(2)
B2	B3	$B5^1$	60.09(18)
B2	B3	$B6^1$	107.6(2)
B2	B3	B1	60.09(17)
B2	B3	B4	107.8(2)
$B5^1$	B2	C3	122.3(2)
B6	B2	C3	121.7(2)
B6	B2	$B5^1$	108.1(2)

B3[1]	B6	B1	108.7(2)	B1	B2	C3	119.8(2)
B3[1]	B6	B4[1]	60.24(18)	B1	B2	B5[1]	108.9(2)
B2	B6	C1	118.5(2)	B1	B2	B6	60.15(17)
B2	B6	B5	108.3(2)	B4[1]	B2	C3	122.8(2)
B2	B6	B1	60.32(17)	B4[1]	B2	B5[1]	59.85(18)
B2	B6	B4[1]	60.02(18)	B4[1]	B2	B6	60.22(17)
B2	B6	B3[1]	108.2(2)	B4[1]	B2	B1	108.8(2)
B5	B1	C7	123.4(2)	B3	B2	C3	120.7(2)
B6	B1	C7	122.3(2)	B3	B2	B5[1]	60.43(17)
B6	B1	B5	59.89(17)	B3	B2	B6	108.1(2)
B4	B1	C7	123.1(2)	B3	B2	B1	60.31(17)
B4	B1	B5	59.72(17)	B3	B2	B4[1]	108.3(2)
B4	B1	B6	107.1(2)	C11	N9	Cu1	169.8(2)
B3	B1	C7	121.0(2)	C9	C8	N3	179.4(3)
B3	B1	B5	107.7(2)	C0aa	C11	N9	179.1(3)
B3	B1	B6	107.1(2)				

[1]-X,1-Y,1-Z

Hydrogen Atom Coordinates (Å × 10^4) and Isotropic Displacement Parameters (Å^2 × 10^3) for [AAK-068i]:

Atom	***x***	***y***	***z***	**U(eq)**
H10a	5400(4)	3390(20)	-1215(15)	63.1(11)
H10b	6561(18)	3861(14)	-58(4)	63.1(11)
H10c	6541(18)	2483(8)	-1029(18)	63.1(11)
H9a	7684(6)	-490(20)	3706(15)	62.2(11)
H9b	6935(16)	-331(19)	4947(5)	62.2(11)
H9c	6651(12)	-1739(4)	3974(19)	62.2(11)
H0aa	-1081(11)	-1970(20)	-305(6)	68.8(12)
H0ab	-827(7)	-2813(9)	740(20)	68.8(12)
H0ac	-1474(5)	-1471(14)	1066(17)	68.8(12)

7.3 Optimized Geometries

Optimized Geometry for $[B_{12}(CN)_{12}]^{2-}$ (B3LYP/6-311+G(d,p)):

B	0.698393	0.063878	1.559143
C	1.337035	0.122841	2.957851
N	1.823836	0.160521	4.004260
B	-0.522978	1.262794	1.023833
C	-1.007942	2.407309	1.931005
N	-1.372154	3.266432	2.611175
B	-1.005399	-0.442835	1.309429
C	-1.916998	-0.841800	2.483020
N	-2.600885	-1.143823	3.363009
B	0.335497	-1.497861	0.749830
C	0.636310	-2.851268	1.417380
N	0.855241	-3.868813	1.917362
B	-1.112320	-1.264082	-0.284968
C	-2.120112	-2.396524	-0.548984
N	-2.882799	-3.240781	-0.745502
B	-1.643145	0.444120	-0.118402
C	-3.127004	0.839212	-0.218395
N	-4.240437	1.135822	-0.292484
B	-0.698389	-0.063872	-1.559138
C	-1.337047	-0.122840	-2.957838
N	-1.823837	-0.160545	-4.004251
B	0.522971	-1.262792	-1.023829
C	1.007959	-2.407296	-1.931000
N	1.372190	-3.266413	-2.611168
B	1.005396	0.442839	-1.309420
C	1.916998	0.841809	-2.483008
N	2.600887	1.143836	-3.362993
B	-0.335501	1.497864	-0.749824
C	-0.636324	2.851273	-1.417365
N	-0.855263	3.868821	-1.917339
B	1.112317	1.264087	0.284978
C	2.120123	2.396522	0.548966
N	2.882816	3.240777	0.745463
B	1.643139	-0.444119	0.118412
C	3.126997	-0.839224	0.218375
N	4.240424	-1.135861	0.292432

Optimized Geometry for $[B_{10}(SCN)_{10}]^{2-}$ (PBE0/def2-TZVP)**:**

B	-0.06370944083465	0.05845202046497	0.01286753252862
B	-1.00286522090261	-0.83575217720020	1.11394871186025
B	0.84816430005716	-0.87781479527684	1.10190059636984
B	0.89009583289817	0.97313359808044	1.08399977879015
B	-0.96088534120292	1.01523167184766	1.09620184879952
N	-1.90439082544837	1.99489958767334	0.61782836976135
N	1.87113856894993	1.90867229257393	0.59291107920289
N	1.78520536078692	-1.86646926656311	0.62932965132076
N	-1.99037646749743	-1.78019812254148	0.65391196747540
N	-0.07317491214795	0.04458054816320	-1.42018615014825
B	-0.01606699782434	1.39200659548054	2.62719294574835
B	1.26296163375359	0.05321566547156	2.63115172243112
N	2.62698237819271	0.02668015246039	3.09757487807277
B	-0.03854219370583	0.09343372535681	3.72587402239101
B	-1.35472640889765	0.11304092721659	2.64840703872108
B	-0.07570147678170	-1.22570553490520	2.65240482574686
N	-0.10352553678147	-2.58203492564051	3.14058766822723
N	-2.71230649435469	0.14845866265385	3.13268754973329
N	-0.02868719587334	0.10717852411704	5.15895009674667
N	0.01836278676977	2.75729314807084	3.08941174069996
C	-2.66983218876122	2.78624924711978	0.20463537972382
C	-0.12488029807303	-3.67994769787953	3.56129841132166
C	-0.02048290755669	0.11811519368040	6.33410725814169
C	0.04470148600697	3.86293290343112	3.48906513377982
C	2.66428351977623	2.66538500739068	0.16727985191652
C	-0.08050191724235	0.03332885901228	-2.59533653695195
C	-2.78919411942617	-2.54480943669481	0.25372654205052
C	-3.81180525894987	0.17054786524310	3.54920596439789
C	2.54146389794322	-2.66918799305766	0.22118703262102
C	3.73161399123053	0.00378932594954	3.50022927988966
S	3.73484743857304	3.68587917817143	-0.40755297639108
S	-0.09062816475082	0.01798838493905	-4.18454028515562
S	-3.86695402207312	-3.57609414292233	-0.28729807024872
S	-0.00957277131939	0.13286943425930	7.92330148393306
S	3.56190891129336	-3.75173605339254	-0.33059563381517
S	-3.70219258985713	3.85390812970283	-0.35391250559428
S	0.08041906016447	5.35425717461949	4.02975254640317

S	-0.15388333423465	-5.16082153874986	4.13040779886283
S	5.22166424439471	-0.02679656452644	4.04477070689353
S	-5.29498732629342	0.20107042620039	4.11230274374263

Optimized Geometry for $[B_{10}(CN)_{10}]^{2-}$ (PBE0/def2-TZVP):

B	-0.07683958955244	0.06236412408246	0.04730655767701
B	-1.01861382947573	-0.82528152002664	1.14601245215192
B	0.81880567106342	-0.86580053350687	1.15106419095843
B	0.85936985625485	0.97150504069648	1.13311492866423
B	-0.97800214403515	1.01204078903693	1.12800092960780
C	-1.97068825981483	2.04597682463853	0.57490543096899
C	1.90007819321884	1.96021335707495	0.58561419083625
C	1.81407657179859	-1.91049971027810	0.62341779524424
C	-2.05649799995132	-1.82465480782487	0.61270520163212
C	-0.07280937376199	0.04736227655354	-1.47633959051740
B	-0.05459290642920	1.38723721218125	2.64879848586526
B	1.21576759101052	0.05923151313715	2.66512990741546
C	2.65229595739481	0.03231836453632	3.20922226194528
B	-0.08625680278452	0.09881314237144	3.75373280837686
B	-1.38271568313476	0.11688396511268	2.65794297288837
B	-0.11234794474832	-1.21111201858817	2.67424070411006
C	-0.14592751869566	-2.64351665796025	3.22874290633385
C	-2.82199030290906	0.15431918044462	3.19409487636129
C	-0.09007344000878	0.11394327298202	5.27738308755753
C	-0.02397441674856	2.83033106893924	3.17503888236560
N	-2.71133748201548	2.81713995620737	0.14646225170093
N	-0.17203648650654	-3.71185061966581	3.65862618714089
N	-0.09290608358429	0.12605288337139	6.42965119823438
N	-0.00130421036972	3.90729181723589	3.58303649227396
N	2.67701261697458	2.69750193467406	0.16182636126641
N	-0.06926923617558	0.03641039679129	-2.62861655132918
N	-2.83065378969827	-2.57075838606685	0.19938914763775
N	-3.89625636325770	0.18201524130865	3.60882970091079
N	2.55657759568416	-2.69022209998418	0.21409722275769
N	3.72425981025812	0.01173399252548	3.63027900896309

Optimized Geometry for $[B_{10}(BO)_{10}]^{2-}$ (PBE0/def2-TZVP):

B	-0.07684312782684	0.06176476268899	0.03737020985293
B	-1.01880812413609	-0.82566600468754	1.15741615713821

B	0.81874919605547	-0.86617315645313	1.16263311576407
B	0.85929142695640	0.97128050454884	1.14457229676307
B	-0.97822828727250	1.01178864009716	1.13935622486324
B	-2.03732788969349	2.11531090012383	0.50701121026039
B	1.97012795022834	2.02633114885002	0.51828775634780
B	1.88161126898448	-1.98139923133394	0.55775405628573
B	-2.12684918296511	-1.89255325964989	0.54645241668652
B	-0.07248885125179	0.04538785618648	-1.60843700060685
B	-0.05483074890899	1.38688287796604	2.63716600457706
B	1.21568476207649	0.05878951496376	2.65361534452660
B	2.74880617289118	0.03107637529769	3.27658256638471
B	-0.08659624557457	0.09855565309214	3.76350760251304
B	-1.38300052311046	0.11639637281990	2.64621331846955
B	-0.11251064158507	-1.21168655288452	2.66265760325874
B	-0.14815218471408	-2.74025187873639	3.29630774470206
B	-2.91934515880719	0.15713714824916	3.26045293991898
B	-0.09097506713820	0.11480865945465	5.40931750211602
B	-0.02187689559968	2.92762030967697	3.24079519747890
O	-2.80355065575024	2.91578086959568	0.02515964160549
O	-0.17309714817699	-3.84764785643203	3.77910000914488
O	-0.09418938655588	0.12668693478893	6.61762124251328
O	0.00362989510825	4.04417342724623	3.70196580089717
O	2.77408931661492	2.79157957305745	0.04072400452719
O	-0.06929550651025	0.03324757180450	-2.81673809709067
O	-2.93077927159077	-2.66476800675403	0.08016227999806
O	-4.03258512712830	0.18869942816225	3.72920966294133
O	2.65284474334172	-2.78876966444245	0.09580519201514
O	3.85965529203922	0.01259708270326	3.75165799614737

8. APPENDIX B: TABLE OF REACTIONS

Target Compound	Reaction ID (AAK-###)	Scale and Reaction Conditions
$[B_{12}(CN)_{12}]^{2-}$	004–006, 008, 011–015, 017–025, 027, 033, 037, 038, 040, 042, 044–055, 057–059, 067, 068, 070–073, 077, 092, 096, 097, 099–101, 104	*Scale:* 0.02–0.5 g $[Et_4N]_2[B_{12}I_{12}]$ *Yield:* ≤ 39% *Heating:* MWI
$[CB_{11}H_6(CN)_6]^-$	007, 028, 030–032, 036, 039, 041, 043, 074–076, 082, 083, 102,	*Scale:* 20–80 mg $[Et_4N][CB_{11}H_6I_6]$ *Heating:* MWI
$[CHB_{11}(CN)_{11}]^-$	009, 010, 029	*Scale:* 20 mg $[Et_4N][CHB_{11}I_{11}]$ *Heating:* MWI
$[B_{10}(CN)_{10}]^{2-}$	063–066	*Scale:* 20 mg $[Et_4N]_2[B_{10}I_{10}]$ *Heating:* MWI
$[B_{12}(COOH)_{12}]^{2-}$	078, 079, 084, 085, 087, 088, 090, 091, 094	*Scale:* 15–60 mg $[Et_4N]_2[B_{12}(CN)_{12}]$ *Heating:* MWI and conventional